UNIVERSITÀ DI PARMA

UNIVERSITA' DEGLI STUDI DI PARMA

DOTTORATO DI RICERCA IN

SCIENZE E TECNOLOGIE DEI MATERIALI

CICLO XXXIV

DEVELOPMENT OF BIFACIAL OR FLEXIBLE THIN-FILM PHOTOVOLTAIC DEVICES BASED ON COMPLEX CHALCOGENIDES BY PHYSICAL VACUUM AND LIQUID PHASE DEPOSITIONS

Coordinatore:

Chiar.mo Prof. Dalcanale Enrico

Supervisori:

Dr. Delmonte Davide

Dr. Gilioli Edmondo

Dottorando: Sala Andrea

Anni Accademici 2018/2019 – 2020/2021

ABSTRACT

The climate change is indisputably the main problem of this century. Therefore, courageous policies of energy supply renovation towards green and renewable sources must be acted worldwide, as soon as possible. Particularly, concerning the photovoltaic technology, some serious challenges are exponentially arising, related to the availability and costs of raw materials and, at the same time, to the increased request of clean energy. For these reasons, an expanding number of scientific publications is nowadays devoted to find alternative, non-toxic and earth-abundant materials, applicable in the pre-existing technologies. In the field of thin-film solar cells (TFSC) technologies, the search of new solutions for each constituting layer is needed to significantly improve performances.

The objective of this work is to explore possible materials and deposition processes modifications for the chalcogenide-based TFSC. The typical TFSC architecture is composed by a supporting material such as glass or polymers; a metallic or transparent conductive oxide (TCO) substrate; the main absorber layer made of complex chalcogenides stacked under a CdS buffer layer to create the p-n junction; two contact layers made of undoped and Al doped ZnO. Three main possible alternatives were investigated:

[1] Engineering back contact substrates to improve performances and enlarging active areas for bifacial solar cells (BFSC) application;
[2] Study of the RF-sputtering deposition parameters for inducing an oriented growth of the alternative absorber layer Sb_2S_3, made of abundant and available elements;
[3] Development of low-cost, green and scalable deposition and processing methodologies for the realization of innovative solar devices based on $CuInS_2$ (CIS) varnishes/inks, obtained via high-energy ball milling.

[1] A BFSC, thanks to its two transparent contacts, can collect both direct and albedo light. They represent a smart solution to improve PV performances, limiting at the same time the amount of material employed to produce a single cell. BFSCs are generally less efficient than classical single-sided TFSC cells. This is due to the characteristics of the back contacts, usually TCOs, which are less performing than metals in the photocurrent extraction on mean and large area devices. For this reason, we worked on defining new engineered substrates which could possibly merge the optical properties of a TCO with the electrical properties of a metal. Specifically, Mo grid embedded in a TCO layer, were

developed through a tricky photolithographic process followed by a selective chemical etching. After that, the selected TCO was deposited through RF-sputtering. The overall process was developed either with positive or negative photolithography, starting from both commercial and auto-produced substrates. The mixed layer granted an improvement of the cell active areas thanks to cooperative action of TCO and metal: the former provided good bifacial behaviour, the latter an effective collection of the carriers. In particular, Mo:FTO mixed layers presented improved performances as compared with a not engineered bifacial device. Nevertheless, some intrinsic limitations, affecting the Mo:FTO processing, make this engineered layer not suitable for the final application. Contrarily, Mo:ITO substrates resulted to be more proficient due to their quasi-ideal diode behaviour. For Mo:ITO back contacts overall active areas are greatly improved, over 2 cm^2, while very low sheet and high shunt resistances are retained. Further studies, devoted to refining the processability of these embedded grids mixed contacts, are ongoing: the aim is to obtain the smoother surface to properly fabricate $CuIn_{0.5}Ga_{0.5}Se_2$-based BFSC deposited via Low Temperature Pulsed Electron Deposition (LT-PED).

[2] One main topics in the scientific research on TFSC is to find alternative solutions to abandon expensive and/or toxic elements like In, Ga, and Cd. One promising candidate is Sb_2Se_3. It is high absorbing p-type semiconductor which can in principle reach efficiencies of over 28%, according to the Shockley–Queisser theory. Thanks to its quasi-mono-dimensional ribbon-like covalent structure, the photogenerated carriers can almost freely flow along covalent bonded ribbons while they are hindered to flow perpendicularly, due to the presence of Van der Waals forces involving the neighbouring ribbon chains and leading to an unfavoured hopping-driven conduction mechanism. Therefore, in such a system, a key role is played by the crystallographic orientation of the AS layer: particularly, (hk0) directions, which identify ribbons completely lied on substrate, have to be avoided. Contrarily, (hk1), corresponding to slanted ribbons orientation, and (00l), characterized by ribbons normal to substrate, should be obtained in order to maximize the current extraction. Therefore, a theoretical study was done in order to evaluate which substrates can possibly influence a correct Sb_2Se_3 growth. Reasoning on epitaxial mismatches and lattice parameters, a wide selection of materials to be employed as back contact was put in comparison. Structural data were retrieved through Vesta software and ICSD simulations. The results were controversial: all tested metals, ZnO and FTO likely favour (hk0) reflections; moreover, ITO can produce random orientations. Despite this, an interesting fact was observed: RF-sputtering depositions, if prolonged in time, seem to allow Sb_2Se_3

self-orientation. Preliminary tests on this showed great improvements in the promotion of (hk1) and (00l) reflections. Lastly, a new engineered back contact was ideated, and novel studies are ongoing to verify its real effectiveness. Specifically, a distribution of ZnO nanowires will be prepared oriented normal to the substrate. Such layer could influence a growth of ribbons concordant with the ZnO nanowire axes, thus favouring (00l)-type reflections. First attempts seem to confirm the above statement.

[3] A very comprehensive work concerned the development of innovative CIS-based solar devices, obtained through ultralow-cost liquid phase deposition. Homogeneous and sub-micrometrical CIS powders were obtained by mechanochemical reaction performed through high-energy planetary ball milling experiment. After that, CIS varnishes were prepared by means of liquid assisted refinement, adding 2-propanol as solvent and mixing a tiny amount of NaF (0.2% in mass) as dopant. These varnishes were deposited by simple techniques, like manual brush painting or drop-casting. Through a standardised process, composed by four steps, the powder distribution was then transformed into a film and completed with CdS buffer layer . However, about 2% of S was systematically lost, probably during the annealing step. Morphological analyses, carried out by AFM and SEM, confirmed that after this articulated process the films were flatter than as deposited samples, with highly reproducible thicknesses of about 2 µm. Remarkably, resistivity of 200 Ω*cm, average mobility of 10 $cm^2/(V \cdot s)$ and intrinsic carriers' concentration of 10^{15} cm were achieved; surprisingly, these results were comparable with those obtained on CIS deposited by common vacuum techniques such as LT-PED. Two windows layers (ZnO and Al:ZnO) were then deposited via RF-sputtering, completing solar cell. 0.22% of efficiency, low short circuit currents (2.81 mA/cm^2), low open circuit voltages (211.68 mV) and fill factors (0.37) were achieved on Mo-based devices. Consequently, high series resistance were detected, depending on the CIS morphology: the presence of very fine CIS powders leads to tremendous surface area vs. Volume ratio. Low doping diffusion rates due to a mild use of temperature during the film processing, do not helped to passivate grain boundaries and achieve better characteristics. For these reasons, two independent but simultaneous paths were undertaken:

a. Stabilisation and diffusion of the NaF dopant prepared as a varnish;
b. Study of a new process for the absorber layer re-crystallization.

(a) A new NaF varnish was stabilised in 2-propanol by ball milling treatment and deposited through drop-casting in order to create a homogeneous distribution of separated crystalline units on the substrate. Different operations were discriminated depending on the chosen substrate (FTO or Mo). Afterwards, CIS was manually deposited, then treated as reported above; finally, the cell was completed by RF-sputtering. A slight diffusion of the alkaline dopant from the bottom of the solar absorber layer helped to improve the photovoltaic characteristics both on Mo and FTO. The extraction currents were tripled, as well as the efficiencies. Despite this, open circuit voltage as well as fill factors resulted far to be optimal, as reported in the table below.

	Mo	**FTO**
J_{sc} (mA/cm^2)	7.65	7.00
V_{oc} (mV)	250.72	268.11
FF	0.32	0.36
PCE (%)	0.60	0.70

Such very poor performances can be possibly ascribed to very low absorber crystallinity and dopant diffusion.

(b) Open-air annealing step of recrystallization has been modified introducing a close-system thermal treatment which can allow to work in selected atmosphere enhancing internal temperatures. Particularly, it was chosen to work in overpressure of sulphur being careful of calibrating the amount of sulphur as a function of the working temperature: indeed, too high sulphur partial pressure can poison CIS layer, too low pressures can lead to sulphur sublimation from the film and so CIS decomposition. The balance was found by working with 150 mg of sulphur at 600°C for 30 minutes. As a result, CIS crystallinity was greatly improved. Despite this, after some electrical tests, the semiconductor resulted totally compensated and an insulator-like behaviour with series resistances over 1 MΩ*cm was measured. A possible explanation can be given considering a detrimental action of 2-propanol: the solvent, which possibly remains trapped inside the film, during the annealing at high temperatures, can decompose, causing CIS layer carbon poisoning and so the loss of its PV properties. In order to solve these issues, a new water-based varnish is under investigation.

TABLE OF CONTENTS

TABLE OF ABBREVIATIONS

Abbreviation	**Definition**
1 G	First PV generation
2 G	Second PV generation
3 G	Third PV generation
4 G	Fourth PV generation
4SP	Four step process
ASe	Antimony selenide
AZO	Aluminium-doped zinc oxide
BF	Bifacial
BFSC	Bifacial solar cell
BIPV	Building integrated photovoltaic
BPR	Ball to powder ratio
BZO	Boron-doped zinc oxide
CBD	Chemical bath deposition
CIGS	$Cu(In_xGa_{1-x})S_2$
CIGSe	$Cu(In_xGa_{1-x})Se_2$
CIS	$CuInS_2$
CISe	$CuInSe_2$
CS	Cold sintering
DC-MS	Direct current magnetron sputtering
EBL	Electron-beam lithography
EDX	Energy dispersive X-Ray spectroscopy
EUV	Extreme ultraviolet lithography
F4SP	Four step process optimised for FTO
FF	Fill factor
FOURIER	FotovOltaico efficiente in facciata per il fUturo pRossimo della rEte elettRica
FTO	Fluorine-doped tin oxide
FWHM	Full width at half maximum
GB	Grain boundaries
HIP	Hot isostatic pressure
HiPIMS	High-power impulse magnetron sputtering
HS	Hot sintering
HTS	High-temperature semiconductors
I_L	Light-generated current
I_o	Current in dark conditions
i-PrOH	2-propanol
I_{sc}	Short circuit current
ITO	Indium tin oxide
JCPDS	Joint committee on powder diffraction standard
J_{sc}	Short circuit density
LAG	Liquid assisted grinding

LT-PED	Low temperature – pulsed electron deposition
M4SP	Four step process optimised for Mo
$MAPbI_3$	Methyl-ammonium lead iodide
MC	Mechanochemical
PCE	Power conversion efficiency
PET	Polyethylene terephthalate
PIPV	Product integrated photovoltaic
PLD	Pulsed laser deposition
P_{MP}	Maximum real power
PTFE	Polytetrafluoroethylene
PV	Photovoltaic
PVD	Physical vapour deposition
PVOUT	Photovoltaic power potential
PXRD	Powder X-ray diffraction
$\rho_\square$	Sheet resistivity
RF-MS	Radio-frequency magnetron sputtering
RMS	Reactive magnetron sputtering

RPM	Rotation per minute
R_s	Series resistance
R_{sh}	Shunt resistance
RT	Room temperature
SEM	Scanning electron microscopy
SLG	Soda-lime glass
SPL	Scanning probe lithography
SQ	Shockley-Queisser Theory
TC	Texture coefficient
TCO	Transparent conductive oxide
TFSC	Thin-film solar cell
UV	Ultraviolet
UZO	Undoped zinc oxide
VdW	Van der Waal interaction
V_{oc}	Voltage in open circuit configuration
VTD	Vapour transport deposition
YBCO	$Yba_2Cu_3O_{7-x}$

CHAPTER 1

INTRODUCTION

1.1) A WORLD HUNGRY OF ENERGY: THE CLIMATE CHANGE ISSUE

During the last decades, the impact of mankind's life and activities on nature was devastating. At the origin of this process, there is the increasing need of energy made even more poisoning by the lack of punchy and effective environment policies addressed to a deep transformation of the concept of human activities. In the last 50 years, the deforestation of rainforests, the intensive farming livestock, the use of nitrogen fertilizers and the burn of oil, coal, and natural gases, produced enormous amounts of greenhouse gases dispersed in the atmosphere (Figure 1.1). Particularly, the massive production of carbon dioxide, methane, nitrous oxide, fluorinated gases is the principal responsible of global warming and the greenhouse effect. Consequences are evident: an abrupt, never recorded, and thus dramatic increase in the world's average temperatures.

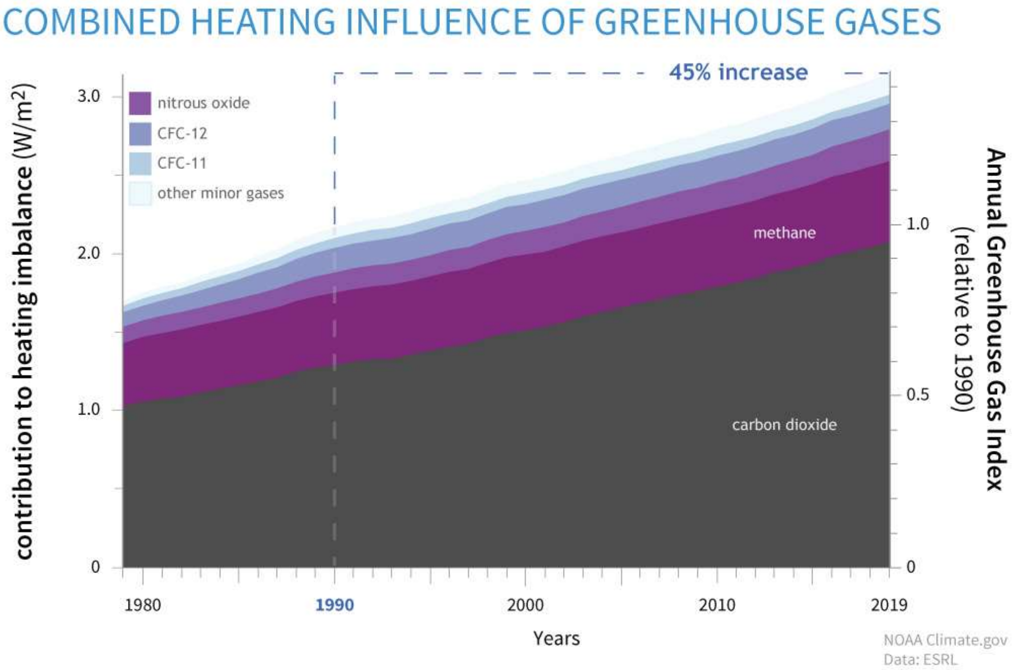

Figure 1.1: The combined heating influence of greenhouse gases during the last four decades.[1]

If the last 800,000 years are considered, nothing similar had happened before. In *Figure 1.2*, it is possible to evaluate the CO_2 trend during this long period. From the industrial revolution, the carbon dioxide concentration in the atmosphere grew from 280 ppm to over 400 ppm, leading to the periodical oscillations of this parameter along unpredictable ascendant path. It is so clear that, the role of men's activities in this process is undeniable.[2]

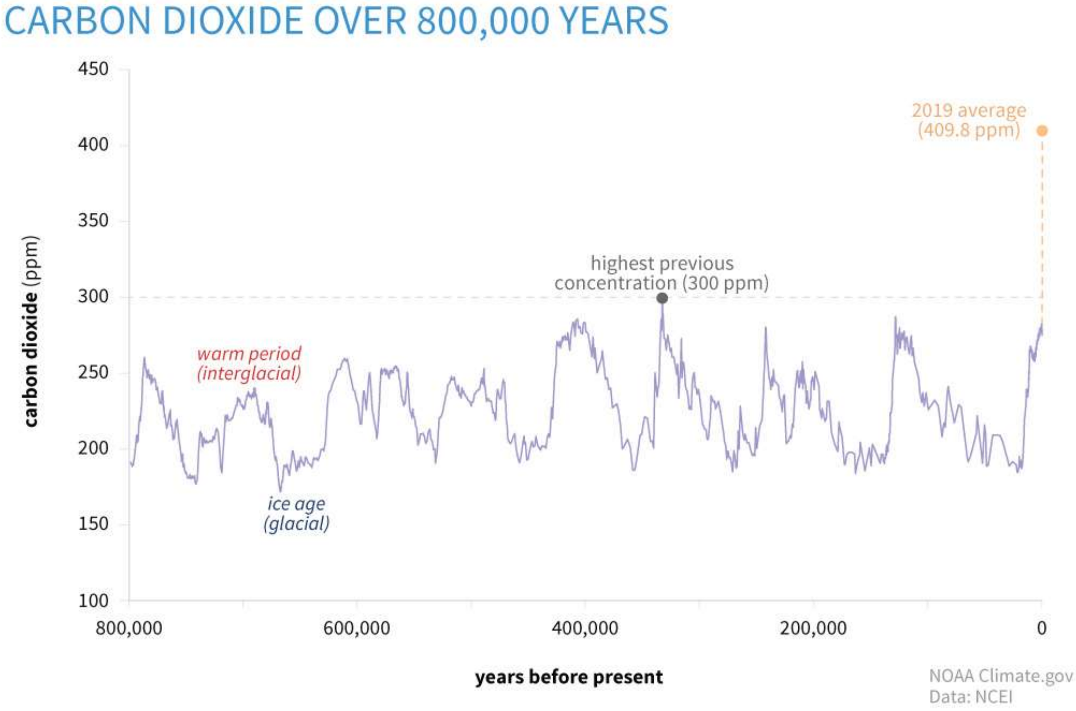

Figure 1.2: Carbon dioxide concentration in the atmosphere during the last 800,000 years.[2] *Notice the effects of the industrial revolution in the previous two centuries with the consistent increase of CO_2 emissions.*

The phenomenon of climate change is well known and recognized by the scientific community. In 2020, global warming marked +1 °C on the average planet temperature since the beginning of the industrial age. The situation is foreseen to worsen with an increase of +3 or more degrees. Year after year, the weather is getting more extreme, the ice caps are melting faster than ever, the oceans are warming up, getting more acidic, and sea levels are rising. Those effects will cause direct consequences with incalculable damages to nature, ecosystems, wildlife, but also to human health, economy, and society. This process could not be stopped, but hopefully decelerated. The only possibility to avoid the scenario explained above is a massive reduction of greenhouse gases, the quicker, the better.[3] The actual Agreement of Paris, promulgated by 55 countries worldwide, is focused on limiting 40% the CO_2 emission by 2030, on containing the temperature rise within 1,5 °C.[4]

Climate change is a direct consequence of crazy energy requirements to sustain our social model and our wellbeing standards. Burning oil, coal, or natural gases to produce an enormous amount of energy has become detrimental. Moreover, these energy sources are not renewable. Many alternatives could help humankind at this stage. Renewable energies and green policies could limit the effects of climate change. In 2019, around 11% of all the primary energy came from renewable technologies.[5] It is possible to obtain the total power from wind, water, waves, earth, biofuels and, mainly, from the sun?

1.2) THE PHOTOVOLTAIC SOLUTION

Every year our planet is invested by a massive amount of solar energy, estimated in 179 PW (i.e., $179 \cdot 10^{15}$ W). A large part of this sunlight is reflected or absorbed by the atmosphere, but a big fraction of this enormous power is in principle available for photovoltaics (PV) technology. It is possible to estimate this quantity as 86,000 TW per year; in 2018, the whole world consumed an amount of energy equal to 45 TW per year.[6] It is therefore easy to understand that photovoltaics, among all renewable energy sources, is by far the most promising and could by itself provide all the energy we need.

Many studies based on the solar irradiation shown in Figure 1.3 confirm the possibility to power the entire world with only solar energy. Desertic and equatorial areas of the planet are more exposed to solar irradiation and located at the perfect latitude to maximize the yield of photo-conversion. Matching direct and horizontal irradiation data is possible to estimate the photovoltaic power potential (PVOUT).[7]

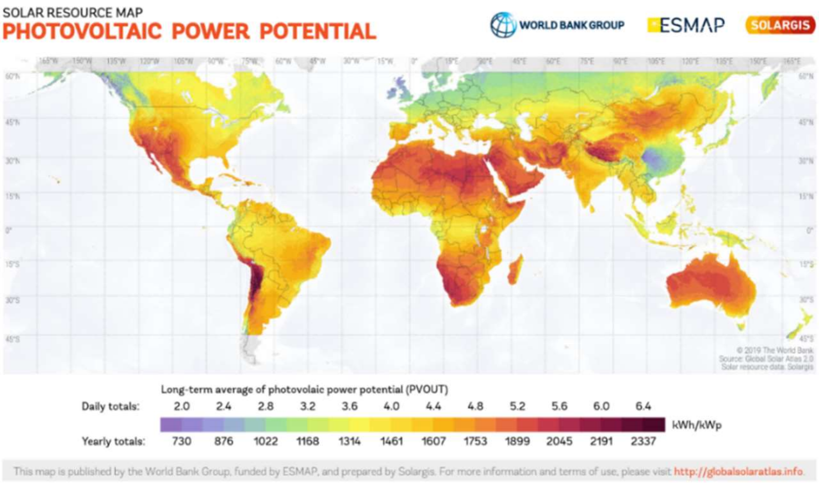

Figure 1.3: The world photovoltaic power potential obtained matching horizontal and direct irradiation of each area of the planet.[7]

It was calculated that few and large solar plants placed in the points of greatest solar irradiation could cover all the power requirements of the planet without emitting carbon derivates. The calculated data, shown in *Figure 1.4*, reports a realistic projection of square kilometres of photovoltaic surfaces required to cover all the energy requirements in 2030.[8] It is necessary to underscore that a total of 500,000 square kilometres of implants could be reduced by the use of more efficient technologies than the classic photovoltaic panels based on Si. For example, a High Concentration or Multi-Junction PV Systems could significantly reduce the total active solar areas. Obviously, this reduction should not be inversely proportional to the production cost.[9]

Figure 1.4: A projection of the critical area that would be needed in the year 2030 to power the world via photovoltaic energy. The Saharan Desert square (1/4 of the total) could supply the power of the whole of Europe and North Africa.[8]

The practical realization of this perspective is quite far. As reported in *Figure 1.5*, many countries like the United States, China, India, and South Africa are constantly increasing their annual solar energy production. Nevertheless, the cumulative solar power generated is far to even approach the value of 45 TW. In 2019, the world total installed solar energy capacity was only 587 GW, around 1% of what required.[5]

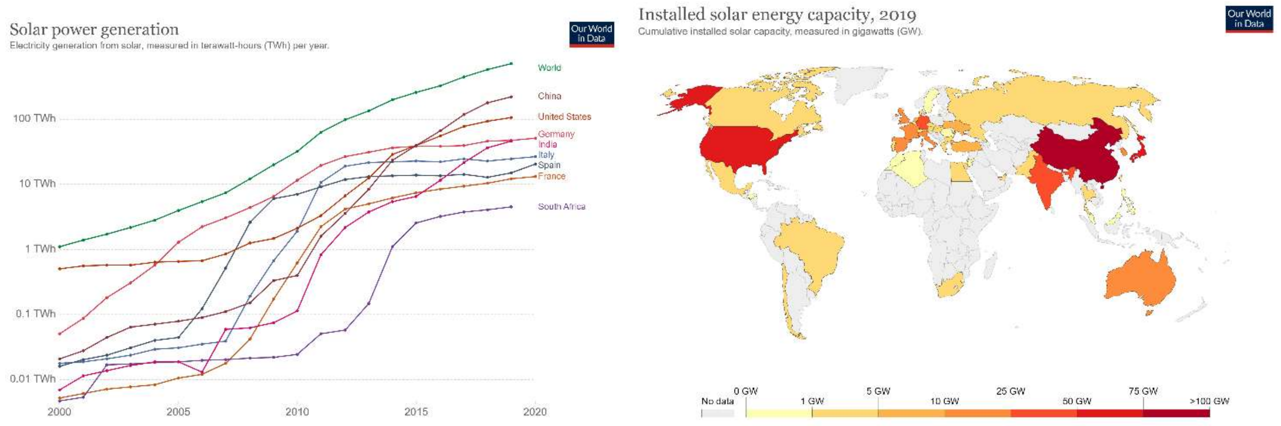

Figure 1.5.[5] Left: Logarithmic solar power generation trend of major green energy producer countries in the last 20 years. Right: Installed solar energy capacity in 2019, divided by countries.

1.3) PHOTOVOLTAIC TECHNOLOGIES

The studies on the photovoltaic effect started with Becquerel[10] in 1839, culminated in 1921 with of the Nobel prize for the discovery and description photoelectric effect, awarded to A. Einstein. In 1954, the United States became the leader in photovoltaic technologies creating the first p-n junction silicon-based device.[11] In the following years' Japan, Germany and now, China took the lead of the PV industry. Nowadays Si-based PV technologies are fully consolidated, and we are experiencing a continuous development and expansion towards novel and more performing devices, focused on finding ever more innovative, non-toxic, cheap, and efficient photovoltaic devices.

The principle of the PV effect is the following: when two different semiconductors (one n-doped, with extra free electrons, and another p-doped, with extra free holes) are in contact, the carriers of one sign flow through the interface to compensate the carriers of opposite sign, creating a depletion layer with no free charges, a p-n junction. Upon illumination by sunlight, the photoexcitation is promoted at the depletion layer of the junction, generating a couple electron-hole which is drifted by the electric potential acting across the junction, causing the free movement of charges from one side to the opposite of the system. If a circuit is closed, the electrons can flow outside the device (extraction process). One of the most important parameters in PV technologies is the power conversion efficiency (PCE% or η%). According to the Shockley–Queisser (SQ) limit[12], a single p-n junction, working in ideal condition, cannot convert more than 33,7% of the incident solar light energy. Specifically, the maximum conversion efficiency is strongly related to the bandgap energy and to the electrical properties of the considered semiconductors, but also to the type of illumination. The SQ theory considers several factors, like carriers' recombination, black body radiation, spectrum losses and many others. This theoretical limit can be surpassed with some expedients (e.g., light concentrators, tandem or multi-junction devices), as reported below.

Based on the type of materials and architecture used, four PV generations are generally recognized. *Figure 1.6* reports an overview of the trends of maximum cell efficiencies from 1975 to 2020; each colour group represents a different generation of photovoltaic devices.

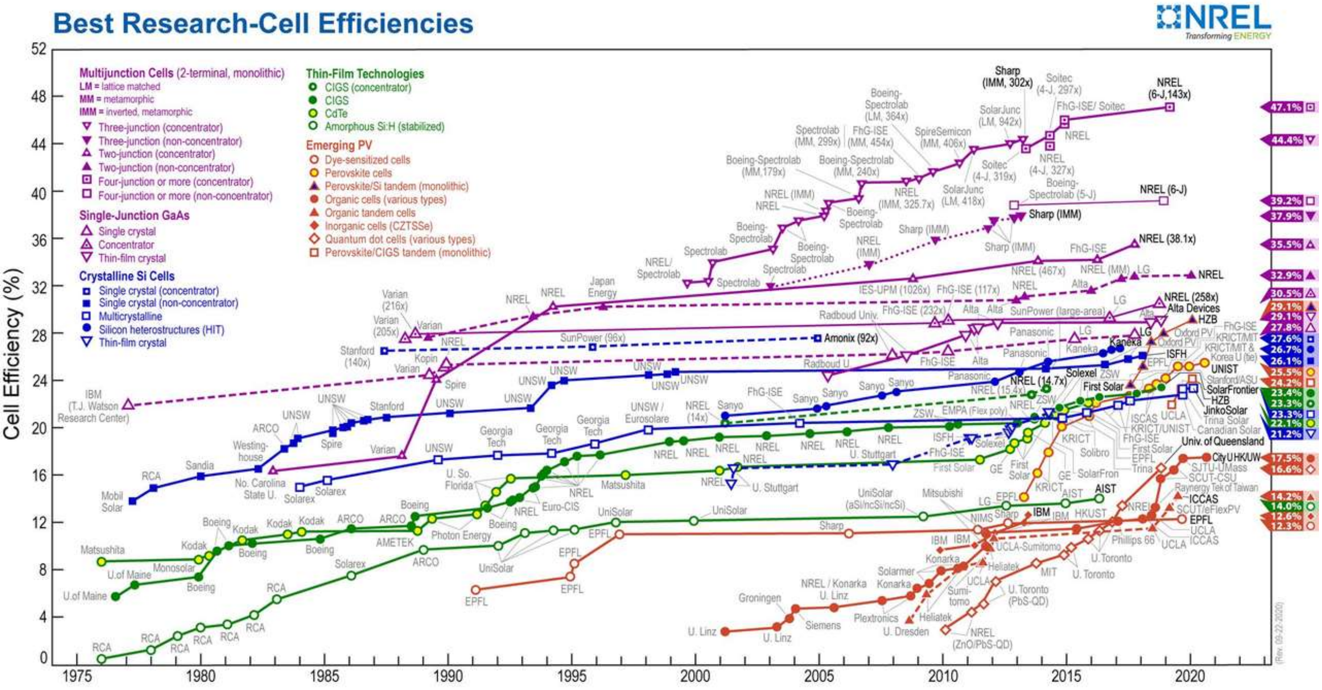

Figure 1.6: The best cell efficiencies at the lab-scale chart over the last 45 years (by NREL).[13] *Colour groups reported the four different PV generations: Crystalline Si Cells, thin-film Technologies, Multijunction Cells and Emerging PV (respectively).*

The first generation (1 G) is based on crystalline silicon, high earth-abundant elements and represents the main part of PV devices present in the global market. The module is generally composed by two differently doped layers of Si in contact to form a single p-n junction. The most common silicon modules are made by monocrystalline or polycrystalline Si wafers, the former with higher efficiencies and cost. In the earlier 2000s, the cost of raw Si for PV modules was around 30 $/kg. A rapid expansion of semiconductors requests caused a dramatic shortage of raw materials with the effect of a significant increase in terms of cost (475 $/kg in 2008).[14] This pushed the research to find solutions and several techniques, second and third generations (2 G and 3 G, respectively), were developed to avoid the use of significant quantities of silicon (e.g., thin-films or multijunction devices). Nowadays, thanks to an improved mass production combined to the reduction of Si wafer thicknesses, the price of raw silicon is cheaper than ever (around 7 $/kg): so, today the cost of a single module of crystalline silicon is lower than 0.10 $ (in 2020). Besides, the 2 G and 3 G were improved, to use fewer quantities of expensive semiconductor materials. Focusing on the thin-film solar cells (2 G), the use of different materials allowed also improving the development of flexible and light PV modules. Despite lower top efficiencies than 1 G, materials like $Cu(In_xGa_{1-x})Se_2$ (CIGSe), CdTe and amorphous Si are strong competitors for several application aspects. The main advantage and characteristics of the 2 G is the possibility to design thin-film solar cells (TFSC) starting from these alternative semiconductors with high absorption coefficient. The fabrication of thin-film solar devices is the main subject of this PhD thesis and will be extensively discussed.

Moreover, innovative solar devices presenting up to six p-n junctions are representative of the PV third generation (3 G). The presence of several junction in whole device, specifically designed to be activated from photons of a certain energy, allow to easily overcome the SQ limit.[12] Their actual business is limited to aerospace and power plants applications due to their high energy production with very tiny material utilization but also their extremely high production costs. These devices exploit the penetration of the various wavelengths that compose the light spectrum, and each junction is specifically designed to absorb photons of specific energy. Devices characterized by six p-n junctions, can reach 39,2% of efficiency. 3 G PV devices are usually made of undoped and substituted GaAs (e.g., InGaAs or InGaP). The efficiency could be magnified via a concentrator. Under 143 suns concentrator, a NREL 6J device can reach 47,1% of total efficiency.[15]

The fourth generation of PV (4 G) Is a broad and heterogeneous group, constituted by technologies based on organic polymers to inorganic perovskites, with complex structures and/or methods (from quantum dots to dye-sensitized devices). They also exhibit a variety of different properties; for example, an organic polymeric solar device is cheap, thin, semi-transparent, flexible, and it is composed of abundant and low-cost elements (like plastics or fullerenes), but in general, the carrier diffusion is slow, and the PV efficiency is low. For this reason, new bulk-heterojunctions were developed on purpose.[16, 17] In 2018, the

Organic PV maximum efficiency reached 17,3%.[18] Furthermore, one of the most interesting subgroups of 4 G is represented by hybrid organic-inorganic perovskites (ABX_3 structure). Materials like methyl-ammonium lead iodide ($MAPbI_3$) and other halides have been intensely studied for PV or water splitting applications.[19]

1.4) THIN-FILM SOLAR DEVICES: AN OVERVIEW

The real revolution made by thin-film (2 G) PV can be resumed in the extensive applicability of modules and the possibility of drastically reducing the quantities of material employed. A thin-film module is very light; it could be rolled thanks to the flexibility,[20] it can be semi-transparent or bifacial (BF),[21, 22] and it can be integrated in buildings or in products (e.g., utility scale tandem cells, Building Integrated PV, Product Integrated PV).[23, 24]

A thin-film solar device is generally composed by several layers of different thicknesses which usually do not overcome the total amount of 10 µm.[25] The thicknesses could be significantly reduced to allow the partial transmission of the sunlight in case of semi-transparent application of devices.

In the cell architecture, reported in *Figure 1.8*, the lower part of the module is the substrate. It supports the cell and could be composed by standard soda-lime glass (SLG), steel, fabrics, or plastics (e.g., polyimide, PET, or parylene etc.). The back contact is, generally, the layer used to collect holes. It is constituted by metals like molybdenum, aluminium, silver, gold, or transparent conductive oxides (TCOs), such as indium tin oxide (ITO), undoped tin oxide (UZO) or fluorine tin oxide (FTO). These oxides are commonly used in the case of BF modules. Finally, it is possible to find, directly stacked on back contact, the light absorber material. 2 G main absorbers are, generally, semiconductors with direct bandgap and very high absorption coefficient ($>10^5$ cm^{-1}). The photons are, thus, easily absorbed, and therefore, the thicknesses of 2 G absorbers are lower than the corresponding 1 G materials with indirect bandgaps. Another strictly necessary parameter is the absorbed photon energy. The light wavelength can be plotted with the material's absorption coefficient to estimate which region of the visible spectrum shows the maximum value, as shown in *Figure 1.7*.

CIGSe ($CuIn_{0.5}Ga_{0.5}Se_2$) and CdTe are the two founder materials of thin-film technologies, although they have some drawbacks. The former contains rare and expensive elements such as indium, and the latter is very toxic due to high cadmium content. Therefore, research is nowadays focused on developing new cheap and non-toxic absorbers with optimal characteristics and high PV efficiency.

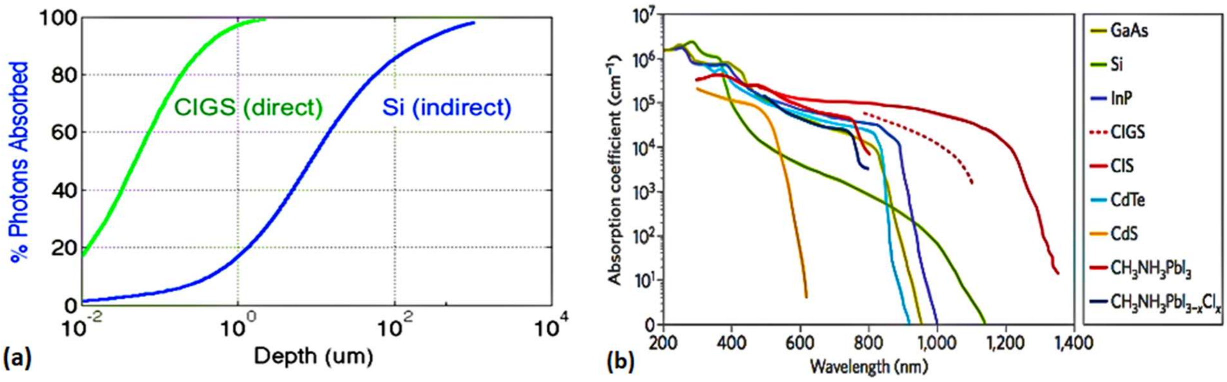

Figure 1.7: (a) The plot of photons absorbed percentage in the case of CIGS (direct bandgap) and Si (indirect bandgap). (b) The plot of photon wavelength and absorption coefficient of materials commonly used in thin-film technologies as absorbers.

A n-doped semiconductor material in contact with the absorber layer forms the p-n junction, the heart of the whole solar device. The materials composing this layer must have a higher bandgap than the absorber to allow the carriers extraction, a good electrical conductivity and optical transparency in the visible spectrum, to avoid photon absorption. Common buffer materials are CdS, ZnO, ZnS or $BiVO_4$. The solar cell is completed by stacking over the p-n junction one or more n-doped layers, called top contact and window layers. TCOs like the bi-layer ZnO/Al:ZnO (UZO/AZO) or ITO are usually chosen for this scope. Finally, on the top of the device, there are metal contacts. The ohmic contact is mandatory, and several geometries have been studied over the years to minimise power losses given by metals spurious contact resistivities. Depending on the needs and applications, another type of stacking of the layers, called “superstrate” cell, is possible. This scheme is somehow the reciprocal with respect to the substrate architecture: it foresees a front contact directly deposited on the substrate, followed by a buffer layer, absorber, and back contact, as represented in *Figure 1.8*.

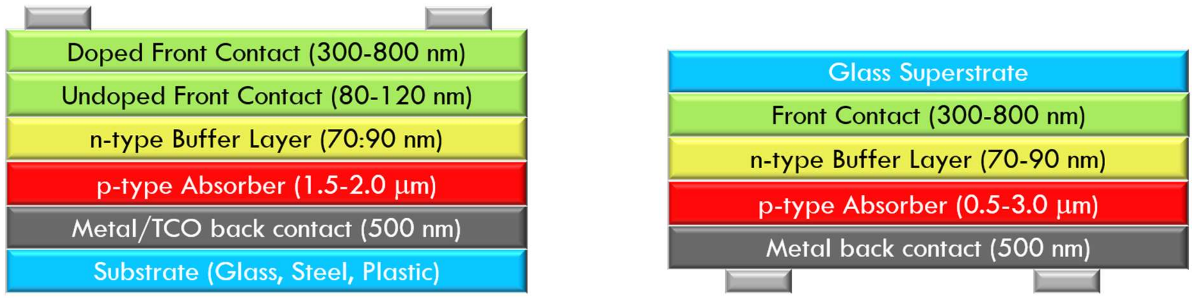

Substrate Architecture

Superstrate Architecture

Figure 1.8: Schematic representation of the commonest thicknesses and architectures (substrate and superstrate) in thin-film solar devices.

A wide selection of suitable materials, together with the exploitation of different possible architectures, contribute to generate an uncountable number of studies on TFSC: starting from innovative layers towards new materials, moving from new preparation techniques to proper development and study of devices structures and performances. Specific cases which are subject of this Thesis are reported in the following.

(1) Bifacial solar cell (BFSC), able to collect sunlight from both sides. Compared to a classic substrate cell grown on opaque metal, the use of a TCO as back contact can increase the overall efficiency by up to 20-30%.[26] Despite this, the electric conductivity, and the sheet resistivity ($\rho_{\square}$) of a TCO are inferior compared to metal's performance.[27] For these reasons, new engineered layers could be studied using metallic grids embedded in TCOs. The embedded grid layers enable the appropriate sunlight exposition from the device's back-side, thanks to transparent oxide windows. At the same time, the collection of holes is maximised by the metal grid, making this solution very promising for BIPV technologies.

(2) The properties of each selected absorbing material have a heavy impact on the device performance. The carrier's diffusion along and across the grain boundaries (GB) composing a layer is fundamental in PV technologies.[28] As reported above, well established structurally isotropic materials like CIGSe or CdTe have been intensely studied over decades. However, the necessity to find non-toxic, cheap, and earth-abundant elements drives the researchers to perform several studies on innovative materials which are flourishing (e.g., antimony sulphides or selenides).[29] These materials possess an anisotropic covalent ribbon-like quasi-1D structure. The covalent ribbon elongates in a unique direction interacting each other by Van der Waal (VdW) interactions. The carrier's movement is, thus, favoured along with ribbons and compromised across them. A

maximised carrier extraction could be achieved if an absorber layer is grown on a precise crystallographic orientation on a proper substrate. This and other characteristics explained in this work make materials like ASe a cornerstone of the forthcoming 2 G PV research.

(3) Innovative, low-cost solar cells preparation technique. In the last years, we developed a completely new method to “paint” a solar cell, by using a photovoltaic “varnish”. The varnish can be prepared in both chemical and physical ways; one of the most innovative techniques is by the mechanosynthesis. In sort, absorber materials (e.g., $CuInS_2$, CIS)[30] can be prepared via a mechanochemical synthesis through a ball milling machine.[31] Then, it is possible to obtain an ink or a varnish, simply adding a small quantity of a proper solvent during the refinement process, applying the so-called Liquid Assisted Grinding (LAG). Once a stable suspension is obtained, it is possible to deposit absorber layers through a brush, by drop-casting, spin-coating or via ink-jet printer. This methods are innovative, extremely cheap, and easily scalable.

Chapter 6 will be devoted to study of such innovative prototypal devices produced starting by painted and *printed* absorbers, reported in chapter 7. This study’s final goal, and so the applicative purpose is the production of building integrated photovoltaic cells with a partner company.

CHAPTER 2

AIM OF THE STUDY, MATERIALS AND METHODS

2.1) AIM OF MY PhD ACTIVITY

The motivation of this study is the development of innovative layers and novel production methods/techniques for thin-film solar devices. The work was divided into three major sections, depending on the type of layer.

(1) In the first section metal grids embedded in the TCO back contacts were studied in order to improve the performances of BF solar devices. This work was handled combining photolithography and RF-magnetron sputtering (RF-MS) techniques.

(2) The second section is focused on the complete characterization and growth parameters of antimony selenide (Sb_2Se_3, ASe) a promising solar absorber with a strong anisotropic character. The study was carried out through the RF-MS technique at different growth conditions. Theoretical evaluation and choice of the proper substrate was done through texture calculations in order to improve and control the crystallites orientation.

(3) The last major section is concentrated on the study of innovative mechanochemical synthesis, ink/varnish stabilization and ink deposition techniques of a well-known chalcogenide solar absorber, CIS. The aim of the final study is the manufacturing and full characterization of the whole stand-alone solar cell for BIPV and PIPV.

In the following paragraphs, all the preparation and characterization techniques used in this work are presented and brief presentation of each material studied is reported in the last section of this chapter.

2.2) THIN-FILM PREPARATION TECHNIQUES

2.2.1) LOW-TEMPERATURE PULSED ELECTRON DEPOSITION

Low-temperature Pulsed Electron Deposition (LT-PED) is an innovative physical vapour deposition (PVD) technique. It works through a pulsed electron beam, accelerated by an electronic gun which allows to reach high energy power densities (10^8 W/cm^2), directed on a proper target. The primary characteristics of LT-PED is the possibility to prepare thin-films having the same stoichiometry as the bulk target, independently from the phase diagram of the starting material. Power densities are higher even of the value to evaporate solid materials.[32] For this reason, the target is directly ablated in a few hundreds of ns: i.e., a plasma-plume of the constituting elements is produced, with shape and collimation which depend on the energy of electronic beam. Such a plume is generally characterized by the same compositional ratio between the elements. Although the ablation process follows non-equilibrium thermodynamics, it is impossible to avoid the target's thermal evaporation due to the heating processes following the discharges. This process can be minimized only with a correct modulation of the electron beam power density and pulses frequency. LT-PED is a powerful technique, suitable to prepare thin-films of a variety of materials characterized by good quality, purity, and uniformity even with incongruent melting points or very complex phase diagrams.

Through this technique, it is possible to deposit semiconductors, oxides (e.g., conductors or superconductors), sulphides, hydroxyapatites, alloys, even polymeric (e.g., PTFE) or biomedical materials.[33, 34] Since the plasma temperatures are very high and the ablated ions are very energetic, it is possible to grow high crystalline thin-films even at low temperatures. Indeed, materials such as high-temperature semiconductors (HTS) or superconductors like $Yba_2Cu_3O_{7-x}$ (YBCO) are deposited via a similar technique: the Pulsed Laser Deposition (PLD).[35] Despite the same working principle and similar products, cost balance between PLD and LT-PED is quite different. For example, a high energy laser source is more expansive compared to a simply hollow cathode source commonly used for LT-PED, making LT-PED preferable to PLD.

The LT-PED apparatus (Neocera PEBS-20) used in this work operates with the source inclined 45° to the target. The characteristic working pressure of LT-PED source was ~10^{-3} mbar, an inert gas (i.e., argon) was fluxed to create a plasma. This was accelerated from 12 to 18 kV and directed on the target through a dielectric alumina tube. The frequency of pulsated discharges was settled to 10 Hz, as standard. The target was a slice (few mms thick) of the bulk material to be deposited. This was positioned directly under the dielectric tube to fully intercept the incoming pulsed plasma. All targets used in this work were either purchased by supply companies, prepared via sintering process by the powders or realized by melt growth techniques.

Moreover, through a mobile carousel it was possible to change the type of material with a simple external rotation. During the LT-PED deposition experiment, substrates were placed upside down, facing the targets. The ablated material formed an expanding plasma plume that altogether included the substrate. The thickness of growing material was constantly monitored by a pyrometric camera. The temperature registered on the thin-film plotted vs. deposition time generated a sinusoidal trend. The first minimum corresponded to the thickness required for the standard absorber material. A schematic representation of the LT-PED instrument and the control graph is reported in *Figure 2.1*.

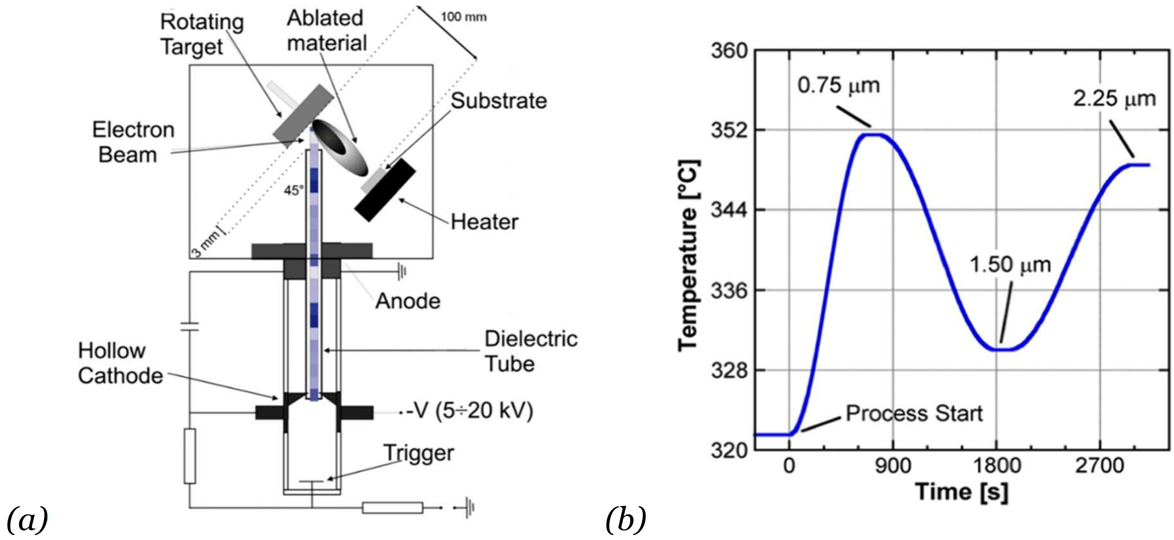

Figure 2.1: (a) Schematic representation of Low-Temperature Pulsed Electron Deposition instrument used in this work. (b) The sinusoidal plot of temperature vs. time is calibrated to finely control the growth rate.

2.2.2) MAGNETRON SPUTTERING

Sputtering is a widespread vacuum PVD technique, widely used both in industrial and in research fields. A magnetron sputtering instrument is generally composed by a vacuum chamber, a magnetron, a target, two electrodes, a generator of current, a vacuum pump and a system to push a gas inside the chamber. Both inert or reactive gases (e.g., argon and oxygen, respectively) could be used. In case of employment of reactive gases, the technique takes the name of Reactive Magnetron Sputtering (RMS).[36, 37] Through the modulation of current intensity, a plasma could be generated (i.e., argon), and the magnetron is very useful to focus plasma on target. The cloud shape is thus coherent to the magnetic field lines; as a consequence, the target's excavation is often not homogenous due to the use of a toroidal magnetic field. The plasma is principally composed by gas cations (Ar^+, as for the system exploited in this work) and electrons. Ar^+ cations are attracted towards the negative electrode till they violently hit the target. If the energies of this bombardment are superior to the bond's energies of the target's atoms, the bulk material passes directly in the gaseous phase. This process, indeed, is not very simple. The collision cascade is directly responsible for the sputtering process but involves several other secondary processes such as ion implantations, defect creations or neutral Ar emissions. If the incident ion mass is lower than the target atoms mass, the ion could be reflected, generating a scattering process. Otherwise, it can enter the bulk material generating an internal collision cascade. The evaporated material has no charge, thus is not influenced by electrodes, and the deposition takes place locating the substrate in the proper position with respect to the generated plasma cloud.

A sputtering instrument can work in two different generator arrangements: Direct Current (DC) or Radiofrequency (RF). A Direct Current Magnetron Sputtering (DC-MS) cheaply deposits conductive materials at high rates. However, it is challenging to obtain ultra-clean products due to the work's high pressures and voltages. It is, instead, possible to use an RF generator (RF-MS), more efficient than DC-MS: it works at lower pressures and, thus, it is possible to obtain purer samples with an enhanced control on time deposition parameters. However, a correct RF modulation is mandatory: low frequencies (kHz) influence both electrons and ions composing plasma, while high frequencies (>10 MHz) can influence only ions that are forced to hit the target. With RF-MS, it is possible to prepare films of conductive materials (such as metals or TCOs), alloys and dielectrics. In the last decade, a new MS technique has been developed: the High-Power Impulse Magnetron Sputtering, or HiPIMS.[38, 39] Despite being more expensive, this technique is very effective and merges the best characteristics of pulsed and direct current sputtering PVD techniques. It allows the production of ultra-pure thin-films of a large plethora of materials through the use of a dense pulsed plasma generated inside a particular hollow cylindrical target. It is particularly indicated to deposit nitrides, oxides, or metals (depending on the variant used, whether Reactive HiPIMS or normal).[40]

In this work two RF-Magnetron Sputtering facilities were used to deposit TCOs (e.g., UZO, AZO or ITO) and to deposit solar absorber materials (such as ASe). Both instruments were equipped with a 3′′ RF magnetron sputtering cathode (Kenosistec). Thanks to a collaboration with the University of Parma, department of Physics, Mo thin-films were occasionally deposited via DC-MS.

2.2.3) CHEMICAL BATH DEPOSITION

Chemical Bath Deposition (CBD) is an apparently straightforward technique that could be very complex if studied in depth. However, it is a very cheap and efficient method to prepare excellent thin-films. It does not need expensive equipment, is scalable, and can prepare large-area devices[41] or work in continuous flow. Furthermore, it is reproducible, yielding high stable, uniform, and hard thin-films with excellent adhesion to the chosen substrate, immersed in the precursor solution. Despite this, disadvantages could be found in the solution wastage and the mandatory requirement of perfect clean-up of substrates (without this passage, the adhesion of deposited film could be compromised). In this work, CBD was mainly employed to produce thin layers of cadmium sulphide (CdS). This material is one of the most common buffer layers used in PV technologies, as reported in paragraph 2.5.4. Therefore, the analyses and considerations discussed below have been considered to set the most efficient deposition process.

Three main issues must be optimized: the precursor solution, the substrate choices and related effects, and the process control.[42]

Generally, CBD is used to deposit materials with general formula is $MX_{n/2}$ via an aqueous media. M represents a generic metal and X an anion, in which the most common are chalcogenides (X = O, S, Se). To form the required material, it is necessary to choose a precursor metallic salt that has good solubility in water (e.g., chlorides, nitrides, acetates, sulphates) and a source of the chosen anion. In this study, the precursors couple are cadmium sulphate ($CdSO_4$) and thiourea, $CS(NH_2)_2$. Many equilibrium or reactive processes are involved in this system and the product precipitation could be very easy. The adjustment of pH and temperature parameters and, mainly, the addition of complexing agents allow to control formation and precipitation of the product compound.

Furthermore, to avoid fast precipitation and ensure good crystallites growth, it is necessary to carefully control the concentration of all reactive species. The system should remain as long as possible in the metastable range of oversaturation to allow nucleation over the sample immersed in the reactive solution.

The substrate effects depend on the interactions established between particles and surfaces where the film has to be grown. If surfaces are not compatible with the established interactions, several paths are preferable: a functionalization, a chemical etching (possible to improve roughness), a photolithographic treatment (to grant a selective growth).

The CBD set up is represented in *Figure 2.2*. At the beginning of the reaction, a short period of "incubation" corresponds to the first nucleation process (this parameter is influenced by pH value). After this, the film slowly starts to grow, and the thickness increases with a certain proportionality with time. At last, when solid particles begin to aggregate due to VdW interactions, the product starts to precipitate freely. Then, the last parameter is the dwell time. The substrate should remain immersed into the reactive solution during the intermediate reaction period, when time and thickness are directly proportional. Despite the great variety of floating parameters during a deposition, if no reagents or solvents are added, the temperature remains constant, and the solution is not stirred, the deposition could be easily controlled. For these reasons, when larger thicknesses are needed (>90 nm), it is preferable to repeat the process instead of extending the duration of the standard one.

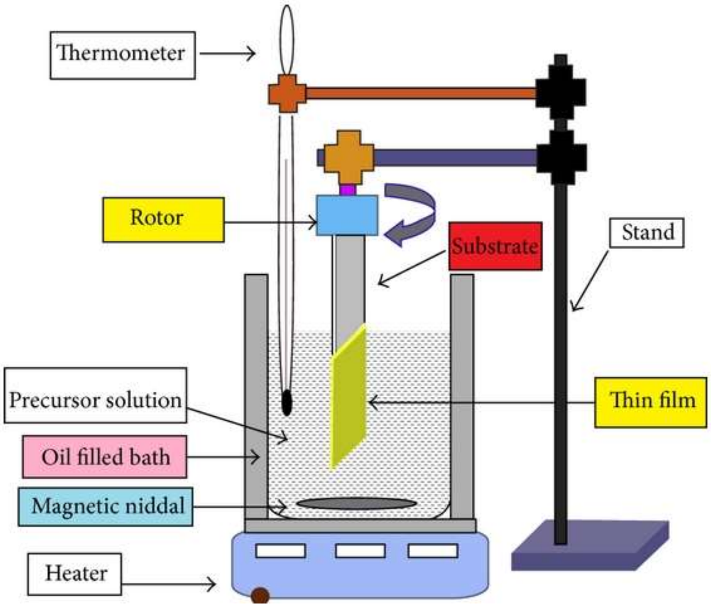

Figure 2.2: Schematic representation of CBD apparatus.[43] *Notice the possibility to apply a rotation to precursor solution even to sample. However, it is not always required; it depends on the type of deposition.*

One of the main problems of this technique is the great quantity of material wasted for every single chemical bath. It is also essential to preserve the fluid-dynamics of the aqueous media, being aware to utilise backers and glasses with the same volume and, using each solution only one time. A clean way to operate should be find in analogy with some industrial processes (e.g., Liquid Flow Deposition[44]) in which substrates are fixed on a proper holder and exposed to a flux of precursor solution, continuously filtered to remove aggregated clusters, and simultaneously re-adjusted to retain concentration.

After the deposition, each sample must be extracted, washed, and dried. This passage is critical because traces of reagents or water could be included in the wet film and thus modify its properties, as for instance its stiffness.

2.2.4) HIGH-ENERGY PLANETARY BALL MILLING

A ball milling is an innovative and very promising technique. The first, reported, notice of such technique dates back to 1870. It was extensively used to grind flint for pottery production.[45] It is still widely used in industrial processes and, in last decade, it being very appealing in the research field. The main advantage is the possibility to obtain large amounts of products through the movements of spheres on reagent's powders. It is a green and low-cost technique that do not involve high temperatures or pressures. The processes could be done both in dry and liquid-assisted conditions, employing different energies (e.g., blend or grind powders requires less energy than a proper chemical reaction). It is very versatile, suitable for a wide range of compounds, whether organic or inorganic. In addition, the possibility to control morphology, stoichiometry and purity of products represent other pillars of this technique. Nowadays, ball milling is used principally for industrial purposes in order to blend for pyrotechnics, paints, ceramics, to grind minerals or other materials with all degrees of hardness. Several types of instruments were developed in order to meet the request of industrial processes (e.g., cement mill or vertical roller mill). High-energy planetary ball milling generate energies substantially greater than the commonest mills, some characteristics are, nevertheless, similar to whose reported above.

In this case of study, a high-energy planetary ball milling is used both for synthesis and refinement purposes. This technique enables a wide variety of products in ambient conditions using at the same time non-toxic solvents. The high-energy planetary ball mill is formed by a plate on which are mounted two jars, in symmetric positions with respect to the symmetry axis. Planetary condition is created by the revolutionary movement of the plate around a motor shaft and the contemporary rotation of jars around their axis. Jars are partially filled with reagents, some grinding balls composed by the material of the same jar (e.g., agate, zirconium oxide, stainless steel, tungsten carbide, or silicon nitride), and, if necessary, a grinding media. Different sphere diameters (1 to 20 mm) are selectable according to the process energy. For example, big spheres are used to improve the solid-state reaction, while smaller spheres are required for refining. Grinding media can be very useful to reduce the particle size of a powder further; the only critical limit is not reacting with it. In particular the hardness, and so the type of materials constituting the jars, is a crucial characteristic that must be experimentally chosen depending on the relative hardness of ground materials. The surface abrasion of jars caused by the mechanical interaction with the spheres put in motion during the milling process could represent a possible problem, so the grinding specifications must always be carefully evaluated.

A mechanochemical (MC) reaction is a solid-state reaction generated by impact, friction and sliding of spheres on reagent’s powders. The whole process possesses non-equilibrium thermodynamics. Moreover, two fundamental parameters need to be mentioned: Rotation Per Minute (RPM) and Ball-to-Powder weight Ratio (BPR). Operatively, work conditions can be set up on 10-1100 RPM and 1-200 BPR. Large amounts of energy accompany the cascade of impact processes that occur in jars during milling. Microscopically, the process is described by the magma-plasma model (*Figure 2.3*).[46, 47] When a ball hits the reagents, the impact energy is dissipated through local temperature increase. Only locally and instantaneously, the formation of μ-plasmas of over 10000 K occurs. This causes the formation of very defective, thus reactive, surfaces that involve the solid-state MC reaction.

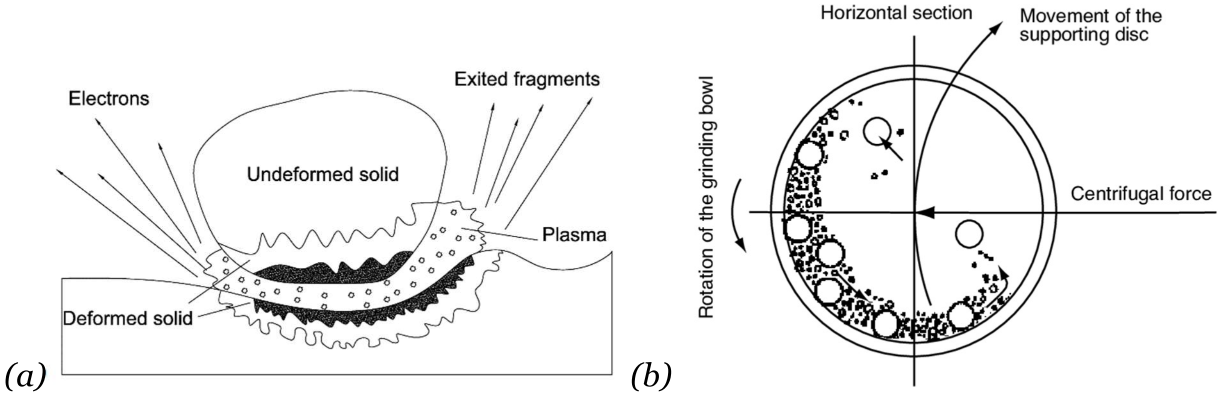

Figure 2.3: (a) Schematic representation of magma-plasma model. (b) Schematic movements of spheres and powders internal to a jar during a MC experiment.

Noteworthy, when a solid-state reaction takes place, several qualitative observations (e.g., an abrupt change of colour) usually indicate whether some chemical reactions occurred. As reported above, the surfaces created during the mechano-reaction could be highly reactive. Consequently, the presence of reactive gases like oxygen can be detrimental for the success of the reaction. In order to avoid oxidation, it is necessary to use hermetic jars, controlling the atmosphere composition, for instance adding inert gases like N_2 or Ar. A certain amount of pressurized gas during the mechano-treatment can also favour the formation of more fine product powders.

In this work, both solid-state reactions and refinements protocols were realized with two different Planetary ball Mills Fritsch (PULVERISETTE 7, *classic* and *premium* line model). Both instruments, reported in *Figure 2.4*, are suitable for dry or wet processes and are equipped with two grinding stations that can load jars of 45 ml capacity each and grinding balls with variable diameters from 1 to 20 mm. The maximum rotation speed of premium and classic line models is slightly different: 100-1100 RPM and 100-800 RPM, respectively. The premium instrument can lodge airtight jars equipped with valves which can easily allow the insertion and the removal of the inner gas before and after the mechano-processes. The materials composing both balls and jars are agate (SiO_2) and zirconia (ZrO_2).

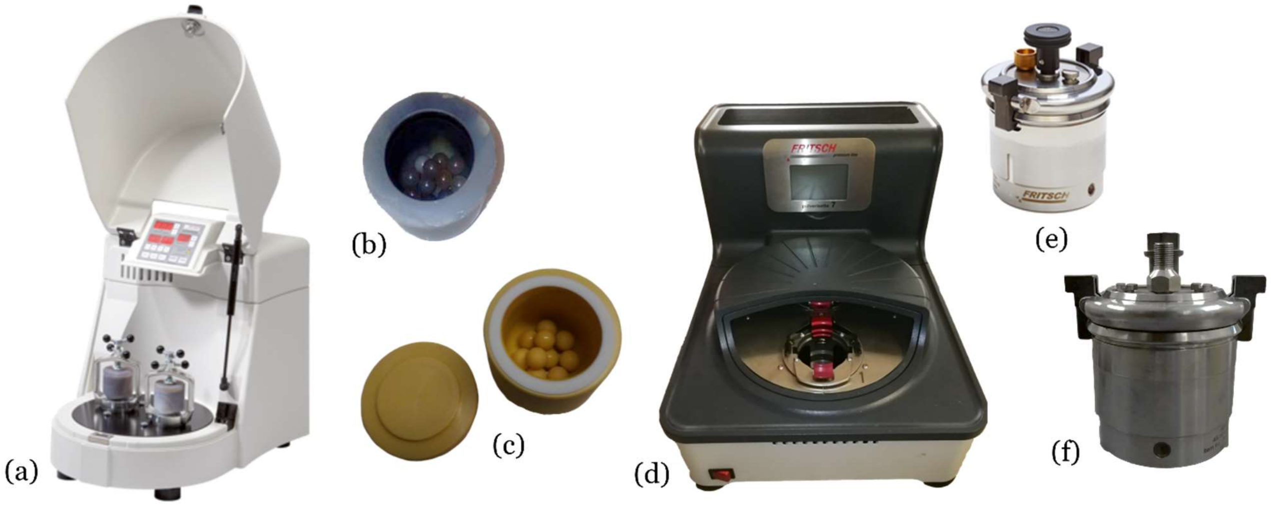

Figure 2.4: All planetary ball Mills Fritsch PULVERISETTE 7 instruments used in this work completed by proper jars and balls. (a) The classic line model holding two SiO_2 *jars. (b)* SiO_2 *jar for classic line model, partially filled of 10 mm balls. (c)* ZrO_2 *jar for classic line model, partially filled with 10 mm balls. (d) The premium line model (the lodging of a jar is clearly visible). I Typical airtight jar for premium line model. (f) Airtight jar provided with valves for injection or removal of inner gases.*

Materials can be prepared via mechano-reactions assisted by liquid conditions using both inert and reactive solvents or gases. Depending on the purpose and MC parameters, it is possible to obtain a refinement, a chemical reaction, or a re-crystallization with a liquid-assisted ball milling. More details will be provided in chapters 5 and 6.

2.3) PHOTOLITHOGRAPHY AND ETCHING TECHNIQUES

UV lithography is a common technique for the fabrication of printed circuits in microelectronics. The working steps are: (1) upon a specific surface, a thin layer of photo-sensible substance, called photoresist, is applied via spray or spin coating. Once it is dried up, (2) geometrical figures can be transferred from a pattern mask to positive photoresist through a simple UV irradiation exposure. These masks are usually made of glass or plastics while the geometrical patterns of metals or conductive pastes. After the UV light exposition (3), photoresist undergoes a photochemical reaction that makes it easily attacked by suitable solvents, called developers (4). This particular step consists of the removal of the light-exposed parts of the photoresist layer. The selective removal of photoresist impressed areas; leaves uncovered the underlying layer. At this point, it is possible to proceed in two different and opposite ways.

On one hand, (5a) it is possible to deposit a new layer of a different material; or (5b) it is possible to proceed with a selective etching (dry or wet). Last, after these two options, lift-off (6) is performed, consisting in the removal of the whole remnant photoresist and surface polishing. The final result of the procedure is an embossed or depressed pattern depending on what it was previously chosen after the development phase. For the sake of completeness, it is necessary to specify that what is explained up to this point is correct only for positive photoresists; a negative resin has the opposite behaviour.

A Microposit S1813 G2 SP15 Positive Photoresist and a Microposit MF-321 Developer (tetramethylammonium hydroxide containing) were used in this work. All the samples were exposed to 400 nm UV irradiation through a Karl Süss MJB3 Contact Mask Aligner provided of a 350W high-pressure UV mercury lamp. The maximum resolution possible was up to 2.5 µm.

In all microfabrication techniques, lithography and etching processes are both fundamental. As for the etching, the correct choice of a proper etchant, the type of process (wet or dry) and the related application times are crucial to obtain the desired product. In this work, only wet chemical etching techniques were used.

Nowadays, electronic technologies are currently pushing to reduce the size of devices. If the required resolution for a device's production is about hundred nanometres (i.e., far-UV wavelength), it is necessary to use a nanolithography approach. To have low-resolution values, it is necessary to use particular and expensive techniques, such as the Extreme Ultraviolet Lithography (EUV) which employs short wavelengths of the UV spectra;[48] Electron-Beam Lithography (EBL)[49] or Scanning Probe Lithography (SPL).[50]

2.4) THIN-FILM CHARACTERISATION

The principal instruments, techniques and parameters used to characterise the thin-films and solar devices treated in this work are listed below.

2.4.1) POWDER X-RAY DIFFRACTION (PXRD)

The PXRD is a powerful tool for discriminating the structural, crystallographic properties and also purity of a powdered sample. In the case of the present study PXRD was performed to verify the success of a MC process. Furthermore, the technique was used as a screening method to check and also evaluate the film crystalline texture and orientation. Finally, the recorded pattern was compared with the calculated reference diffraction pattern of the expected phase/s via Match! Software.[51] In all cases, the superimposition of the pertinent PXRD patterns is used to evaluate the emergence/disappearance of peaks. The material crystallites mean dimension from PXRD can be estimated via the Scherrer method, using the Eq. (2.1):

$$D_{hkl} = \frac{K\,\lambda}{B_{hkl}\,cos\theta} \qquad \text{(Eq. 2.1)}$$

where D_{hkl} is the crystallite size, λ is the X-rays wavelength, θ is Bragg's angle expressed in radians and B_{hkl} is full width at half-maximum (FWHM) of the considered reflection. K is the approximation parameter referred to the average crystallite shape, usually approximated to 0.9.[52]

Each new pattern and several texture orientations were thoroughly analysed via PowderCell software to solve the structural symmetry or estimate the degree of crystallinity. Moreover, a mismatching model was utilised to estimate the lattice mismatches between a wide selection of substrates and a solar absorber material grown by the RF-MS technique, illustrated in chapter 4.

Two powder X-ray diffraction instruments were used for the measurements: a Siemens D500 (Siemens, Berlin, Germany) and a Thermo Electron ARL Xtra. The first used a Bragg-Brentano geometry, and it was equipped with a Siemens scintillator counter C71249-A58-A19. The X-ray generator, a KRISTALLOFLEX 710, was set at 3 kV and 30 mA to produce the correct 1.54 Å K_{α}-radiation; the K_{β} was screened through a Ni filter. Thermo Electron ARL X'tra powder diffractometer was set at 30 kV and 40 mA to obtain the radiation specified above, equipped with a Si(Li) solid-state detector. Each sample was placed on a stationary zero-background sample holder and scanned over the 2θ-range 10°-

75°, with variable step size. For particular high resolution or pole figures analyses, a Rigaku Smartlab XE diffractometer equipped with Euler cradle was used. In the case of pole figures analysis, the beam was limited in the area through mobile slits; a Schultz slit was added to limit defocusing effects at high χ angles. Images were collected by a complete 360° φ analysis, divided into 5° steps. For each sample a range of 0° - 75° on χ angle was investigated and the complete data analysis was provided via home-made Matlab software made by Dr. D. Delmonte.

2.4.2) SCANNING ELECTRON MICROSCOPY AND ENERGY-DISPERSIVE X-RAY SPECTROSCOPY (SEM-EDX)

Morphological analysis as well as compositional microanalysis are highly important in material science studies. Scanning Electron Microscopy (SEM) is an effective and non-destructive technique that allows a high-resolution imaging of the surface study and, the measure of thicknesses in the case of film or layered heterostructures.

In this work, a Zeiss Auriga Compact Scanning Electron Microscopy mounting a Field Emission Gun (Schottky-type) source (FEG-SEM) was used for routine analyses. The FEG source has the characteristic to focalise the electron beam better to obtain a higher resolution as a common SEM. This instrument can indeed reach 1.2 nm of resolution at 15 kV; anyway, voltage is modulable in the range between 100 V and 30 kV. The operating currents can vary between 4 pA and 100 nA, whilst magnification can start at 12 X and reach, in ideal conditions, 900 kX.

However, the electron beam is usually set to work between 5 and 20 kV and within the magnification range between 500 X and 100 kX. InLens and Everhart-Thornley detectors were used (for higher and lower resolution, respectively). The instrument was equipped with an Oxford Energy Dispersive X-Ray Spectrometer detector for the compositional microanalysis. Routine analysis with this instrument included layer thicknesses or granulometry evaluation, morphology studies and EDX compositional microanalysis.

2.4.3) CONTACT PROFILOMETER ANALYSIS

A contact profilometer was used to determine thin-film roughness, chemical-etched surface profiles and, when possible, thickness (e.g., calibration of CBD processes and setups).

The instrument enable a combination of an Alpha-Step 100 Profilometer (220 V, 50 Hz, model 10-00040) and a Surface Profilometer (220 V, 50 Hz, model 10-00020); KLA TENSOR INSTRUMENTS provided both parts of the instrument. A mobile plate hold the samples on the profilometer countertop. The positioning of the sample, the choice of the area to be analysed and the tip position during the measurement could be controlled through the ocular of the instrument. Simultaneously, moving the tip on the sample, the nib of the alpha step profilometer record on a graph paper the profile of surface depending on the sensitivity (from 2 nm to 100 μm). An additional tool allowed the tip to move at different speed to emphasise the resolution of the profiles.

2.4.4) CURRENT-VOLTAGE MEASUREMENTS OF A PV JUNCTION

It is clearly of fundamental importance to study the electric properties of PV devices. When two different doped semiconductor layers are put in contact, a p-n junction is created, as reported in paragraph 1.4. In dark conditions, this junction is characterized by a depletion layer with no free charges. For this reason, a relatively small electrical field can be measured in open circuit configuration (V_{oc}). This field is directly influenced by the doping rate of materials as well as the power and spectral characteristics of the irradiation and it works like a driving force for the photogenerated electron-hole pairs' drift towards opposite direction throughout the junction when the device is illuminated and short circuited (I_{sc}). This phenomenology, synthetically described above, can be explained in detail, introducing all the cell parameters.

A p-n junction in dark condition is fully comparable to an ideal diode; this behaviour can be explained through an ideality factor. Once the current and voltage of an ideal diode are considered, it is possible to calculate an I-V curve (Eq. 2.2),

$$I = I_L - I_0 \left[exp\left(\frac{qV_{Oc}}{nkT}\right) - 1 \right] \qquad \text{(Eq. 2.2)}$$

where I_L is light-generated current, I_o is the current in dark conditions, n is the ideality factor, T is the operating temperature and again, V_{oc} is the voltage measured in open circuit. For small V_{oc}, the exponential term is >>1, the Eq. (2.2) could be simplified and rewritten as shown in Eq. (2.3).

$$I = I_L - I_0 \left[exp \left(\frac{qV_{0c}}{nkT} \right) \right] \tag{Eq. 2.3}$$

When exposed to light, the PV device starts to generate power and the current is generated. The entire I-V curve will be shifted coherently with the current value; if the irradiation increases, the more the current photogenerated, the bigger the shifting will be. Conventionally, the I-V curve is flipped in order to remain in the first Cartesian quadrant. In *Figure 2.5*, it is reported a characteristic I-V curve, completed with the principal parameters that will be discussed as follows.

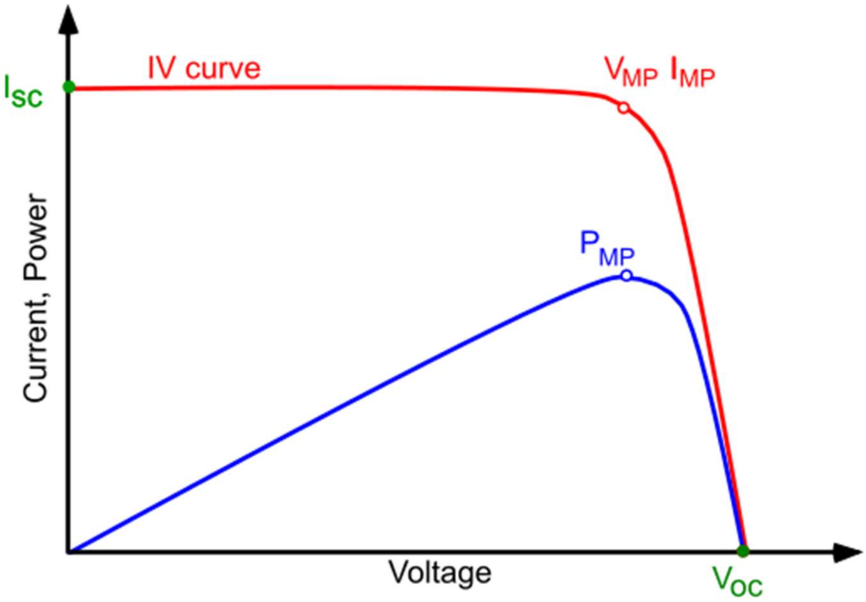

Figure 2.5: A typical I-V curve (red line) and the corresponding power curve (blue line). The most critical parameters treated in this paragraph for solar devices are represented.

From I-V curves, it is possible to extrapolate almost all the photovoltaic parameters. The short circuit current (I_{sc}) is the direct consequence of the generation and collection of photogenerated carriers; it is the maximum current extractable from the device at zero voltage. I_{sc} depends on several factors, such as the active device area, the incident spectrum of light (e.g., AM1.5) or secondary phenomenon caused by the light (absorption or reflection). This parameter is very important, and it represents how many carriers can diffuse across the material. If I_{sc} is divided for the active device area (A), it is possible to obtain the short circuit density (J_{sc}). Rearranging the Eq. (2.3), it is possible to obtain the maximum value of the voltage at zero current (V_{oc}), when the circuit is open. This important parameter is affected by the quantity of the incident light and operating temperature (under the same light irradiation, a device would have its best performances at low temperatures rather than high ones). The scalar product between voltage and current can be graphically represented as the power curve. To have the maximum output power, the device should work at the highest possible values of real power (P_{MP}), voltage (V_{MP}) and current (I_{MP}), as reported in Eq. (2.4).

$$P_{MP} = V_{MP} \cdot I_{MP} \qquad \text{(Eq. 2.4)}$$

Eq. (2.5) also indicates the fill factor (FF). It is the primary parameter that is obtained with the direct comparison between the P_{MP} and the ideal power value, represented by the product between J_{sc} and V_{oc}. The FF could be graphically represented as a rectangle, fitting the I-V curve. This concept is represented in *Figure 2.6*.

$$FF = \frac{V_{MP} \cdot I_{MP}}{V_{OC} \cdot I_{SC}} = \frac{P_{MP}}{V_{OC} \cdot I_{SC}} \qquad \text{(Eq. 2.5)}$$

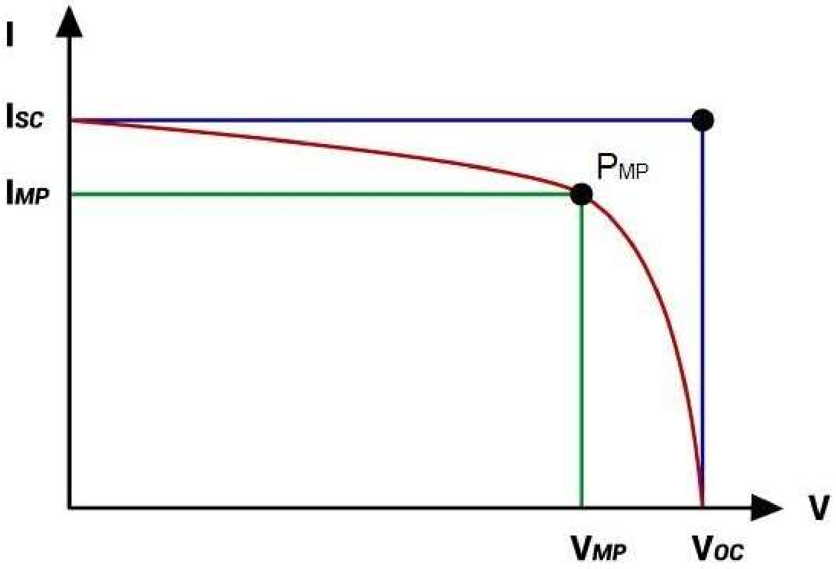

Figure 2.6: Graphical representation of Fill Factor, limited by the green rectangle.

Another fundamental parameter of a PV device is the Power Conversion Efficiency (PCE or, simply, efficiency). It is the ultimate quality index of a PV device. It is calculated by dividing the maximum output power of the cell, from which a significant part of parameters described until this point depends, and the incident sunlight power Eq. (2.6).

$$\eta = \frac{P_{max}}{P_{in}} = \frac{V_{OC} \cdot I_{SC} \cdot FF}{P_{in}} \qquad \text{(Eq. 2.6)}$$

In ambient conditions, under AM1.5 irradiation, the value of P_{in} is standardised at 100 mW/cm^2.

The deviation from the ideality is principally caused by recombination points (physical defects of layers or electrical band alignment failures) that could significantly reduce the device performances.[53] In addition, two values of resistance play a major role: the series resistance (R_s) and the shunt resistance (R_{sh}). R_s is influenced by the lack of ohmic contacts between different device layers (e.g., between substrate and absorber). The absence of straight paths for the carriers during the current extraction can increase R_s very quickly. For example, due to an absorber layer constituted by a disordered distribution of little grains instead of large crystalline units. This means that surface/volume ratio is disproportioned towards surface so that the carriers will have difficulties reaching their respective contacts causing a sharp increase of the measured R_s. Shunt resistance (R_{sh}) is principally related to manufacturing defects of the cell. A low value of R_{sh} causes significant power losses with consequent imbalance in the carrier transport. Graphically, FF, the total area of an I-V curve, for a device affected by extreme series and shunt resistances would be significantly lowered (as represented in *Figure 2.7*).

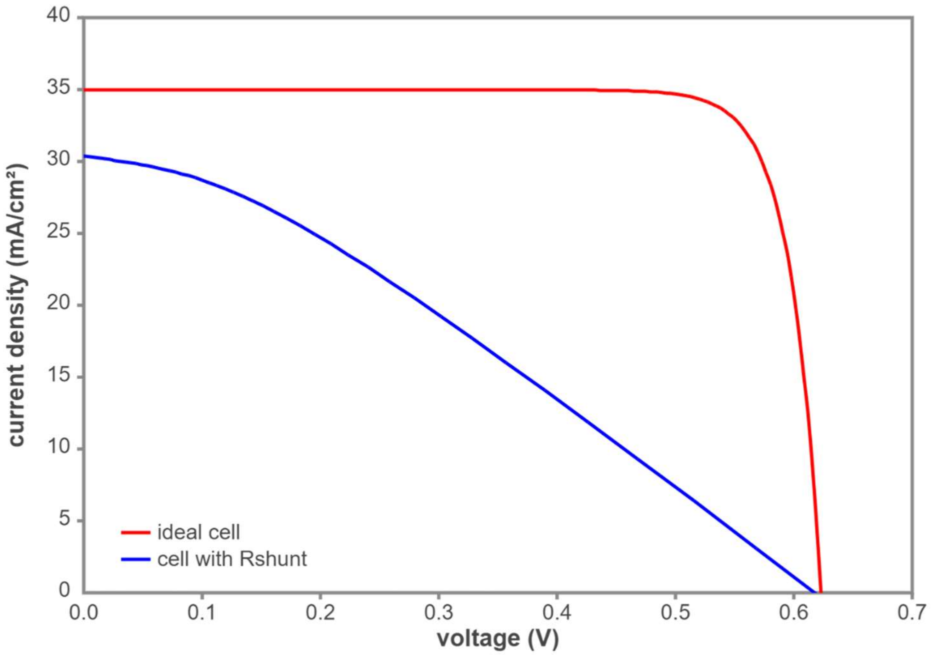

Figure 2.7: Power curve (blue line) influenced by a $R_s > 15\ \Omega{*}cm^2$ *and* $R_{sh} < 100\ \Omega{*}cm^2$ *compared to an ideal diode I-V curve (red line).*

In this work, the numerical simulations of the device performances are performed using wxAMPS software. The solar cell J-V characteristic is calculated using the continuity equations for holes and electrons and the Poisson equation. The current density-voltage (J-V) characteristics of the solar cells were collected by using a Keithley 2614B Sourcemeter and an AAB solar simulator (ABET SUN 2000) under Standard Test Conditions (AM1.5G, 25°C). Finally, resistance and transport measurements were collected through the Seebeck effect.

2.5) MATERIALS

Different materials have been studied as part of a thin-film PV device during this work. In the following paragraphs, I report a detailed presentation of the main investigated materials.

2.5.1) ANTIMONY SELENIDE (ASe)

Antimony selenide (Sb_2Se_3, ASe) is a promising binary chalcogenide suitable for high-efficiency single-junction PV devices, thanks to its intriguing semiconductive properties.

This compound combines the necessity of using low cost, earth-abundant, and low toxic materials in 2 G PV technologies. Thanks to a direct optical bandgap of 1.1-1.3 eV and high absorption coefficient (10^5 cm^{-1} at 600 nm[54]), this material could achieve a theoretical 30% conversion efficiency, accordingly to SQ theory.[55] ASe is a p-type semiconductor that shows strong anisotropic properties. This work used the reference JCPDS Card No. 15-0861, and the Pbnm space group was chosen to describe ASe's orthorhombic structure (a = 11.62Å, b = 11.77 Å, c = 3.962 Å). The $(Sb_4Se_6)_n$ units, covalent bonded, form a ribbon-like order along [001] direction, as shown in *Figure 2.8 (a)*. Along the two other main crystallographic directions [100] and [010], the ribbons are linked just via weak VdW interactions. The structure could be considered a quasi-1D array of ribbons that strongly influence the physical properties and specific lattice directions. The carrier's mobility, in particular, reaches 45 cm^2/V along the ribbons direction, while it is almost negligible between them.[56] This could be explained by hopping conduction due to the weak bonds present between ribbons. Therefore, it is fundamental the correct crystal growth and orientation control of this material during the layer deposition, to guarantee high performances: this in particular occurs when the c axis of ribbons is perpendicular to the substrate, as reported in *Figure 2.8 (b)*. ASe could be prepared through several methods such as thermal evaporation,[57] LT-PED,[58] or RF-MS.[59, 60] By now, the maximum efficiency achieved in literature is 9.2%, obtained via Close Space Sublimation (CSS).[54]

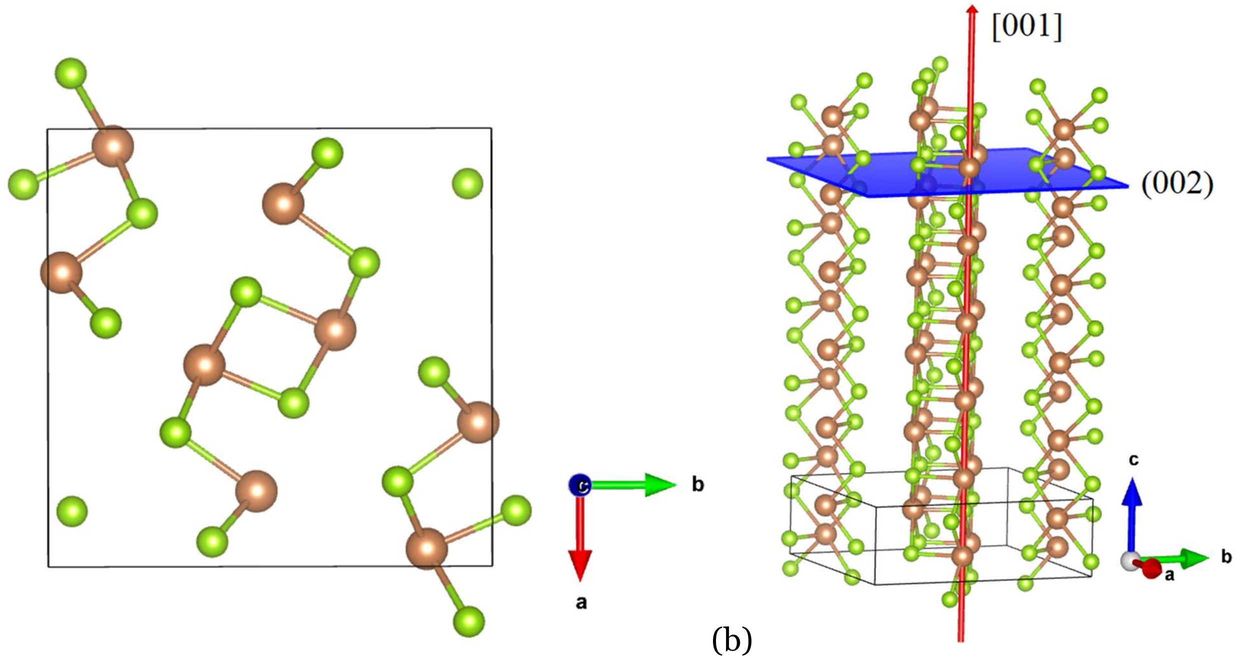

(a) (b)

Figure 2.8: (a) ASe (JCPDS Card No. 15-0861) unit cell perpendicular to the c axis, noticeable the $(Sb_4Se_6)_n$ *unit (Sb and Se, brown and green dots, respectively). (b) Schematic representation of ASe ribbons oriented in (002) reflection, parallel to the c axis. The grain growth perpendicular to a substrate is necessary to achieve the maximum conversion efficiency.*

2.5.2) COPPER INDIUM SULPHIDE (CIS)

$CuInS_2$ (CIS) is a ternary semiconductor with a direct bandgap of 1.53 eV, high absorption coefficient (10^5 cm^{-1}), and earth-abundant (apart from In), non-toxic elements. The good carrier concentration (6×10^{17} to 2×10^{18} cm^{-3}) and mobility (412 $cm^2V^{-1}s^{-1}$) at RT make CIS an excellent p-type semiconductor.[61] In addition, CIS has a high theoretical limit of PCE calculated over the 28%. Despite the excellent properties and the higher bandgap given by the anionic exchange, CIS is less common than $CuInSe_2$ (CISe). The reason of that is related to a different ease of deposition of S with respect to Se; in fact, sulphur has a very high vapour pressure compared to the selenium, so many common techniques, as the melt-growth based techniques, used to produce selenides, cannot also be applied to sulphides. Nevertheless, in recent years, techniques like solvothermal synthesis,[62] electrodeposition,[63] solution spin coating,[64] High Pressure/High Temperature synthesis,[65] Hot Isostatic Pressure (HIP) or Planetary Ball Milling[66] have been developed to overcome the above issue. In the last work, pure CIS phase was obtained by mechanosynthesis; then a densified pellet was produced starting from the powders and used as target for PVD depositions (e.g., RF-MS, PLD or LT-PED).

CIS crystallise in three different crystal structures. The most common compound at RT and RP is the tetragonal chalcopyrite-type phase (α-CIS), belonging to the I-42d space group [*Figure 2.9 (a)*]. At higher temperatures and in particular composition ratios, cubic sphalerite also exists (δ-CIS) and hexagonal wurtzite (β-CIS or γ-CIS, depending on the In content and space group). CIS is completely isostructural to CISe; it is possible to fully understand the phase diagram presented in *Figure 2.9 (b)*. It clearly explains the complexity of Cu_2Se-In_2Se_3 pseudobinary alloy.[67] Furthermore, metastable, and disordered polymorphs have been observed under different conditions.[65] The presence of so many phases and polymorphs are one of the primary reasons why the maximum PCE reached is only 12.5%.

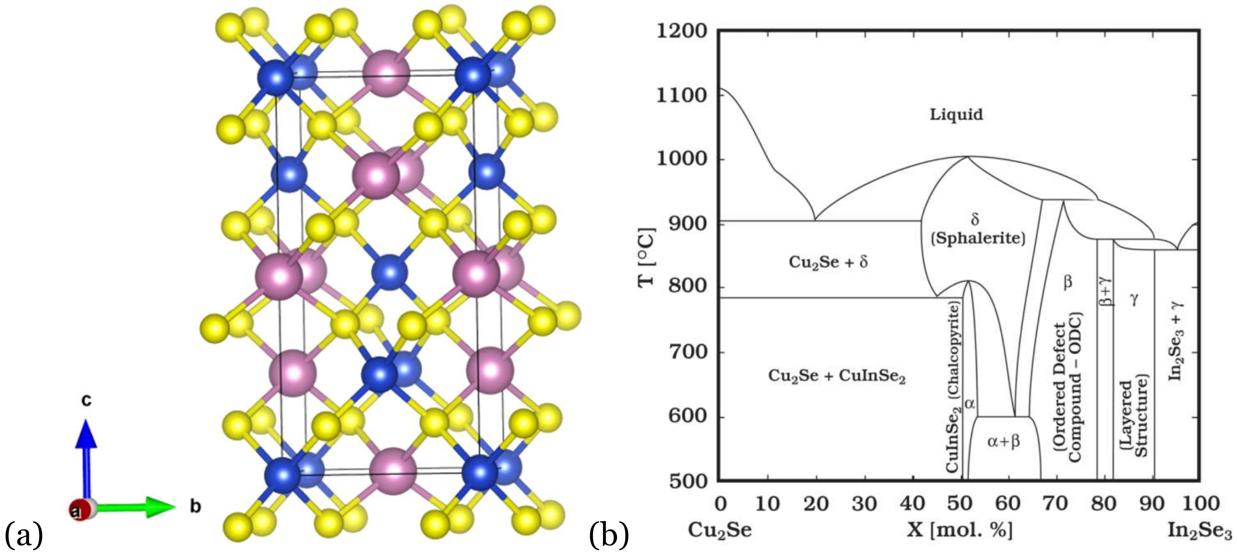

Figure 2.9: (a) Chalcopyrite α-CIS structure (Cu, In, and S atoms are indicated with blue, pink, and yellow spheres, respectively). (b) Phase diagram of Cu_2Se-In_2Se_3 pseudobinary alloy in which are present the chalcopyrite (α), sphalerite (δ), and wurtzite (β or γ) type for CISe.[67]

2.5.3) COPPER INDIUM GALLIUM SELENIDE (CIGSe)

$Cu(In_{1-x}Ga_x)Se_2$, also known as CIGSe, is a chalcopyrite solar absorber with tetragonal symmetry [*Figure 2.10 (a)*] and high p-type conductivity (10^{15} -10^{17} cm^{-3}). Thanks to a tunable bandgap (1.04 – 1.68 eV), relatively low cost, high absorption coefficient ($\alpha > 10^5$ cm^{-1}) and efficiencies that overcome easily 20% at lab scale, it is one of the most common chalcogenides studied in second-generation PV technologies.[68] CIGSe thin-films can be grown with several techniques such as co-evaporation,[69] electrodeposition,[70] RF-MS,[71] or LT-PED.[72]

CIGSe is a pseudobinary alloy of two ternary compounds, $CuInSe_2$ (CISe) and $CuGaSe_2$ (CGSe); it can be considered a simple Ga substitution in α-$CuInSe_2$ (α-CISe) crystal sublattice. However, the most explicative composition diagram is given by a pseudoternary compound system of Cu_2Se-In_2Se_3-Ga_2Se_3 [*Figure 2.10 (b)*].[66] As reported above in [*Figure 2.9 (b)*], CISe exists in four different phases as well as for CIGSe. The primary phase is α-CIGSe, which has the characteristic tetragonal chalcopyrite structure (Ch) with a rich group III composition. β-CIGSe (P1) and γ-CIGSe (P2) are two Ordered Defect Compounds; both are poor in gallium, but γ-CIGSe is very indium-rich. At last, δ-CIGSe is a compound with a disordered zincblende (Zb) structure that forms only at high temperatures. Given the quaternary nature of CIGSe, it follows that the melting point is incongruent, and it is not easy to deposit such material in a single-stage process. Moreover, the p-type conductivity is generated by Cu vacancies and extrinsic doping of some alkaline cations (e.g., Li$^+$, Na$^+$ or, K$^+$). Among all techniques reported above, only LT-PED and RF-MS succeeded in depositing CIGSe in a single step process while others often require post-deposition treatments to adjust the material stoichiometry. In this work, CIGSe was deposited only through LT-PED, using targets prepared by a lab-scale modified-Czochralski apparatus.

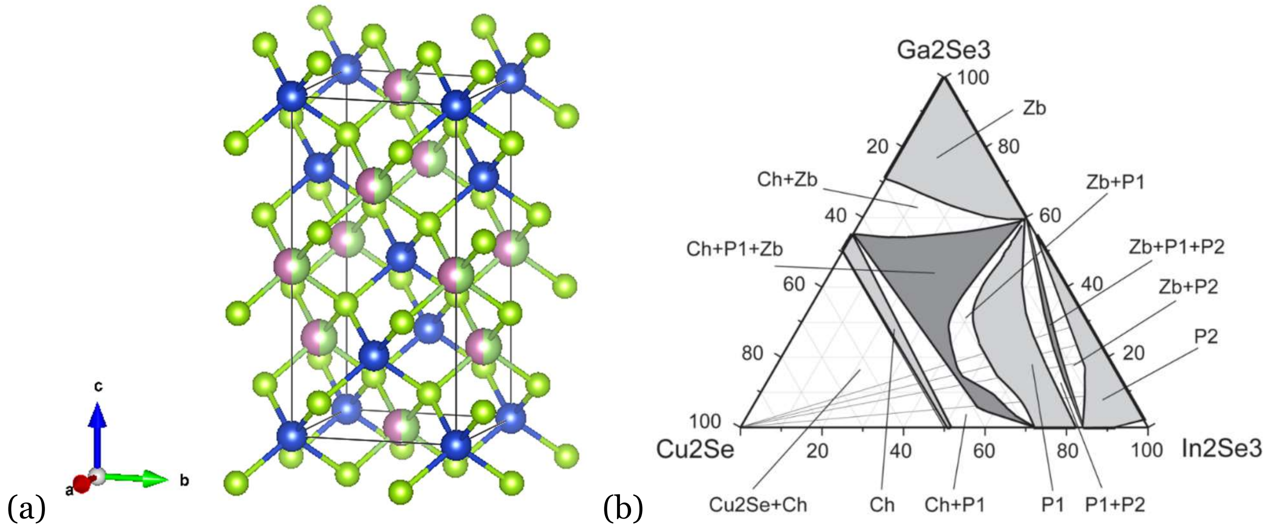

Figure 2.10: (a) Tetragonal structure of CIGSe in which large spheres in half colour represent the disordered sites of indium (pink) and gallium (green), which ratio may vary with stoichiometry. Small solid blue and green spheres represent copper and selenium, respectively. (b) The complexity of Cu_2Se-In_2Se_3-Ga_2Se_3 pseudo-ternary compound system. Ch, P1, P2, and Zb are, respectively, references of α-, β-, γ-, and δ-CIGSe.[66]

The LT-PED deposition was carefully studied in past years to minimise the incongruent evaporation and maximise the crystallinity, using relatively low temperature (< 300°C).[73, 74] It is well known that alkali-doping is mandatory to increase the performances (J_{sc}) and improve the electrical passivation of grain boundaries. Microscopically, alkali doping generally reduces the recombination processes and the p-n junction defects favouring the extraction of the photocurrent.[75-77] A generic thin-film grown on a commercial substrate (e.g., glass/Mo or glass/TCO) is directly doped via diffusion processes involved by high-temperature annealing. This allows alkali to diffuse from the underlying glass to the absorber, creating an ohmic contact. This statement is true for several solar absorbers. However, this is not possible in the case of LT-PED due to the low temperatures and short deposition times involved in the processes (270°C, 20 minutes for CIGS). In this case, it is necessary to deposit a very tiny layer of dopant (NaF) on the substrate surface (~15 nm, 0.1 % ÷ 0.4 % at.%) before depositing the absorber. Relatively Low-temperature deposition and subsequent rapid thermal annealing are then enough to allow the alkaline layer to diffuse along the absorber layer, as represented in *Figure 2.11*. For sake of completeness, it is necessary to specify that, if the substrate material is different from soda-lime glass (e.g., stainless steel) it would be necessary to add a thin layer of alkaline dopant to favour its diffusion.[78]

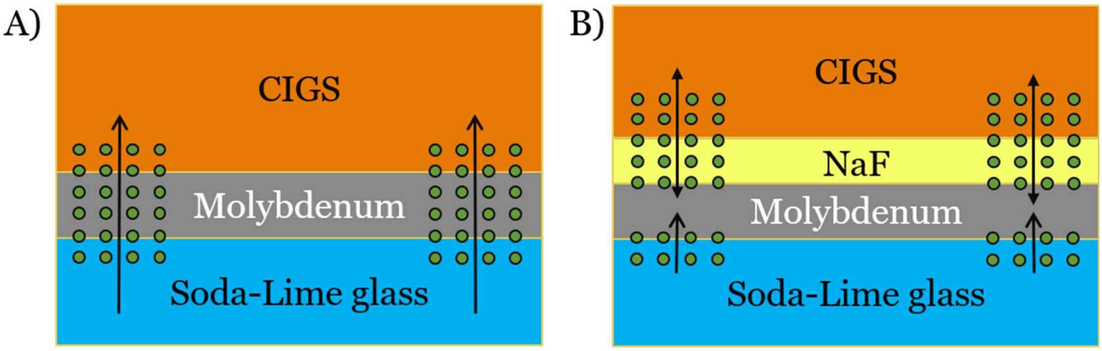

Figure 2.11: Dopant diffusions dynamics for A) generical high-temperature thin-film deposition technique for a Glass/Mo/CIGS architecture, like co-evaporation and B) LT-PED case by interposing a thin layer of dopant between Mo and CIGS layers.

2.5.4) CADMIUM SULPHIDE (CdS)

CdS is a yellow inorganic compound that occurs naturally as an impurity in sphalerite (ZnS) ores. It possesses two different polymorphic mineral forms: greenockite and hawleyite, with hexagonal and cubic symmetry, respectively. It is straightforward to obtain it in pure form, and it is the principal source of cadmium for the industry. Due to its aspect, low cost, and easy availability, it was historically used as a pigment (in substitution of chromium-yellow) by various artists during the 19th and 20th centuries (e.g., Van Gogh, Monet, Pollock, or Munch), despite the confirmed carcinogenic and teratogenic properties. Nowadays it is still used for this purpose but only in plastics or varnishes.

CdS is an n-type semiconductor for each polymorphs, with a yellowish colour, due to a wide direct bandgap (2.42 eV).[79] It is widely used in the transistor, optic, and electronic industries.[80-82] In addition, it is one of the most common and stable materials which is applied as buffer layer thin-film PV technologies. The wide bandgap is fundamental to align the electrical bands between the absorber and the front contacts, thus allowing a perfect charge extraction and limiting the absorption of wavelengths useful for the underlying p-type semiconductor [*Figure 2.12 (a)*]. Furthermore, CdS, despite its high bandgap, possesses a good electrical conductivity and thin-films are generally homogeneous and nanocrystalline, avoiding shunt circuit processes in devices [*Figure 2.12 (b)*].

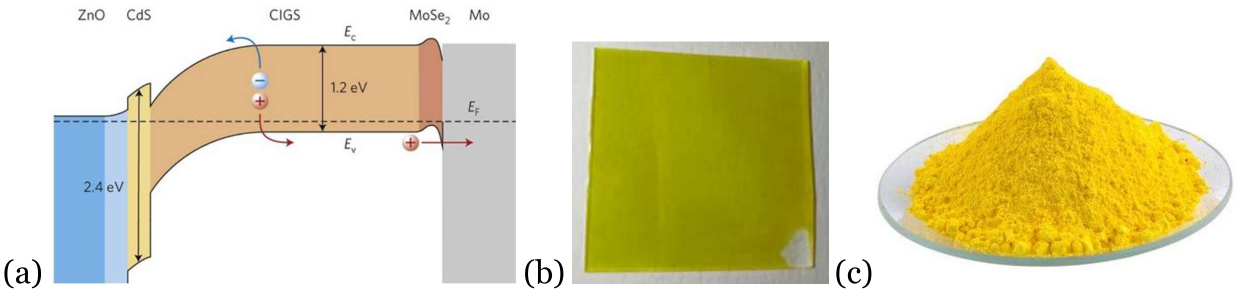

Figure 2.12: (a) A typical example of band alignment in a thin-film PV device, notice the fundamental CdS role connecting the absorber (CIGS) electronically with the window layer (ZnO). (b) CdS thin-film deposited via CBD on bare SLG (90 nm thick). (c) Pure CdS powder.

Enduring and high quality CdS thin-films for PV applications are commonly prepared via vacuum or wet techniques (e.g., RF-MS or CBD, respectively). The latter was chosen in this work, for its versatility, low cost, and the possibility to deposit CdS on different substrates (e.g., SLG, metals, polymers, or flexible materials).[83] As specified in paragraph 2.2.3, CBD is a delicate process in which many factors can play a crucial role. The concentration of precursors and complexing agents, temperatures and times all influence the success of the deposition.[79, 84] Despite the critical applications and inexpensive equipment, CdS does not represent the future of the 2 G photovoltaic due to its high toxicity. Therefore, researchers are intensively studying Cd-free buffer layers, such as ZnS, In_2S_3 or $BiVO_4$.

2.4.5.1) STANDARD CdS PROCEDURE

When preparing CdS by CBD, fresh standard stock solutions are prepared every time necessary with high-purity chemicals (Sigma-Aldrich). A 0.1 M $CdSO_4$ stock-solution was obtained, dissolving 2.08 g of $CdSO_4$ in a 100 mL volumetric flask and 19.03 g of thiourea [$CS(NH_2)_2$] are dissolved in a 250 mL volumetric flask to obtain a 1 M aqueous solution. To obtain the reactive cation (Cd^{2+}), a complexing reagent is needed. It is chosen fresh ammonia (NH_3, 28% v/v, NORMAPUR).

Each deposition took place in a standard 100 mL beaker immersed in a thermostatic bath at 60°C; with no stirring. The samples are immersed in the reactive bath by a Teflon-homemade clamp that allow the complete immersion perpendicularly to the solution. Standardizing all the above parameters is fundamental to control the fluid dynamics of growing nanoparticles and the whole deposition process.

The solution pH is adjusted around 11 and 62 mL of distilled water are mixed with 7.5 mL of NH_3 28% (v/v) to obtain the complexing agent NH_4OH Eq.(2.7).

$$H_2O + NH_3 \leftrightarrow NH_4OH \qquad \text{(Eq. 2.7)}$$

Subsequently, 2.5 mL of stock-solution of $CdSO_4$ are added. In presence of low concentrations of NH_4OH, the formation of $Cd(OH)_2$ occurs Eq. (2.8). Cadmium hydroxide is an unavoidable species, and it can form thin layers on substrates. In the first instance, $Cd(OH)_2$ favours the CdS nucleation, but if present in excess on the sample surface, it can form a proper layer that can determine some parasite electrical behaviour in the PV device. For the above reasons, $Cd(OH)_2$ is always limited by adding $CdSO_4$ in the highly concentrated ammonia solution. Thus, the transition from Eq. (2.8) to Eq. (2.9) is almost instantaneous with the formation of Cd reactive complex $Cd(NH_3)_4^{2+}$.

$$CdSO_4 + 2NH_4OH \leftrightarrow Cd(OH)_2 + (NH_4)_2SO_4 \qquad \text{(Eq. 2.8)}$$

$$Cd(OH)_2 + 4NH_4OH \leftrightarrow [Cd(NH_3)_4]^{2+} + 2OH^- + 4H_2O \qquad \text{(Eq. 2.9)}$$

After the Cd^{2+} solution thermalization of 10 minutes, 8.5 mL of thiourea stock-solution are added to create the SH^- reactive species driven by the alkaline conditions (see Eq. 2.10). Finally, thanks to the combination of Cd^{2+} complex cation and SH^- anion, the CdS is formed first as a suspension in metastable conditions (ideal for a CBD) then as precipitate Eq. (2.11).

$$CS(NH_2)_2 + OH^- \leftrightarrow CN_2H_2 \uparrow + SH^- + H_2O \qquad \text{(Eq. 2.10)}$$

$$[Cd(NH_3)_4]^{2+} + SH^- \leftrightarrow CdS \downarrow + NH_4^+ + 3NH_3 \uparrow \qquad \text{(Eq. 2.11)}$$

The samples are inserted in the reactive bath only at the beginning of the last reaction, i.e., when all the SH^- reagent is formed and the solution turns to pale yellow coloration.

Figure 2.13 reports the experimental calibration curve; a typical 60 nm thick CdS layer, requires 12.5 minutes.

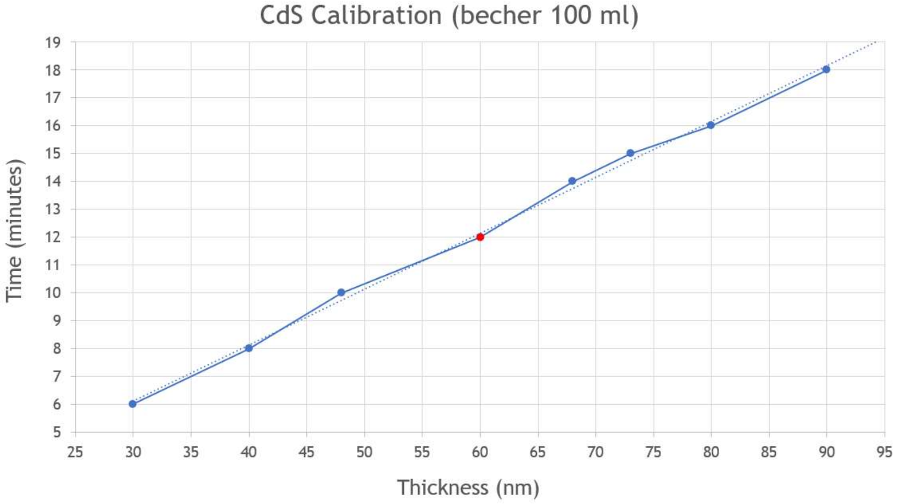

Figure 2.13: Calibration line time over the thickness of a standard CBD experiment on bare SLG for CdS. The red dot indicates the standard deposition thickness (60 nm).

CHAPTER 3

BIFACIAL SOLAR DEVICES WITH INNOVATIVE EMBEDDED GRIDS SUBSTRATES

3.1) INTRODUCTION TO BIFACIAL SOLAR CELLS

Bifacial solar cells (BFSC) are innovative thin-film devices which are in principle designed to collect and convert light from both sides. The first studies on bifacial (BF) active devices starting from Si based solar cells are dated back to 1961, in a patent by H. Mori,[85] while the first working device was indeed developed in 1975 by the Soviet Space Program Solyut.[86] From their first uses, limited to the aerospace industry, BFSC are experimenting a rapidly growing interest. In particular, BFSC devices are suitable for collecting both albedo light from the back face and direct sunlight from the front face. This is a potentially great improvement in terms of the performances of a stand-alone cell since, once a surface area is set, a double-sided photo-active device can yield more energy (theoretically up to 50%).[87, 88] Due to a quick improvement of technology, the cost of such devices has fallen quickly in the last decade, and the main application has immediately designed for high power photovoltaic.[89] Best performances can be obtained in places of an exceptionally high albedo value (e.g., desertic, polar, uncultivated fields or concreted urbanised areas).[90] In addition, a secondary field of application could be found in BIPV or PIPV. BFSC modules can be integrated into canopies [*Figure 3.1 (a)*], parasols or even act as windows or panelling for buildings.[91]

The studies on silicon-based BFSC are numerous, while those based on other materials are very scarce.[92] Besides Si, BFSC has been developed in recent years on TFSC with perovskites,[93] kesterites[94] or dye-sensitised absorbers layers in different architectures.[95] Silicon must be treated in order to obtain a second active rear surface. To avoid undesired reflections and passivation, the semiconductor must be polished, opportunely doped, and protected with a proper material (e.g., SiN_x). Thin-film BFSCs are more versatile for cost, flexibility, and semi-transparency behaviour. In this case, the main problem is represented by overheating and consequent rapid deterioration of cells. Both types of devices see a rise of carriers compared to those active from only one face but also several common issues: (1) correct tilt of the modules with respect to the ground reference is mandatory to peak and maximise mutual performances from both active surfaces;[96] (2) the light absorbance carried out by both sides of the cell grants a rise of carrier's concentration and reflections between layers, recombination processes and parasite currents.[97]

Given a BFSC cell properly installed and illuminated on both sides, it is impossible to discriminate and separate front and rear contributions to the current. For this reason, several methods of characterisation have been implemented. The first validated method, primarily used in the past, separates each contribution by illuminating selectively and perpendicularly the top and the back surfaces to quantify the difference on I-V profiles of each contribution. Thus, the role of recombination's processes in reducing the total amount of produced photo-power is estimated. It corresponds to the direct sum of photo-power when each surface is independently illuminated from the front and from the rear, once the system is set and oriented in order to collect light from both sides.[98] In this case, we talk about front, back and BF parameters obtained via selective irradiation. BF parameters are represented by the ratio between front and back contributes,[92] as reported, in Eq. (3.1) for the PCE:

$$Bifaciality\ factor\ (\%) = \frac{(PCE_{BACK})}{(PCE_{FRONT})} \times 100 \qquad \text{(Eq. 3.1)}$$

Similarly, it is possible to calculate short circuit currents (J_{sc}) and output powers (P_{max}). As reported in paragraph 2.4.4, PCE is directly dependent on J_{sc}. A method proposed in 2011 by Kreinin et al.[99] calculated the BF short current recording directly and simultaneously from the front and back to evaluate all BF parameters with more accuracy. Subsequently, Edler et al.[100] first introduced a specific mirror apparatus to contemporarily collect data from both sides. A mathematical model corroborated the effectiveness of the latter method just a few years later,[101] and, by now, this is the best method available for the characterisation of BFSC. The last cited is the method chosen for investigating bifaciality in our cells during this work.

The method applied to fabricate thin-film BFSC is comparable to the one standardized at IMEM for producing TFSC based on chalcogenides via LT-PED: in fact, the typical utilized architecture forecast the same overall heterostructure as reported in *Figure 3.1 (b)*.

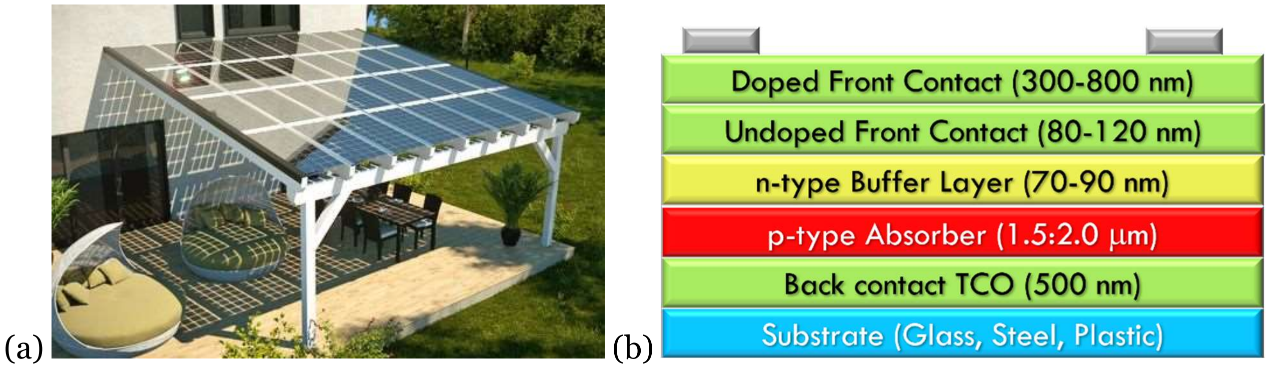

Figure 3.1. (a) Project for a BFSC canopy. (b) Classical architecture of a thin-film BFSC.

The main difference with respect to a high performing TFSC grown by LT-PED is the replacement of Mo back contact with a TCO. This operation in principle is not free of consequences on the cell functionalities: a problem of the alignment of the bands between the absorber layer and the TCO could not guarantee the ohmicity of the back contact. Furthermore, many techniques, which can be employed to prepare thin-films of TCO materials, may act in modifying also the quality of the surface, determining the formation of very thin layers of dielectric oxides (e.g., Ga_2O_3), detrimental for PV performances of devices.[102] It was discovered that low-temperature deposition techniques like LT-PED, thanks to its gentle thermodynamic operating regime, allows to avoid the formation of such dielectrics, preserving the quality of the back contact.[103] The choice of a proper TCO bottom layer (e.g., FTO, ITO, AZO), can permit to study the maximisation of the performance. The most performant transparent materials are, at our knowledge, FTO and ITO, even though the electrical interface between the absorber layer and TCO is worse than that obtained with metals, yet.[102, 104] In order to improve the performances of a BF device a new engineered solution could be used. The use of a metal grid, completed with TCO windows, could link the good hole collector properties of metals and the transparent behaviour of TCOs.

In this chapter, a particular experimental issue such a topics will be faced: *is it possible to further increase performances of a bifacial thin-film solar cells improving at the same time active area??*

3.2) NEW ENGINEREED Mo:ITO EMBEDDED BACK CONTACTS

Recent studies on BFSC, as some of those reported in the previous paragraph, mention about different performances on similar devices with the same architecture, driven only by the changing of the TCO material as back contact element. *Figure 3.2* reports all remarkable PV parameters of two devices studied by Cavallari et al.[103], in which FTO and ITO were alternatively tested within the same architecture: this comparison points out that FTO is the better than ITO for BFSC. Despite the similarities between voltages (V_{oc}) and short circuit currents (J_{sc}), fill factors and efficiencies are larger in the FTO case. Good contact ohmicity is observed for both and consequently R_s and, even if R_{sh} are pretty low, the higher values (about 60% of increment with respect to ITO) have been detected for the FTO-based device.

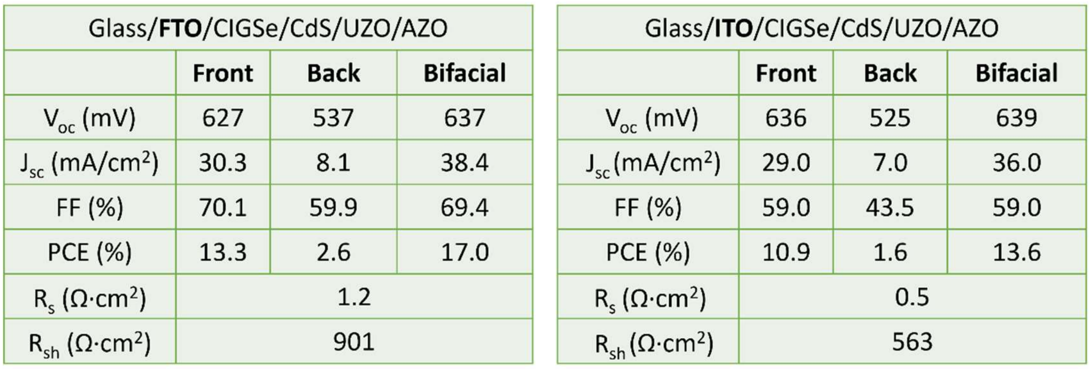

Glass/**FTO**/CIGSe/CdS/UZO/AZO			
	Front	**Back**	**Bifacial**
V_{oc} (mV)	627	537	637
J_{sc} (mA/cm^2)	30.3	8.1	38.4
FF (%)	70.1	59.9	69.4
PCE (%)	13.3	2.6	17.0
R_s (Ω·cm^2)	1.2		
R_{sh} (Ω·cm^2)	901		

Glass/**ITO**/CIGSe/CdS/UZO/AZO			
	Front	**Back**	**Bifacial**
V_{oc} (mV)	636	525	639
J_{sc} (mA/cm^2)	29.0	7.0	36.0
FF (%)	59.0	43.5	59.0
PCE (%)	10.9	1.6	13.6
R_s (Ω·cm^2)	0.5		
R_{sh} (Ω·cm^2)	563		

Figure 3.2. Comparison between PV electrical parameters for thin-film BFSC with FTO or ITO as back contact (active area <0.1 cm^2), as taken by Ref. 100.

In order to further improve the performances, thin metallic layers (Mo) were deposited on TCOs or vice-versa. This path leads to failure because smoothness and flatness of back contacts are strictly required for a CIGSe deposition via LT-PED. Furthermore, precision in the order of microns is required to prepare such back contacts. For the reasons listed above, it was chosen to test a photolithographic process to embed metal grids directly in TCO.

Specifically, two different paths were carefully developed; the only discriminant was the type of substrate's back contact material: metallic (Mo) or TCO (FTO, ITO). In *Figure 3.3*, it is schematically reported the flowchart of the whole process carried out in order to obtain a proper embedded grid sample. Fixing a TCO coated glass substrate, "*path a*" takes place. Selecting a Mo coated substrate, "*path b* " is defined. Each path is constituted by six steps (in which five are different for type of substrate chosen and the last is in common):

1. Coating – a thin layer of photoresist is spin-coated on the chosen substrate;
2. UV irradiation – through a mechanical mask, the photoresist is exposed to UV light in order to create a pattern;
3. Developing – the photoresist's areas invested by UV light are dissolved through a proper developer solution;
4. Etching – the sample is immersed in an etching solution in order to remove the substrate in correspondence to photoresist developed zones;
5. Sputtering – the opposite material (i.e., Mo for *path a* and TCO for *path b*) is sputtered on the sample;
6. Lift off (common step) – the remaining photoresist is removed through a hot acetone bath.

Simplistically, the process is equal, but complementary in terms of photolithography: positive and negative patterns for TCO and Mo, respectively.

In this study, substrates can be both commercial and prepared via sputtering deposition in the lab. Substrates were carefully cleaned through 5 minutes sonication baths in different solvents (distilled water, acetone, ethanol, and isopropanol). They were then dried with nitrogen (5N purity). A spin coater was used in a cleanroom to make steps *1a* and *1b*. The samples were vacuum-glued through a simple rotary pump to the spin-coater sample holder, and a preliminary spin process (10 s, 1000 RPM and 193 m/s^2) was done to fix the sample. After that, a second spin process was carried out to test the deposition conditions (30 s, 4200 RPM, 193 m/s^2). In case of success, a thick layer of positive photoresist (S1813 G2 SP15) was deposited via drop-casting to cover the entire sample surface, and the final spin process was performed. This leads to the formation of a micrometric thin layer (3 μm) of positive photoresist. All prepared samples were annealed in oven for 30 minutes at 90°C, then cooled down in air and mounted on a vacuum mask aligner. A selected poly-acetate mask (positive and negative for TCO and Mo, respectively) was put in contact with the photoresist layer, then fixed with a proper adhesion holder. The masked samples were exposed to UV-C radiation (200 nm) for 60 seconds (steps *2a* and *2b*). The exposed photoresist is involved in a cross-link reaction creating a material very sensitive to ammonia solutions. The cross-linked photoresist removal, (steps *3a* and *3b*), consisted in the samples immersion into a tetramethylammonium hydroxide containing solution (MF-321 Developer) at 20°C for 60 s in order to remove all the irradiated photoresist. Subsequently, a chemical etching step (*4a* and *4b*) was necessary to selectively remove the excess of TCOs or Mo from substrates. For example, to etch ITO a concentrated HI 57% solution was employed. At the same time, to etch Mo, a strong oxidant agent like H_2O_2 30% v/v was necessary. Finally, a magnetron sputtering deposition of conductive material (TCOs or Mo, RF-MS or DC-MS, respectively) completed the windows or the grid of the embedded back contact (steps *5a* and *5b*). Last but not least, the lift-off step (*6*), was identical for both paths. It consists in the positive photoresist removal through a sonication bath in boiling acetone (56°C).

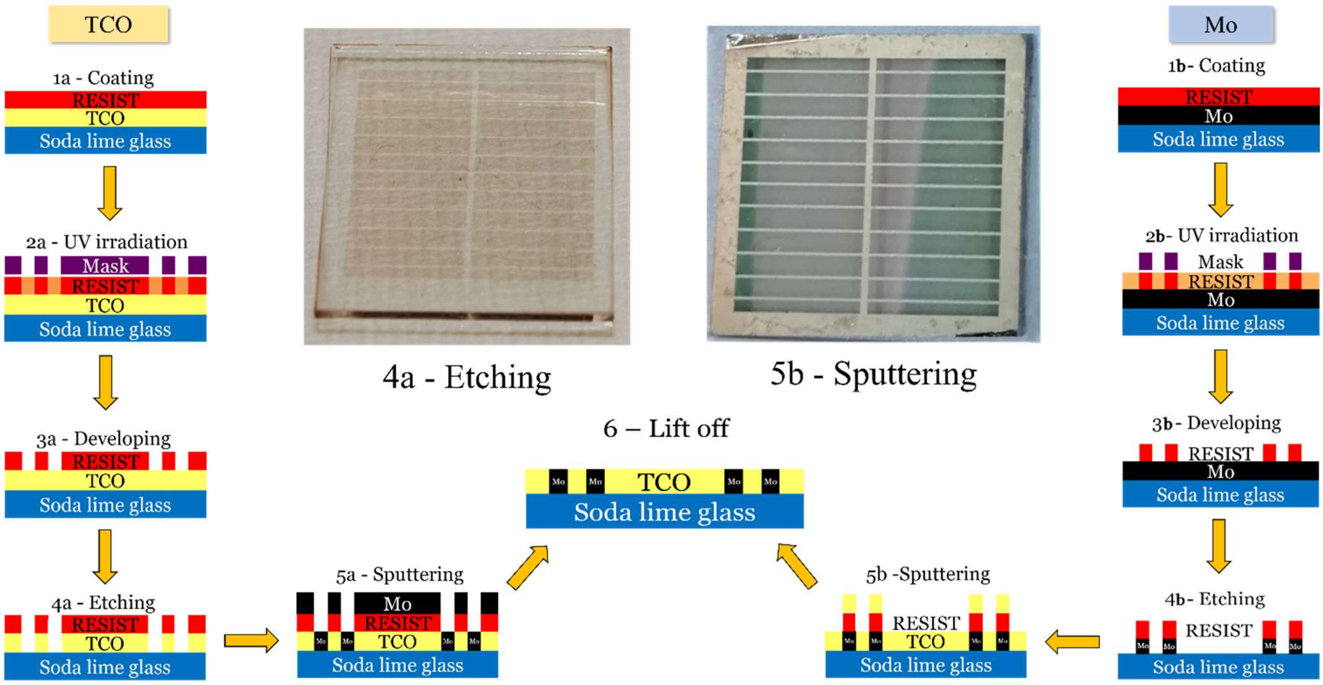

Figure 3.3: Schematic flowchart of the process developed to obtain Mo:TCO embedded grids. It is possible to notice the similarities between the two paths, the positive one, named "a", uses TCO's coated glass as starting material, and the negative one (i.e., "b") uses Mo coated glass. Furthermore, two experimental images are reported in the centre.

It is now necessary to report some fundamental critical aspects affecting particularly steps *4*, *5* and *6*.

Step 4 – Etching

Chemical (or wet) etching is one of the essential techniques for material removal in semiconductors microfabrication.[105] In this study, a high selectivity is required (i.e., the etchant solution must attack only a precise material, like Mo or ITO). Furthermore, the wet etching could be both anisotropic or isotropic if the result presents vertical or rounded sidewalls, respectively [*Figure 3.4 (a-b)*]. In this study, due to the nature of the materials, it was impossible to have an anisotropic etching, so it was tried to slow down the isotropic one as much as possible to obtain as least rounded sidewalls as possible. Finally, the etching rate (E), reported in Eq. 3.2, which is the ratio between the depth of cut required (d) and time (t), is a very important parameter that was extensively used to select etchants.

$$E = \frac{d}{t} \qquad \text{(Eq. 3.2)}$$

Chemical etching was very critical for several aspects. Molybdenum was easily attacked through H_2O_2, when it was immersed in a 30% v/v solution for 5 minutes (E = 1.7 nm s^{-1}), then rinsed in distilled water and dried with a nitrogen flux. Perfect results were obtained by step 4b; due to the slowness of the reaction: in this case the sidewalls roundness was properly limited. Our chosen TCOs were, as specified above, ITO and FTO. ITO was etched via immersion in a concentrated iodide acid (HI 57% v/v) solution for 5 minutes at 80°C (E = 1.7 nm s^{-1}, as Mo). Each sample was rinsed 6 times in abundant distilled water to completely remove this very corrosive solution. Photoresist is quite sensible to corrosive or oxidating agents; for this reason, all the intermediate concentrations were carefully investigated before directly using concentrated agents. Prolonged exposure to these etchants was detrimental; for this reason, it was preferable to increase more the solutions concentration, reducing at the same time the exposure. The above statement was not correct in the case of FTO. This material was treated with a robust etching method due its optimal chemical resistance to such strong solution.[106] Step's *3a* developing products were inserted in a proper sample holder, specifically designed for this use. High purity zinc powder was sprinkled on the surface as uniformly as possible. After that, a few drops of a HCl 1M solution were added to start the reaction, reported as Eq. (3.3). The zinc oxidation under acidic conditions leads to the formation of molecular hydrogen and the quick reduction of FTO to Sn in 40 s (E = 12.5 nm s^{-1}). All samples were afterwards washed carefully with distilled water and dried with a nitrogen flow.

$$3\,Zn^0 + 6\,HCl + \;SnO_2 \xrightarrow{40\,s} 3\,ZnCl_2 + \;H_2 \uparrow + Sn^0 + 2\,H_2O \qquad \text{(Eq. 3.3)}$$

Although the high performances of the above reaction, some collateral effects, occurred during the test phase, prejudiced the cell stability:

- The reaction corroded not only FTO but all layers; thus, several photoresist detachments and holes were created.
- The solid nano-powdered tin product remained on the glass surface, and it was very difficult to be removed. For this reason, the samples were often coloured pale grey [Figure 3.4 (d)].
- Zinc manually distributed over the sample surface was not completely homogeneous; thus, the reaction was more effective in certain zones than others, depending on the zinc powder distribution.
- The last and most critical collateral effect was, as specified above, the bad yield of the isotropic etching. Such difference in etch rate (12.5 nm/s for FTO and 1.7 nm/s for Mo and ITO) was detrimental to Mo:FTO embedded grids production. Tremendous and uncontrollable amount of powdered zinc determined easy isotropic erosion. It was thus easy to experience cutting expanding even below the photoresist with the formation of the so-called "canopies" [*Figure 3.4 (b-e)*].

These effects are all detrimental for the subsequent steps, as reported below.

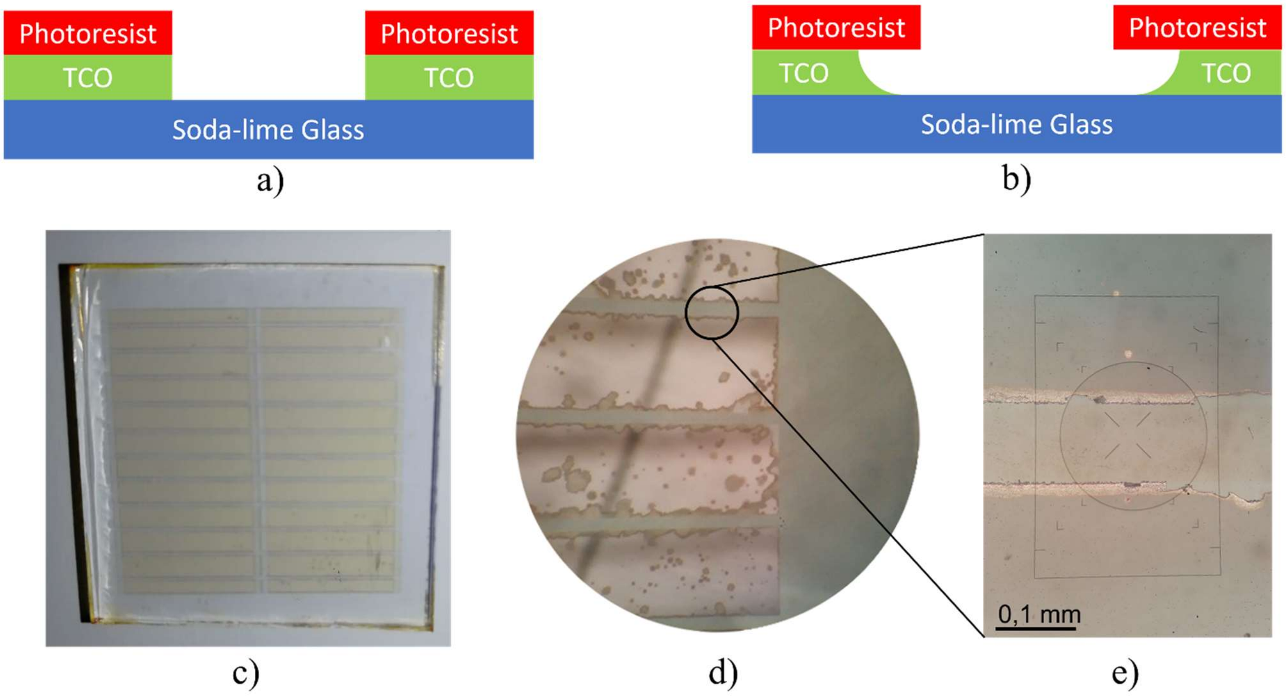

Figure 3.4: Schematic representation of an anisotropic (a) and isotropic (b) chemical etching. (c) FTO rectangles after the 4a etching process. (d) 30x-magnification of sample highlights photoresist disruption and pale grey Sn particulate. (e) Particular photoresist "canopies" as an effect of the strong isotropic chemical etching.

Despite all issues listed above, some working devices have been produced. In *Figure 3.5* are reported all characteristics of the best solar device based on Mo:FTO embedded grids. The active area is improved up to five times (0.48 cm^2) if compared with those reported in *Figure 3.2*. As previously presented, V_{oc} and R_s are similar, whereas R_{sh} is improved. The main reason of such result may be addressed to the insertion of a metal grid in the back contact without modify the deposition processes of other layers. The better conductibility and hole extraction of Mo provide the improvement of R_{sh}. Unfortunately, adhesion and etching criticalities made other parameters (i.e., J_{sc}, FF and PCE) worse as well as the R_s that, albeit in minimum part, it was slightly higher than the sample reported in *Figure 3.2*.

(a)

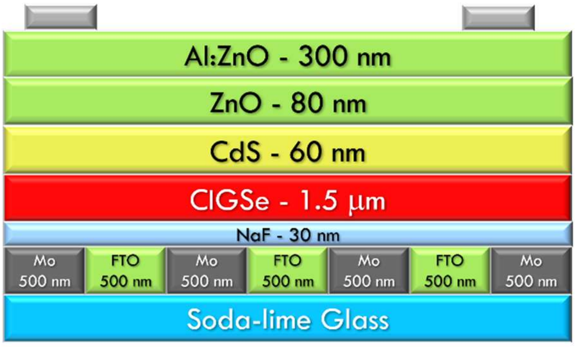

(b)

	FRONT	**BACK**
Area (cm²)	0,48	0,48
V_{oc} (mV)	648,2	514,5
J_{sc} (mA/cm²)	19,9	4,1
FF (%)	47,0	41,4
PCE (%)	6,2	0,89
R_s (Ω • cm²)	2,9	
R_{sh} (Ω • cm²)	5347,9	

Figure 3.5: (a) Schematic representation of the Mo:FTO embedded grid-based BFSC device architecture (glass/Mo:FTO/NaF/CIGSe/CdS/UZO/AZO). (b) Table with cell parameters, notice the improved active area of measurement.

Step 5 – Sputtering

To obtain good adhesion of sputtered materials for engineered substrates, the requirement of a perfectly cleaned and smooth surface is as mandatory as highly challenging to be easily granted. For this reason, profile checks on each sample were carried out, pointing out the success or unsuccess of each attempt. In order to create surfaces that did not present any interruption between the TCO and the selected metal, it was of fundamental importance to have a smooth surface without cracks, depressions, or spikes. Thus, to have a good interface for the deposition of the absorber layer and to favour a correct passage of the carriers, the thickness continuity between the two materials has to be granted and so the smoothness and flatness of the entire mixed layer. Hence, accurate control over the deposition rates was necessary to avoid the creation of an irregular back contact interface. Beside this, if the phenomenon of photoresist "canopies" was present in a sample, this could prejudice the deposition by sputtering. It was very likely to obtain the formation of deep grooves, called "fingers", resulting from the shadow of the photoresist formations. As reported in *Figure 3.6*, the formation could be intense, sometimes also involving the glass support (at about approximately 500 nm of depth), thus creating strong discontinuities. For all the reasons listed above, and due to scarce repeatability and a high degree of failure of this process, the manufacturing of Mo:FTO-based embedded grids was interrupted.

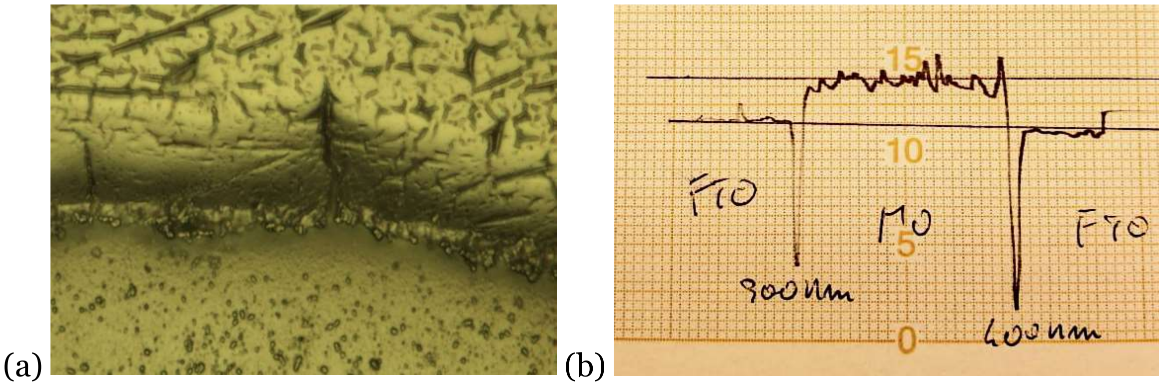

Figure 3.6: (a) 30x-magnification of photoresist edge. Notice the dot irregularities both on glass and in the point of contact with FTO. (b) Step-profilometer measure (1 mm on sheet is equal to 20 nm). "Fingers" created by photoresist "canopies" and the poor control over the growth rate of Mo are apparent.

Step 6 – Lift-off

The temperature as well as corrosive chemical treatments are the leading cause of photoresist deterioration at step *6*. For Mo depositions (step *5a*; DC-MS), high temperatures do not represent a relevant problem, since the deposition is conducted at 50°C. For ITO, contrarily, it is impossible to deposit below 350°C of operating temperature during RF-MS process. Noteworthy, at such temperatures, the photoresist carbonized, assuming the characteristics of a ceramic and losing the referred characteristics by the producer. This prevents photoresist lift-off process to result in a genuine Mo:ITO mixed contact. Thus, ITO was grown at the lower temperature possible, but the product was highly fragile and entirely unsuitable for subsequent vacuum and chemical treatments. Tests were conducted both modifying ITO growth temperature and testing different methods of lift-off. The photoresist transition range was found to be 225-250°C, and ITO started to have an average adhesion over 200°C (that increased to good at 250°C and excellent over 300°C). The lift-off after a 250°C heat was difficult due to the almost complete carbonization of the photoresist. Neither boiling acetone was not enough to remove the residual carbonized photoresist.

For this reason, it was attempted a prolonged immersion in the same solvent but in a reflux regime for 12 hours and a strong sonication in hot acetone. Both attempts led to not complete photoresist removal and the partial deterioration of ITO's windows. Furthermore, a 24-hour immersion in acetone was tried at RT. The prolonged treatment allowed the carbonized photoresist to be wholly moistened by the solvent. Finally, through a delicate manual polishing with a sterile cotton swab and a few drops of solvent, it was possible to successfully remove the photoresist altogether without scratch the substrate surface, as reported in *Figure 3.7*.

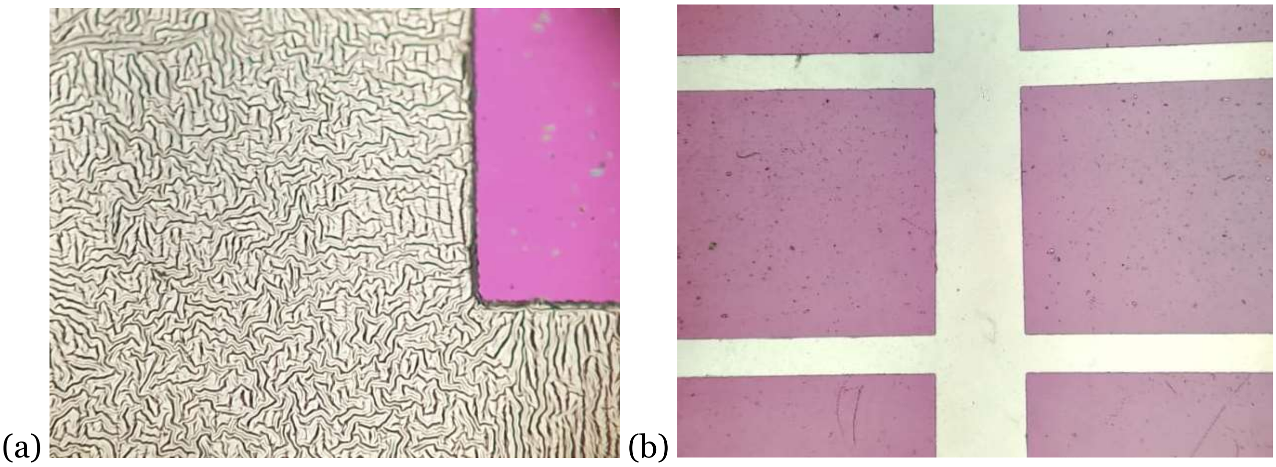

Figure 3.7: (a) 40x magnification of a sample at step 5b under polarized light after ITO's deposition at 250°C. The particular is a Mo grid cross, in which it is possible to notice the corrugated appearance of the carbonized photoresist under a thin layer of TCO. The pink aspect of ITO is related to thickness (500 nm). (b) 5x magnification of the same sample after the lift-off (step 6). In white is the free Mo grid, and in pink is the bare ITO.

3.3) Mo:ITO EMBEDDED GRIDS CHARACTERIZATION

Ohmic contacts and large areas were the principal focus of this study. However, in a broader perspective, new photovoltaic cells based on Mo:ITO embedded grids should be developed.

For the first instance, processability had a significant influence on the goodness of devices. Several samples were prepared by depositing ITO at 350°C. Next, ITO was etched, and Mo was deposited via DC-MS at 50°C, thus following *path a*. After the lift-off, excellent properties in terms of resistivity and active areas were found. The only critical point at this level was the flatness of the mixed layer which needs accuracy at the nanometric scale. In *Table 3.1* resistivity test results are reported for such samples and compared to Mo:FTO embedded grids (*Figure 3.5*) in dark conditions. As it can be appreciated results are excellent: larger area but decreased R_s and improved R_{sh}.

Table 3.1. Dark characterization for a "path a" sample in comparison to Mo:FTO case of study.

	Mo:ITO	**Mo:FTO**	**Variation**
Active area (cm^2)	2.0	0.48	+ 317 %
R_s (Ω*cm^2)	1.8	2.9	-38%
R_{sh} (Ω*cm^2)	271130.8	5347.9	+467‰
Ideality factor	1.7	N.A.	/

Mo:ITO embedded grid back contacts reported above can be compared directly to an ideal diode. This result is totally in contrast with Mo:FTO and the reasons could be found in those issues explained in the previous paragraph (i.e., FTO etching and photoresist "canopies").

Very good results were instead obtained on samples prepared via *path b*. In this case, it was noticed a rise of resistivity value after the lift-off step. A little study on annealing pre- or post-photoresist removal was conducted (*Table 3.2*). Commercial Mo was etched, and ITO was deposited at 200°C, following *path b*. All samples were annealed at 150°C in air for different periods before and after the lift-off. In order to avoid fake measurements caused by the formation of molybdenum oxides, a rinse in distilled water was done on each sample after annealing treatment, being known in literature that such oxides are perfectly soluble in water.

Table 3.2: Effects of air annealing before and after the lift-off step on $\rho_\square$ (sample 1 and sample 2, respectively).

	Time (min)	**Average $\rho_\square$ (Ω*cm^2)**
Sample 1 (annealed BEFORE lift-off)	0	13.3
	5	12.6
	10	12.3
	15	13.3
	20	12

	Time (min)	**Average $\rho_\square$ (Ω*cm^2)**
Sample 2 (annealed AFTER lift-off)	0	430.0
	5	357.6
	10	359.6
	15	241.6
	20	267.3

As shown above, an annealing treatment after the lift-off step was detrimental to electrical properties of the device. For sample 2, it is possible to notice a significant reduction of R_s up to 15 minutes of treatment. This was a direct effect of ITO cracks forming on the surface. As a remind, ITO was grown at 200°C thus it comes out pretty fragile. Sample 1 was used to deposit a whole photovoltaic device: its geometrical characteristics and electrical behaviour are reported in *Figure 3.8 (b)*.


(a)

(b)

	Mo:ITO	**Mo:FTO**	**Comparison**
Area (cm²)	0,2	0,48	-58,3
V_{oc} (mV)	525,9	648,2	-18,9
J_{sc} (mA/cm²)	37,2	19,9	+86,9
FF (%)	41,4	47,0	-11,9
PCE (%)	8,0	6,2	+29
R_s (Ω • cm²)	2,2	2,9	-24,1
R_{sh} (Ω • cm²)	46,9	5347,9	-99,1

Figure 3.8: (a) Picture of sample's 1 back contact before CIGSe deposition. (b) Front electrical measurements on a Mo:ITO cell obtained via path b with an annealing treatment before lift-off (sample 1) and comparison with Mo:FTO.

Mo:ITO-based PV device obtained a remarkable improvement of J_{sc} and an excellent 29%-increase of efficiency compared with Mo:FTO-based. Despite this, FF (%) and R_{sh} (Ω*cm²) are not comparable. The reasons of these bad values be traced back in the employed vacuum and chemical processes.

CHAPTER 4

ANTIMONY SELENIDE (Sb_2Se_3) FILM ORIENTATIONS

4.1) SPACE GROUP SELECTION AND EFFECT ON PROPERTIES

As reported in paragraph 2.5.1, ASe is a promising type-p PV material due to its peculiar anisotropic characteristics. This material merged the necessity to avoid toxic compounds (e.g., CdTe) and to use cheap and earth-abundant elements (i.e., avoiding for example the use of indium). The structure is characterised by infinite layer of covalent ribbons composed by $(Sb_4Se_6)_n$ units along the (001) direction, the shorter lattice direction.[107] Each ribbon is stacked to others thanks to weak VdW interactions. As reported in *Figure 4.1* and discussed above, the best carrier extraction is obtained if ribbons are oriented normal to the substrate, thus precluding a conduction mechanism driven by hopping. Hence it is of fundamental importance to obtain the correct orientation during a deposition. Moreover, it is important to define the best reference space group to better interpret its structure and use this information for proper choose the underlying substrate for material to be grown on.

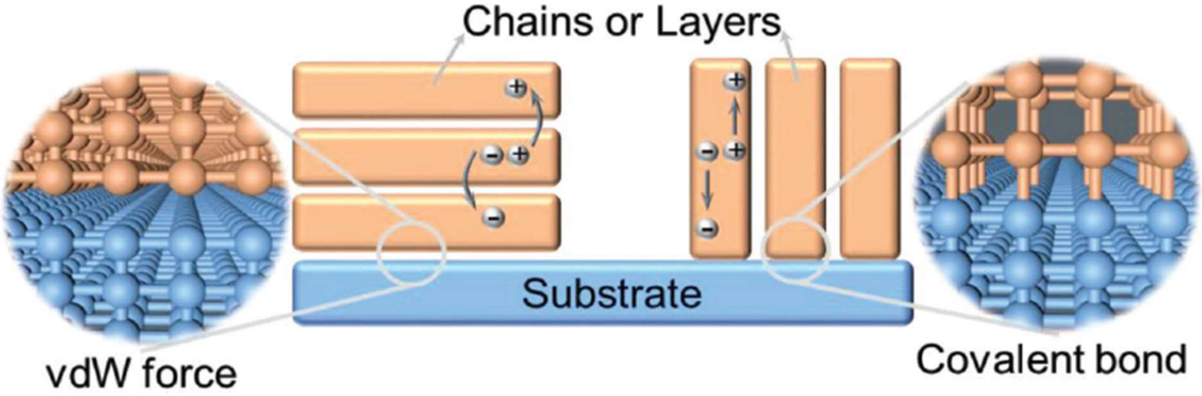

Figure 4.1: Schematic charge conduction in ASe ribbons oriented in different directions. The "+" and "-" are photogenerated holes and electrons, respectively.[108]

For what concerns structural evaluation on the material, ASe crystallizes with an orthorhombic symmetry, mmm or D_{2h}^{16} point group (Hermann-Mauguin or Shoenflies notation, respectively). The conventional space group is Pnma (Nr. #62). The glide planes (i.e., a, b, c, or n) can be applied to a simple permutation matrix generating several non-conventional #62 space groups: Pbnm, Pnmb, Pcmn, Pmcn, and Pnam. In recent years, some papers reported both conventional and non-conventional space groups without any distinction to describe ASe's structure, thus creating misleading interpretations.[109, 110] No differences can be observed between the various PXRD patterns of different space groups, but the indexing is radically different. For example, in a paper by *Zhou et al.*[111], the ASe is correctly reported according to the space group Pbnm, but some illustrations refer to the Pnma conventional group instead. In order to further clarify the difference between space groups, *Figure 4.2 (a-b)* is reported. Standing this observation, in this work, Pbnm space group was uniquely adopted to define the lattice parameters as a=11.62 Å, b=11.77 Å, c=3.96 Å (JCPDS Card No. 15-0861).

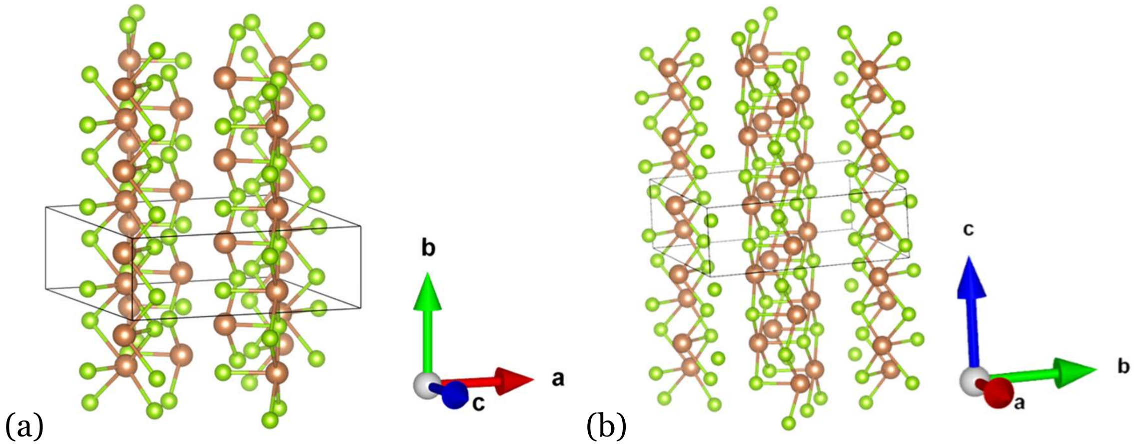

Figure 4.2: (a) Schematic representation of Pnma space group for ASe. (b) Schematic representation of non-conventional Pbnm space group for ASe. Sb and Se are represented by brown and green dots, respectively.

Indexed reference powder pattern (JCPDS Card No. 15-0861) is reported in *Figure 4.3*. It is essential to notice that the Miller's indexs permutation are (bca) in Pbnm non-conventional space group, instead of the classical (abc), obtained from the original Pnma. Standing this, the orientations for which the ribbons are horizontal to the plane present (hk0)-type indexes. Viceversa, those oriented vertically have indexes of (00l)-type. The intermediate ones, called slanted, are more or less important depending on how much the angle between substrate and ribbon is close to the (00l)-type.

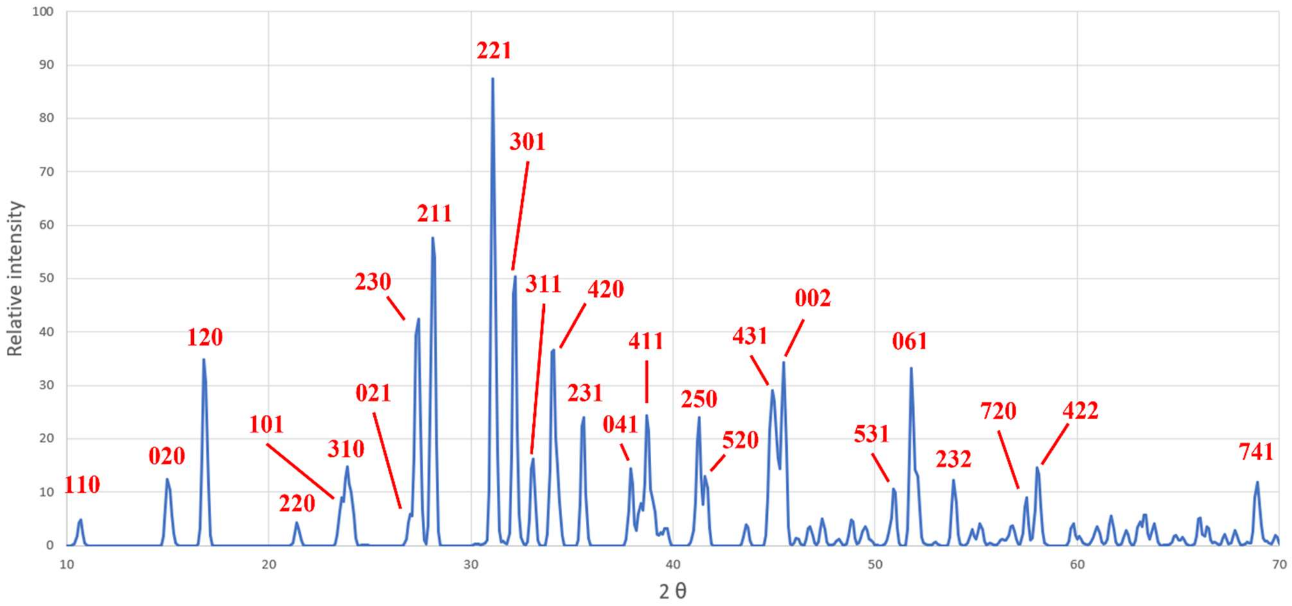

Figure 4.3: PXRD reference pattern for JCPDS Card No. 15-0861, indexed with main orientations in Pbnm non-conventional permutation.

Chosen the reference spatial group (i.e., Pbnm), the goal of this work was to grow polycrystalline ASe films with the correct crystallographic orientation to obtain ribbons normal to the substrate, in order to favour the maximum extraction of carriers. The relative orientation of ribbons strongly influences all PV properties. Many examples are reported in literature, but a polycrystalline film containing most of the (hk0)-type orientations will lead to low performances due to hopping carriers' as majority transport mechanism.[112, 113] Contrariwise, the actual PCE's world record is given by a layer mainly composed by (221) ribbons grown on $MoSe_2$ substrate.[114] The most relevant crystallographic reflections (reported by *Pattini et al.*[58] in *Figure 4.4*) are represented by ribbons grown on a hypothetical substrate (blue line). The ribbon vertical direction, [001], is represented by the red vector, helping to visualise each orientation with respect to the one desired. Moreover, the relative angles (001) and the substrate plane are given in *Table 4.1*.

Table 4.1. Angle values between ribbon crystallographic orientations a hypothetical substrate.

(hkl)	Angle (°)	(hkl)	Angle (°)	(hkl)	Angle (°)	(hkl)	Angle (°)
(002)	90	(221)	46.2	**(041)**	36.6	(061)	26.4
(211)	52.7	(301)	44.3	**(411)**	35.8	(hk0)	0

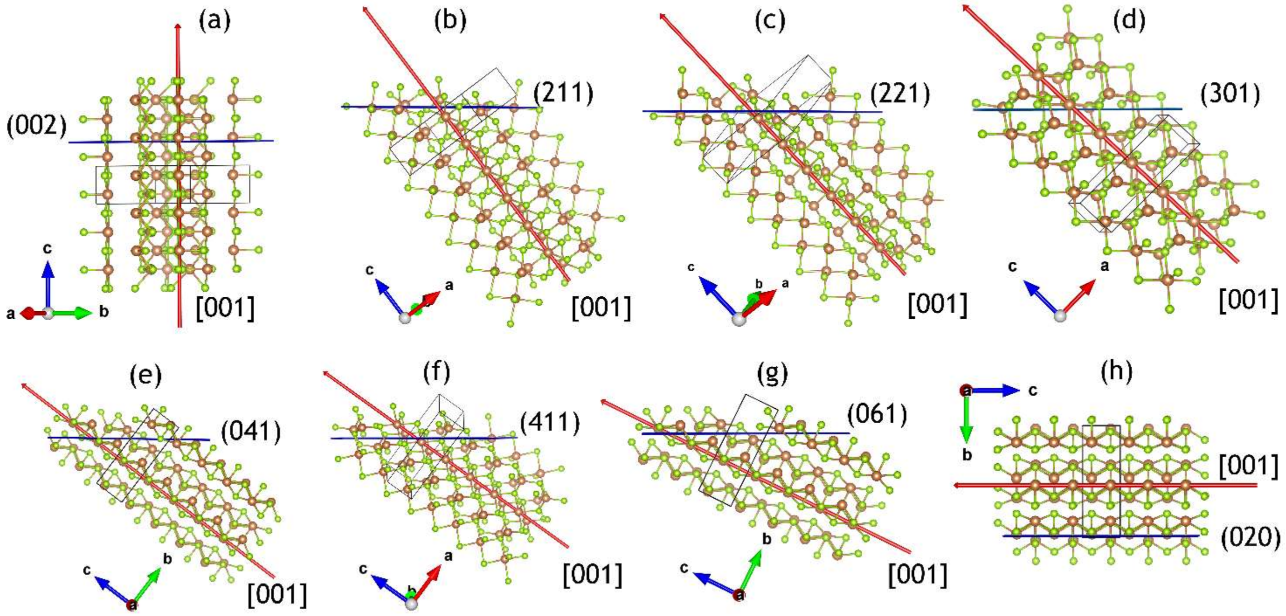

Figure 4.4: Graphic representation of the main crystallographic orientations of ASe concerning a hypothetical surface of growth (blue line). The red vector [001] is used to visualize the ribbons orientation with respect to the surface.

4.2) ASe-SUBSTRATE MISMATCHES: A SYSTEMATIC STUDY

It was specified above that substrates can strongly influence ASe thin-films orientation. In addition, a process of annealing could help in the self-organising grains after or during the deposition. The texture coefficient (TC) is a valuable parameter for analysing a polycrystalline film's preferential orientations. It is defined, as follows, in *Eq. (4.1)*, where I and I_0 are relative, respectively, to PXRD intensities of experimental and tabulated patterns, and n is the number of reflections considered.

$$TC\ (hkl) = \frac{\frac{I(hkl)}{I_0(hkl)}}{\sum_n \frac{I(h'k'l')}{I_0(h'k'l')}} \cdot 100\% \qquad \text{(Eq. 4.1)}$$

A careful study was carried out on the preferential orientations of ASe grown on different substrates and annealed at different temperatures. *Figure 4.5* shows that the use of Mo leads to low-efficiency devices linked to a film consisting primarily of horizontal ribbons.[58] At the same time, the use of different substrates, as FTO, leads to an increase in performance thanks to the massive presence of slated ribbons and lowered percentages of (hk0) reflections.

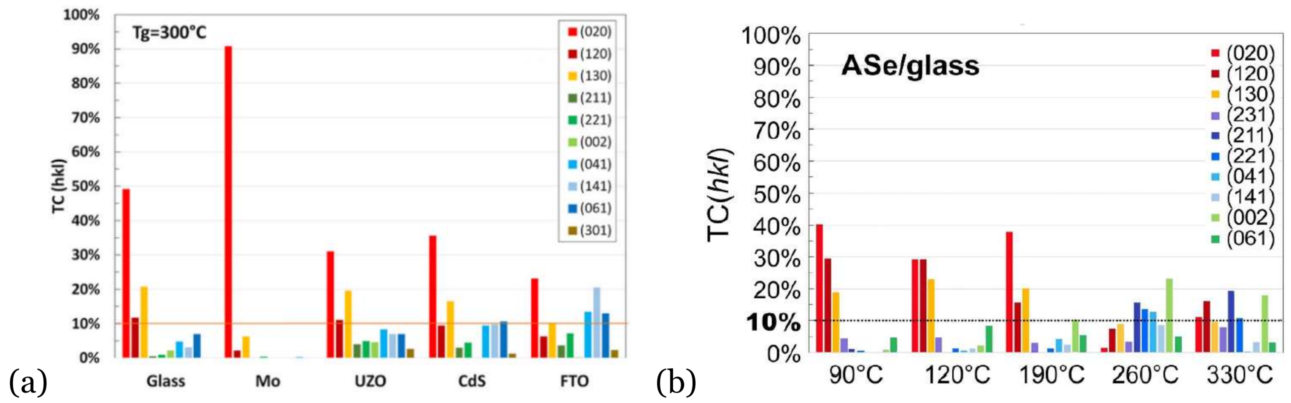

Figure 4.5: (a) ASe TC (hkl) values for different substrates.[58] *(b) Annealing temperature influence on ASe TC (hkl).*[60]

In order to further increase the orientation of (00l), (211) and (221)-types as much as possible, a detailed study on crystal lattices of interest was necessary matching ASe ribbon surfaces and some possible substrates, treated as seed layers. Therefore, the empirical parameter of crystal lattice misfit (ε) was used, defined in *Eq. (4.2)*.

$$\varepsilon = \frac{d_{film} - d_{substrate}}{d_{substrate}} = \frac{d_{ASe}(hkl) - d_{substrate}(hkl)}{d_{\ substrate}(hk\ )} \qquad \text{(Eq. 4.2)}$$

This parameter is adimensional and refers only to the lattice distances (d) ratio of two crystalline lattices. Misfits' empirical values qualitatively provide information on growth compatibility, stress-strain compressions, and dislocation formation between different crystal lattices. If ε = 0, the reticular distances of two materials are the same. With ε>0, $d_{ASe}>d_{substrate}$ and a compressive force will act on the ASe surface at the moment of the deposition. Contrarywise this, if ε<0, $d_{ASe}<d_{substrate}$ and a tensile force will be involved. Moreover, if the ε value is similar to 0, these forces are not very intense; thus, they will not create strong distortions to the unit cell. On the other hand, if the misfit value grows, it is

possible to estimate the presence of such forces (ε ± 1) that can generate surface stretches like dislocations (ε ± 2), even plastic deformations (ε ± 3).

It is well reported above that ribbons should grow vertical in the Pbnm space group, thus on [001] plane. If they are parallel to the substrate, they lie on planes [100] or [010]. VESTA software and ICSD database were extensively used to determine all the possible reticular distances in ASe and substrates preferential grow planes. In *Table 4.2* are reported all the lattice distances calculated in the ASe orientation of interest.

Table 4.2. Lattice distances were calculated via VESTA software for interest orientations (JCPDS Card No. 15-0861).

(hkl)	**d (Å)**
(hk0)	3.96
(211)	12.42
(221)	14.13
(041), (411)	11.77
(002), (061)	11.62

A mathematical model was created to provide all the possible combinations between such ASe's values and those of the seed layers. In this way, the task was to find the best value of misfit and know, theoretically and a priori, which specific material orientation could maximise the vertical orientations of ASe (e.g., 002). Over 25 types of substrates were tested; the group included several metals (Cu, Mo, Al, Au,..), TCOs (FTO, UZO, ITO, Cu_2O,...), and other materials like CdS, $CuSbSe_2$ or CIGSe. The most relevant results are presented in *Table 4.3*. It is possible to notice from the misfit values with Mo that a vertical or oblique orientation of the ribbons is very unlikely, as reported in *Figure 4.6*.

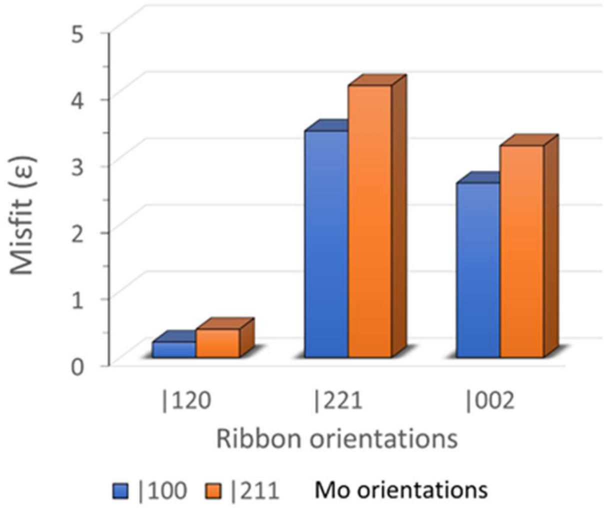

Figure 4.6: Misfit values for three ASe ribbons compared to main reticular distances of Mo.

A material with a larger lattice parameter is, thus, required as substrate for ASe. For example, Pb could be better, but misfit values indicate that it is not the correct seed layer. All metals have misfit values comparable to those reported in literature. Among TCOs, the best is undoubtedly ITO. However, the very homogeneous results showed that an ASe film could grow with random orientations on such substrate. Finally, FTO does not seem suitable for the growth of highly oriented ASe films due to the preponderance of low values in (hk0). Due to the failure of almost all types of substrates available, it was thought to prepare heterogeneous or engineered substrates.

Table 4.3. ASe misfit values for Mo (ICSD 643957), Pb (ICSD 96501), ITO (ICSD 50849), FTO (ICSD 39178) and UZO (ICSD 76641).

			Sb_2Se_3		
	(hkl)		**(hk0)**	**(221)**	**(002)**
		d (Å)	3.96	14.13	11.62
Mo	**(110)**	3.21	0.24	3.41	2.62
	(211)	2.78	-0.43	4.09	3.18
Pb	**(111)**	3.50	0.13	3.04	2.32
	(100)	4.95	-0.20	1.85	1.35
	(311)	7.83	-0.49	0.81	0.49

ITO	(211)	8.77	-0.55	0.61	0.32
	(222)	7.16	-0.45	0.97	0.62
	(400)	10.13	-0.61	0.39	0.15
	(440)	12.41	-0.68	0.14	-0.06
FTO	**(110)**	3.19	0.24	3.42	2.63
	(101)	5.73	-0.31	1.47	1.03
	(200)	4.76	-0.17	1.97	1.44
UZO	**(100)**	3.25	0.22	3.35	2.58
	(002)	5.21	0.24	1.71	1.23

A paper by *J. Zhou et al.* used Boron Zinc Oxide (BZO) as the seed layer, obtaining a selective growth of ASe on (002) reflection.[115] Based on misfit data obtained by UZO, similarly to those of other TCOs, it was thought to engineer a substrate in order to create vertical nanostructures (e.g., nanopillars or nanowires) that would help ASe to grow parallel to them during an RF-MS deposition. Since the preferential orientations on UZO are (hk0), if the substrate is nano-verticalized, this would help ASe grow with ribbons parallel to these nanostructures. *Figure 4.7 (a)* graphically represents the idea of UZO nanostructures and the hypothetical ASe vertical growth on them. Some experimental tests are in progress to demonstrate the veracity of the system. The preliminary results are shown in *Figure 4.7 (b),* and they are very promising. (hk0)-type reflections resulted low in intensity, and the predominant reflections were typical of slanted ribbon reflections (hk1). The concomitant work of *J. Mendes* supported this study finding similar conclusions using Vapour Transport Deposition (VTD).[116]

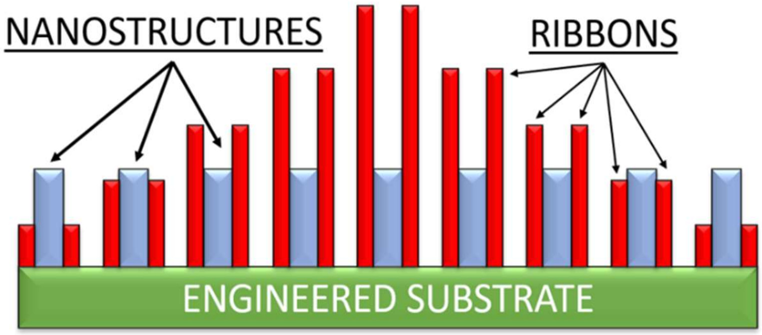

(a)

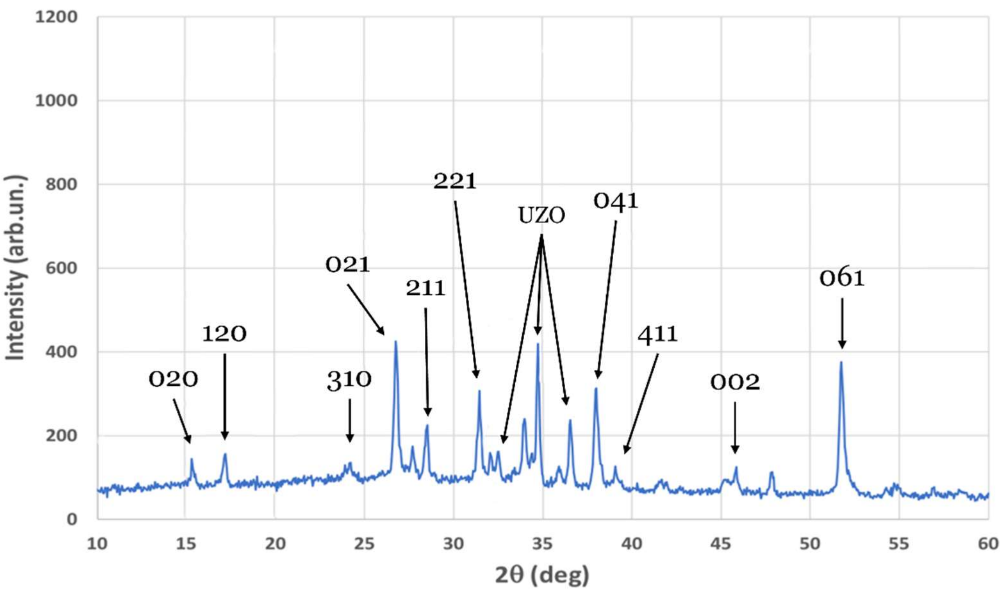

(b)

Figure 4.7: (a) Schematic representation of nanostructure engineered substrate. (b) PXRD pattern of an ASe sample grown on UZO nanowires engineered substrate.

Since this entirely theoretical study was based on the orientation of the first seed layer formed during the deposition of ASe, one can argue if ASe could work as the seed layer itself, thus influencing and improving TC. Through specific growths by RF-MS, it has been noted that the increase in deposition time and, therefore, in thickness, led to an enhancement in the orientations of interest.[60] A comparison, reported in *Figure 4.8*, shows that the orientations can be influenced using ASe as seed layer and a proper annealing process.

All samples reported here were grown via RF-MS on bare SLG at the pression of $5 \cdot 10^{-3}$ mbar, with a power of 30 W, at the temperature of 130°C. After deposition, each sample was annealed for 30 min at 250°C. The only variation was the deposition time: 25, 50 and 100 minutes. It was possible to notice that, in the beginning, with deposition times of 25 minutes, the film presented a majority of reflections belonging to (hk0)-type. As the deposition is prolonged over time, the (hk0)-type reflections intensities highlights a sharp decrease, and others take their place. Reflections of (hk1)-type are predominant for long deposition times (i.e., 100 minutes). In addition, a remarkable increase in (002) reflection could be noticed.

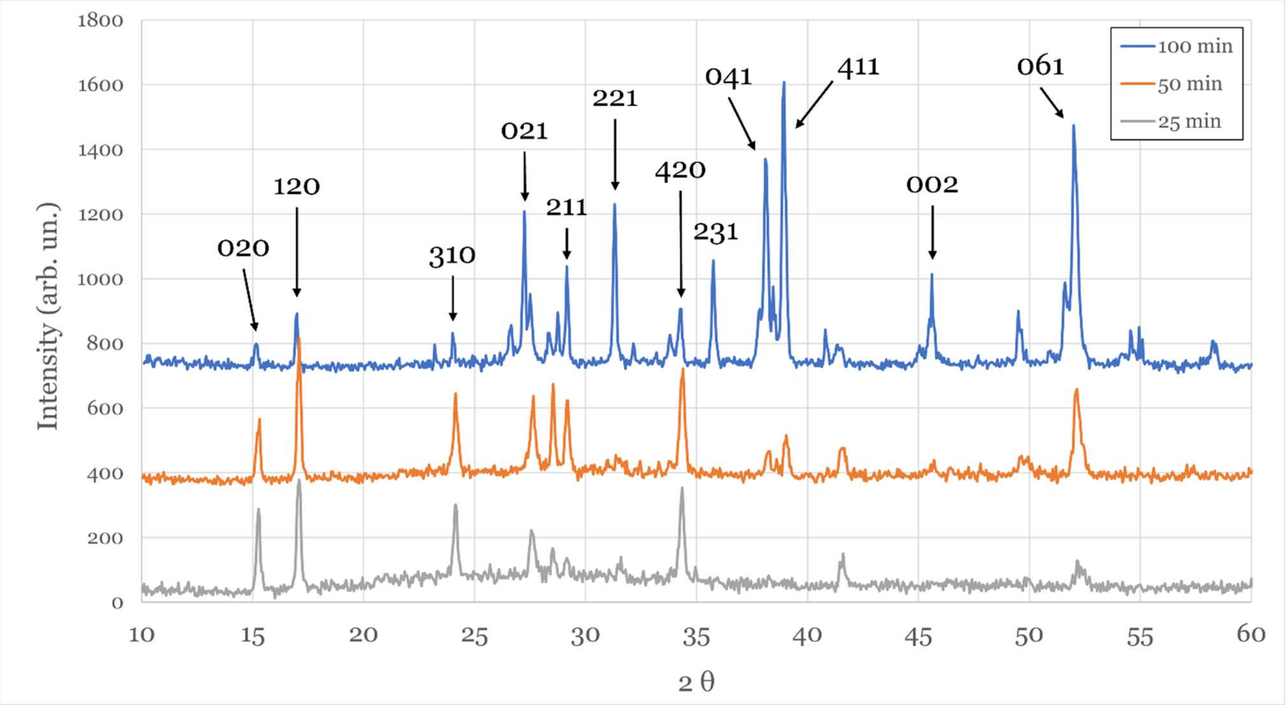

Figure 4.8: Comparison between PXRD patterns of ASe thin-films grown through RF-MS at different times.

Further studies are underway to define the importance of ASe itself as a seed layer.

CHAPTER 5

CHALCOGENIDE VARNISHES-BASED THIN-FILM SOLAR CELLS BY ULTRA-LOW-COST BALL MILLING: A DREAM CAME TRUE.

5.1) CIS BALL MILLING

Pure reagents powders of Cu_2S and In_2S_3 were purchased from Alfa Aesar (99.5% and 99.995% metal basis purity, respectively). In order to prepare pure powders of CIS ($Cu_{0.9}In_{1.1}S_2$), 286.48 mg of Cu_2S and 716.8 mg of In_2S_3 were carefully weighted through an analytical balance. Both powders were inserted in an agate (SiO_2) mortar and mixed with an agate pestle for 1 minute, obtaining a light brown powder mixture [*Figure 5.1 (a)*]. The dry grinding was chosen to favour the mechano-reaction. It is necessary to point out that the overall stoichiometry of the product was not Cu:In:S equal to 1:1:2 but 0.9:1.1:2. Cu-substoichiometry was required to our knowledge to make the final absorber work as PV element.[117] In two different closed agate jars, with a controlled atmosphere, were inserted 5 agate spheres of diameter 10 mm. The reagent mixture was divided into two portions of 500 mg each. Subsequently, each aliquot was inserted in the relative jar, and the system was closed and sealed through an appropriate screw placed on the top of the lid [*Figure 5.1 (b)*]. The original air atmosphere was purified through 4 purge cycles of pure nitrogen gas (5 N purity) up to a pressure of 2.8 bar. After the purging each jar was prepared for the reaction and filled with a different nitrogen pressure (4 bar). This passage is mandatory due to the necessity to avoid oxidations and crystallite aggregations during the MC. Both jars were inserted in a Pulverisette 7 high-energy planetary ball mill (*premium line*).

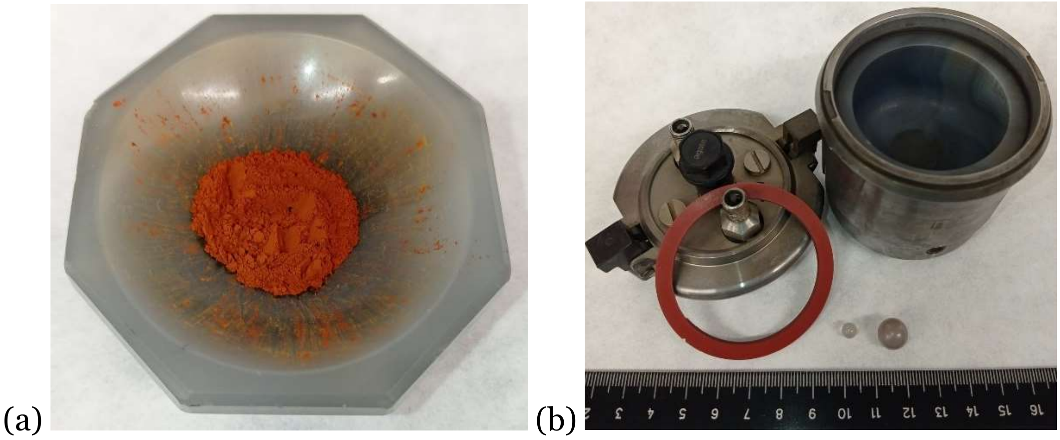

Figure 5.1: (a) The reagent's mixture, after dry manual grinding, before mechano-reaction. (b) One of the agate jars with the lid equipped for insulating and controlling the inner atmosphere, silicone o-ring and two agate spheres (⌀5 mm and ⌀10 mm, left and right, respectively).

The synthesis parameters reported in *Table 5.1* were applied for the MC. Noteworthy, the requirement of high energies (i.e., high RPM and big spheres) is necessary to obtain the correct MC reaction. The process was standardized to perform the revolution just along the primary direction.

Table 5.1: Mechano-reaction parameters for CIS preparation.

Total mass per jar (g)	0,5
Mill duration (h)	5
Repetitions (N)	1
Pause (min)	0
Reversal rotation?	No
RPM*	530
BPR**	13
Mill spheres diameter (mm)	10
Mill N spheres	5
Material	Agate (SiO_2)

* Rotation Per Minute; ** Ball to Powder Ratio

As the mechano-reaction ended, whose chemical reaction is reported in Eq. (5.1), the sealed jars were cooled down to let all powders precipitate.

$$Cu_2S + In_2S_3 \rightarrow 2\ CuInS_2 \tag{Eq. 5.1}$$

After a few minutes, the nitrogen over-pressure was removed via relief valves, and the whole jars were inserted in a glovebox. The atmosphere was purged with nitrogen, by cycling out the air with a vacuum pump and then fluxing the inert gas at least three times. Both jars were opened under a weak over-pressure of 5 N nitrogen.

CIS is entirely isostructural to, e.g., CISe.[118] Despite this, the presence of the small peak at 32°, belonging to (200) reflection, is the finger print of the presence of a sulphide-based chalcopyrite [*Figure 5.2 (a)*]. The preliminary appearance of the obtained powder confirmed or not the success of the reaction. If the colour was black, reactions occurred [*Figure 5.2 (b)*].

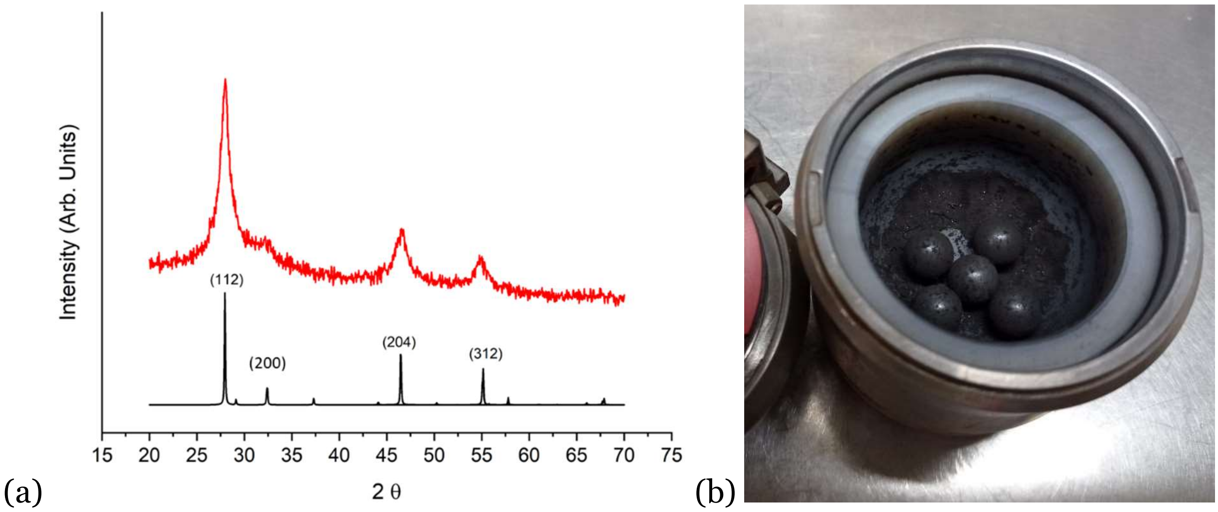

Figure 5.2: (a) CIS powder appearance after the MC reaction. (b) The PXRD pattern of CIS compared to the reference pattern of sulphide-based chalcopyrite (ICSD code 66865).

A PXRD control analysis was carried out for each jar. In *Figure 5.3* is reported a comparison between product and reagents PXRD patterns (i.e., In_2S_3 and Cu_2S).

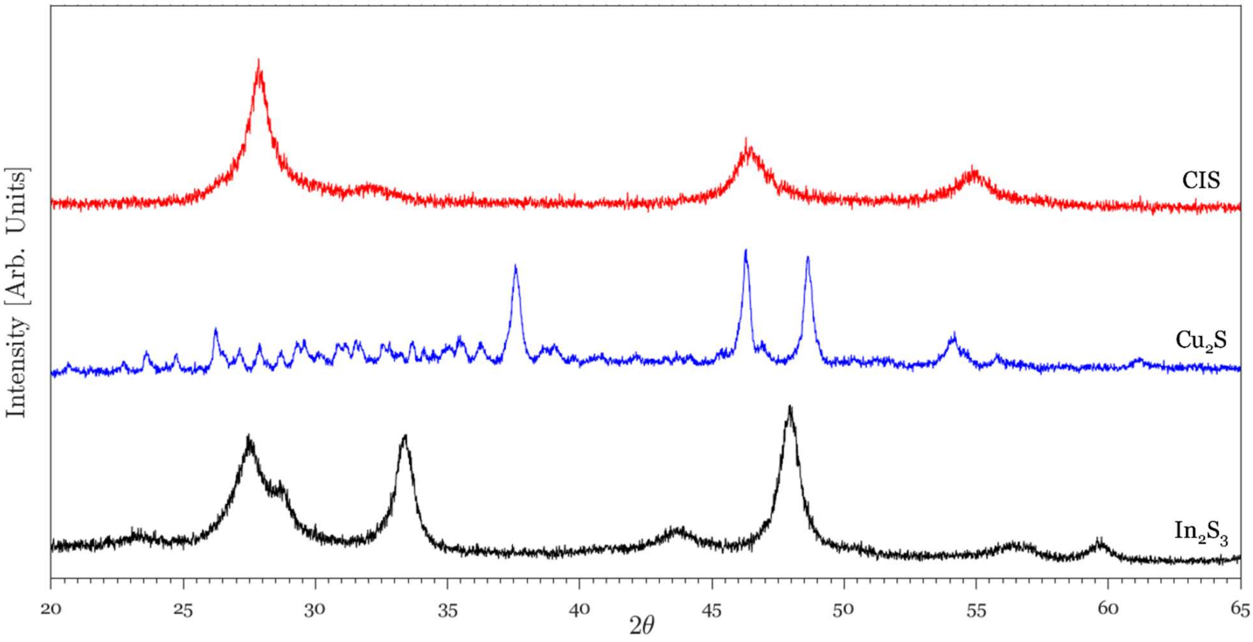

Figure 5.3: PXRD pattern comparison between pure CIS and reagents for MC reaction.

Moreover, a tiny amount of SiO_2 contaminant was detected as unavoidable due to medium mechanical deterioration of spheres and jars, and it was no longer observable through PXRD due to its amorphous or nanocrystalline characteristics. As previously reported, CIS powders obtained by mechano-synthesis presented a sub-micrometrical average size of the crystallites and the correct stoichiometric ratio (*Table 5.2* and *Figure 5.4*).

Table 5.2. EXD compositional analysis for CIS mechano-powder.

	Cu	**In**	**S**	**(Si)**
%	23,36	27,13	49,52	(1,5)

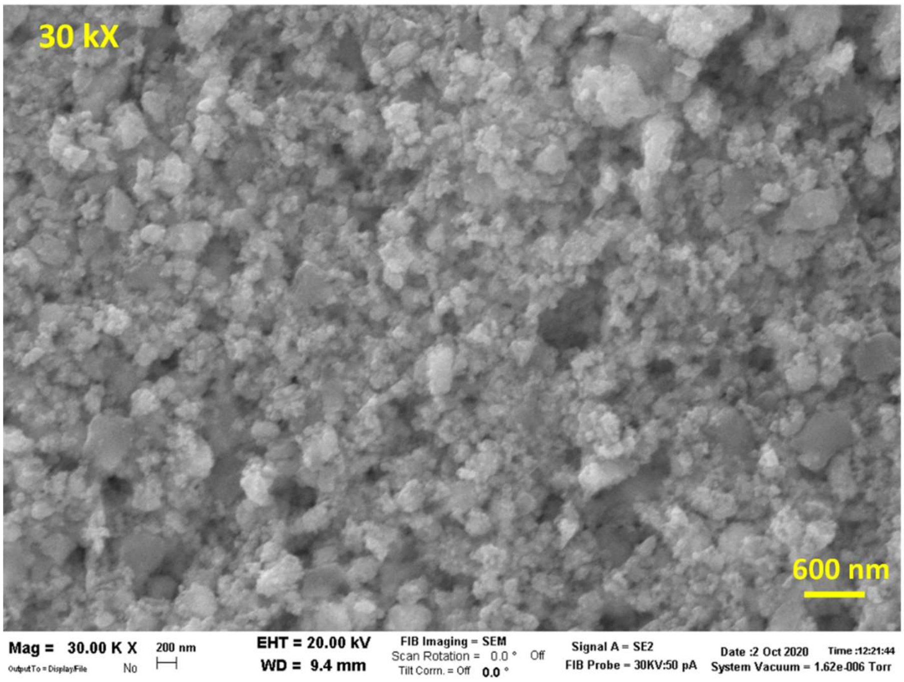

Figure 5.4: 30 kX Scanning Electron Microscopy (SEM) image of pretty homogeneous and sub-micrometrical CIS powders.

5.2) VARNISHES PREPARATION THROUGH CIS LIQUID ASSISTED REFINEMENT

After the MC, CIS powders were suspended in a proper solvent in order to create a varnish: a refining experiment must occur. i-PrOH was selected due to its high availability, low toxicity, and cost. After opening the jars into the glovebox's under nitrogen atmosphere, the agate 10 mm spheres were removed, and 10 ml of i-PrOH were added in both jars. Subsequently, 12 spheres of 5 mm diameter were added, and jars were re-sealed. Next, the internal atmosphere was purged again with nitrogen (5 N purity) at the pressure of 2.8 bar. This time, only two cycles were done to avoid solvent evaporation as much as possible. Finally, jars were filled with nitrogen at the pressure of 4 bar, as done for the mechanosynthesis passage. The refining parameters are reported in *Table 5.3*. In this case, a long milling treatment with lower energies (with respect to MC process) is necessary.

Table 5.3. Refining parameters for CIS varnish.

Mass CIS per jar (g)	0,5
Solvent	i-PrOH

Solvent volume (ml)	10
Mill duration (min)	6
Repetitions (N)	100
Total time (h)	10
Pause (min)	0
Reversal rotation?	Yes
RPM*	300
BPR**	4,5
Mill spheres diameter (mm)	5
Mill N spheres	12
Material	Agate (SiO_2)

* Rotation Per Minute; ** Ball to Powder Ratio

The standard CIS-based PV varnish has thus been obtained, as pictured in *Figure 5.5 (a)*. As, reported in *Figure 5.5 (b)*, the PXRD comparison between CIS powder and dried varnishes shows a slight enlargement of all peaks.

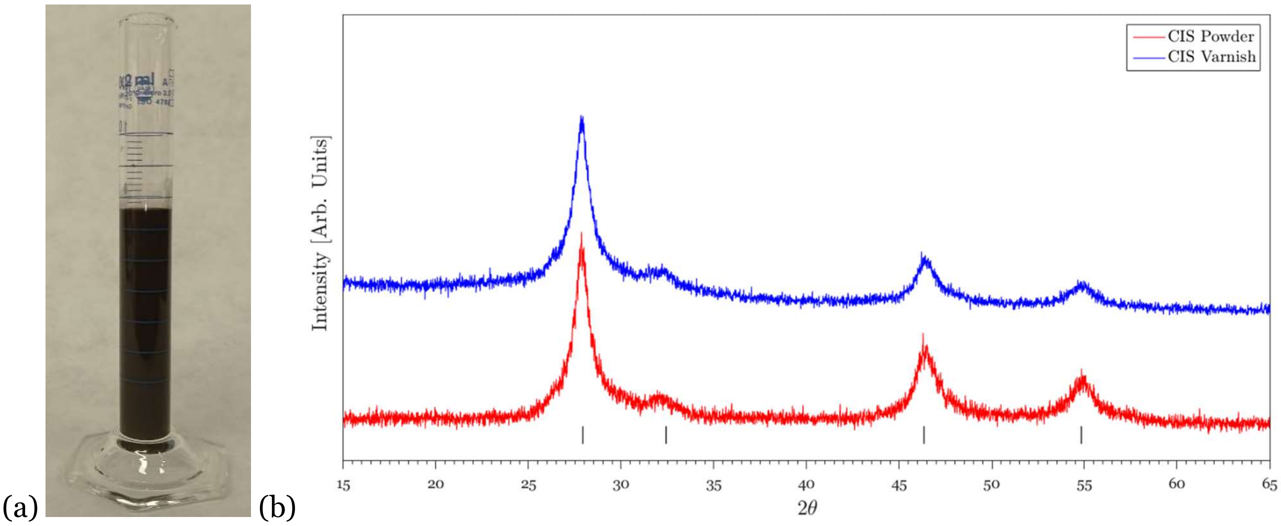

Figure 5.5: (a) Fresh CIS-based PV varnish aspect. (b) PXRD pattern comparison between CIS powder and dried varnish (red and blue line, respectively). Black ticks correspond to reference peak positions.

It is possible to notice the difference between the two patterns: the phase is identical, but the varnish clusters are smaller due to the refinement process; thus, peaks are broader. Under working pressure conditions, the new particle suspension can be maintained for at least a week. Viceversa, up to 3 days in air exposure, dependently on ambient conditions of the laboratory, clusters aggregation mainly occurs in the case of ambient pressure storage. By the way, the only requirement is to avoid solvent evaporation by closing the jar after every utilization.

5.3) VARNISH DEPOSITIONS

Several sample were prepared with fresh CIS varnishes deposited through different techniques such as drop-casting, spin-coating, or room temperature brush painting. Due to the reasons reported below, the last one (i.e., brush painting) was chosen as the standard deposition method for this work. Depending on the purpose of the study, several substrates were selected for these depositions: SLG, FTO, ITO, Mo or Al_2O_3 (sapphire).

The most used substrates were, certainly, FTO and Mo, therefore the reference PXRD patterns of both are here reported in *Figure 5.6* and *5.7*, respectively.

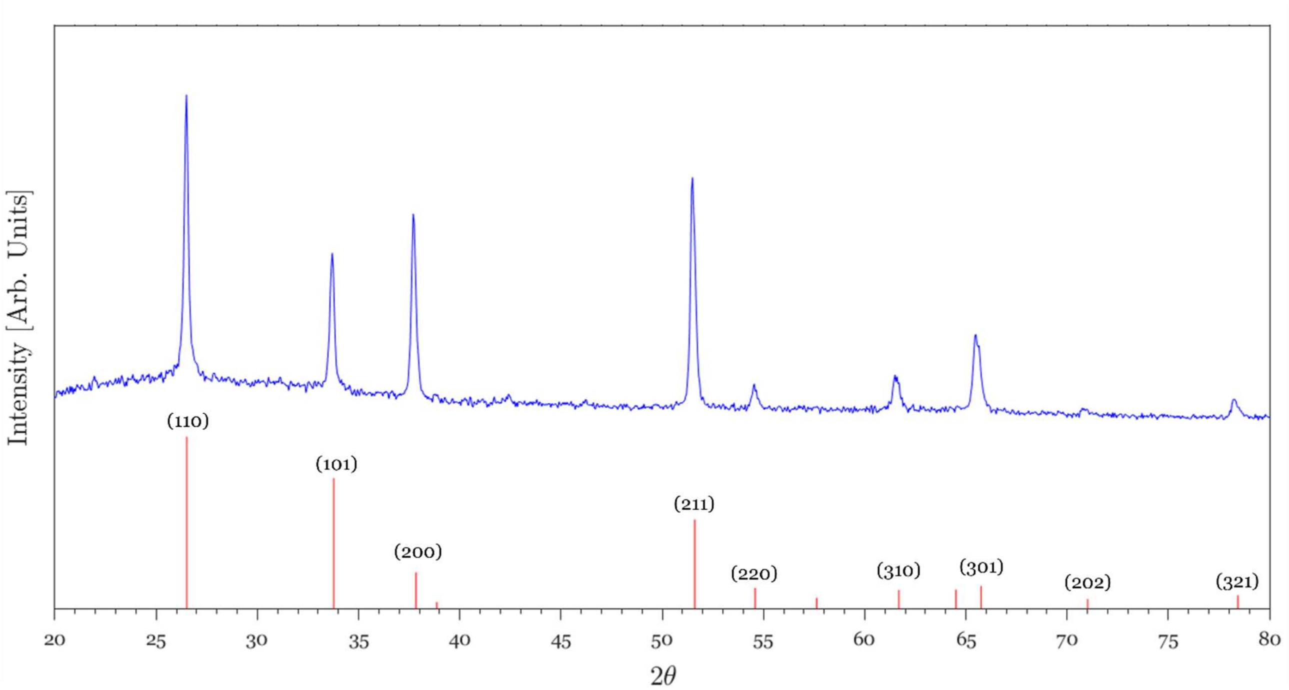

Figure 5.6: Experimental indexed PXRD pattern of bare FTO used in this work. Red lines correspond to peak positions and intensities of reference J. Card No. 00-077-0452.

In *Figure 5.7* is reported the experimental PXRD pattern of bare Mo, as reference. It is necessary to underscore that some minor peaks in the 27°-39° range are not indexed. They belong to a mix of molybdenum oxides with various and indefinite stoichiometries. The Mo_xO_y species are naturally formed on bare sample surfaces during the data collection due to metal passivation by the action of air. It is, thus, impossible to altogether avoid their formation.

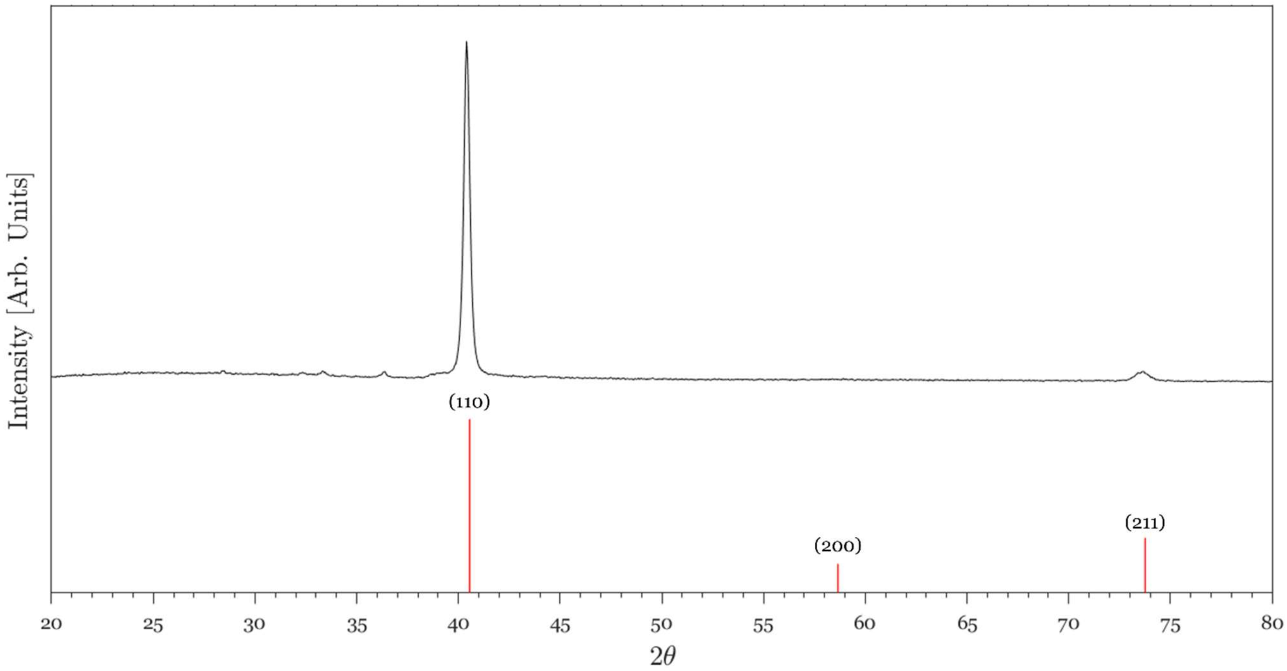

Figure 5.7: Experimental PXRD pattern of bare Mo used in this work. Red lines, correlated by relative indices, correspond to peak positions and intensities of reference J. Card No. 00-042-1120. The presence of a mix of Mo oxides is also noticed but not indexed.

The fresh varnish, just after the refining process, presents low density. The CIS clusters concentration is low; thus, no re-aggregation processes takes place. After several attempts, it has been established that the solvent should be kept free to evaporate for at least one hour after the end of the refinement before any deposition could take place. This allows to concentrate and reaggregate a little bit the suspension and make it suitable for brush deposition. The role of ambient humidity, in principle, can influence the suspension. For this reason, a test sample was painted about every 20 minutes to evaluate the best covering. Once the latter was homogeneous, the jar could be closed again, limiting the varnish evaporation process, so fixing the ideal density of the suspension. The varnish is, nevertheless, sensitive to ageing. After about two days from preparation, the phenomena of re-aggregation, favoured by the increased concentration, cause partial or complete CIS particles precipitation. Deposition with such an aged paint is, thus, almost compromised.

Experimentally, the varnish was gently mixed before deposition. All substrates (1.5 cm^2) were carefully washed through sonication hot baths in distilled water, acetone, ethanol and i-PrOH (5 minutes each); then dried with a flow of pure nitrogen. Subsequently, the brush was dipped without touching the bottom of the jar to avoid the collection of larger aggregates already deposited. The tip of the brush was then placed on the cleaned substrate and tilted by about 45°. The track followed the contours of the sample along the four sides. Simultaneously with the translation, the tip was gently rotated to obtain the most homogeneous layer possible. If the supporting sample holder was not inclined, it was easy to observe the subsequent pretty homogeneous coverage of the surface. A small bubble of varnish was thus formed [*Figure 5.8 (a)*]. During the drying process, thanks to the fast evaporation of i-PrOH, it was observed a first narrowing of the from the sides towards the centre of the substrate. After a seconds, the bubble was reduced to a circular drop surrounded by a flat but still wet zone. Depending on ambient conditions, the solvent evaporated entirely in a few minutes. The result was a homogeneous distribution of CIS, as reported in *Figure 5.8 (b)*. Moreover, the homogeneity was checked through an optical microscope [*Figure 5.8 (c)*].

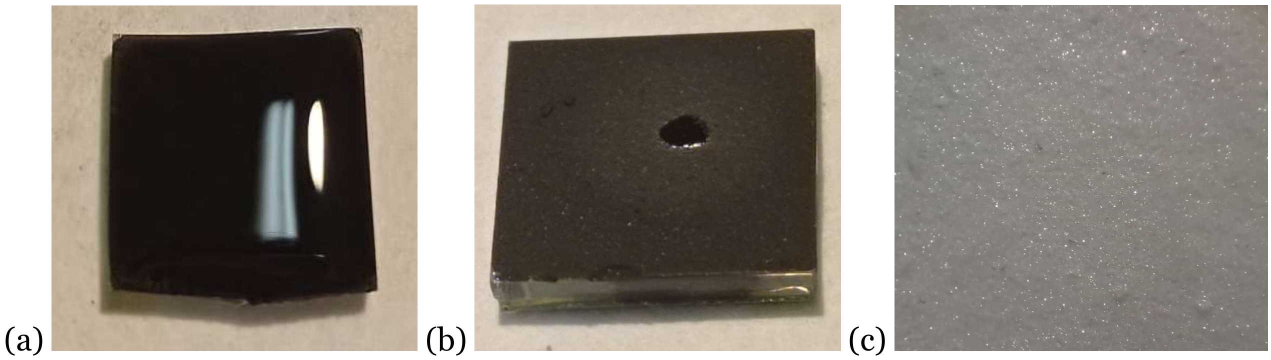

Figure 5.8: CIS paint on FTO substrate. (a) Varnish bubble after brush deposition. It is possible to notice the light scattering on the liquid surface. (b) Dried powder distribution. (c) Homogeneity evaluation at optical microscope (30x magnification). Light dots are the effect of light reflection on CIS crystallites.

5.4) A “4 STEP” DENSIFICATION PROCESS

After the deposition process, each painted sample needed a proper treatment in order to create a stable CIS thin-film suitable for PV application. This passage was fundamental to obtain a working device. Without sintering or an annealing process, the grains would remain isolated, and no electrical or physical continuum could be defined. In addition, the high surface area of the sub-micrometric powder would prevent the carriers from moving freely in the layer and, therefore, from being extracted from the solar device. However, since the layer is deposited at standard ambient conditions, its frailness is clear. Thus, the processes discussed in this paragraph are devoted to improving CIS layer uniformity, compactness and adhesion to the substrate.

In the beginning, we tested a procedure based on hot sintering (HS) of the sample in order to merge contributes of both pressurization and annealing.[119] A hydraulic press equipped with heated metallic plates was used for this process. Before starting the HS, a smaller square of SLG (around 1 cm^2) was placed on the powder sample being careful to locate it inscribed to the larger bottom substrate. The aim was to smooth and flatten the CIS layer as much as possible and protect it from direct contact with metallic plates. The standard treatment was settled at 150°C for 60 minutes and 3.33 Kbar on the deposited layer. The excellent sintering results made the samples durable under a strong blow of compressed air [*Figure 5.9 (a) - (b)*]. Moreover, the empirical scotch test was done to test the actual adhesion of films in critical conditions. *Figure 5.9 (c)* reported that the film partially resists to these stresses. Thus, the homogeneity is not assured with this treatment.

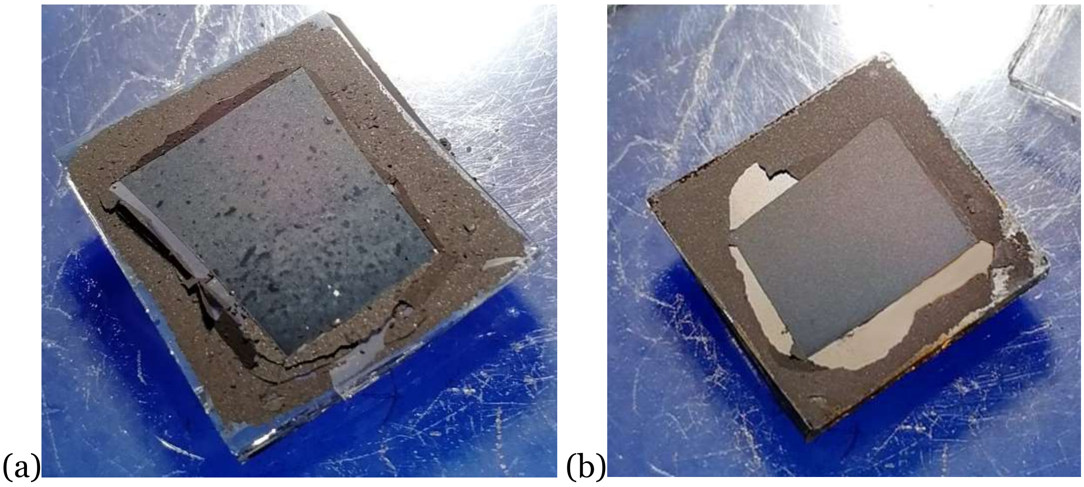
(a) (b)


(c)

Figure 5.9: (a) FTO sample just after the hot synterization process and (b) Mo sample treated with a strong blow of compressed air. (c) Scotch test on a FTO sample: in the left side of the image the film's adhesion is not homogeneously performant.

Such inhomogeneity was evident in the subsequent passage of buffer layer CBD. Most samples exfoliated during the deep coating process due to an unfortunately only apparent adhesion to substrates. This effect is a direct consequence of the non-linear pressure ramp during the hot synterization. Despite the outstanding aspect, this led to an overall inhomogeneous synterization and adhesion to substrate. Once dipped in CdS bath, the liquid percolated in the less synthesized zones, causing the complete detachment of the layer. Due to the issue reported above, the layer sintering should be obtained with a more controlled and gradual increase and decrease of pressure, obtainable by changing the loading apparatus.

The HS process was thus modified and divided into four parts. This whole "4 step process" (4SP), fully reported below and in *Figure 5.10*, allowed to deposit both layers constituting the p-n junction and to make them interdiffuse and lock together . Overall, the new 4SP was calibrated to replace the previous two (i.e., HS followed by CBD), obtaining, as it will be shown , improved results.

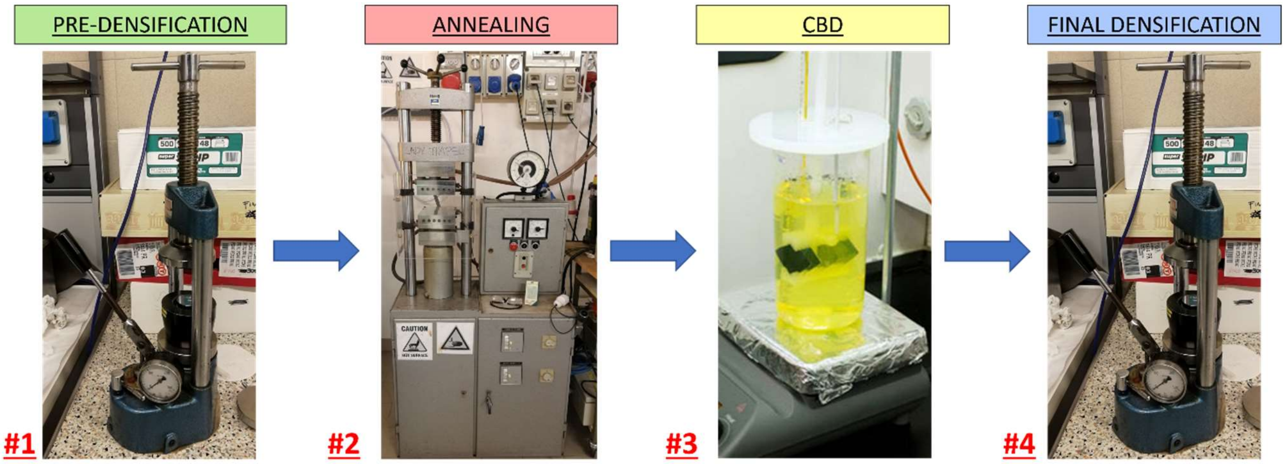

Figure 5.10: Graphical representation of 4SP presented below.

The 4SP is reported as follows:

<u>Step #1</u> - *Pre-densification.*

Fresh deposited samples were pressed through a commercial hydraulic jack. As a standard process, they were pressed for 15 minutes at the effective pressure of 2 Kbar. In addition, the top, pressing glass surface area was properly cut to cover the total area of sample in order to expand the sintering area, differently to what done in previous cases explained above. The applied pressure increment was finely controlled thanks to this instrument, leading to an overall improvement of homogeneity of the CIS layer. In *Figure 5.11* two attempts to directly evaluate the effects of cold pre-densification on an excellent coated FTO sample are reported; the average thickness were recorded by SEM cross-section analysis. Remarkably, homogeneous films with a thickness of just two microns are reproducibly obtained through a completely manual deposition.

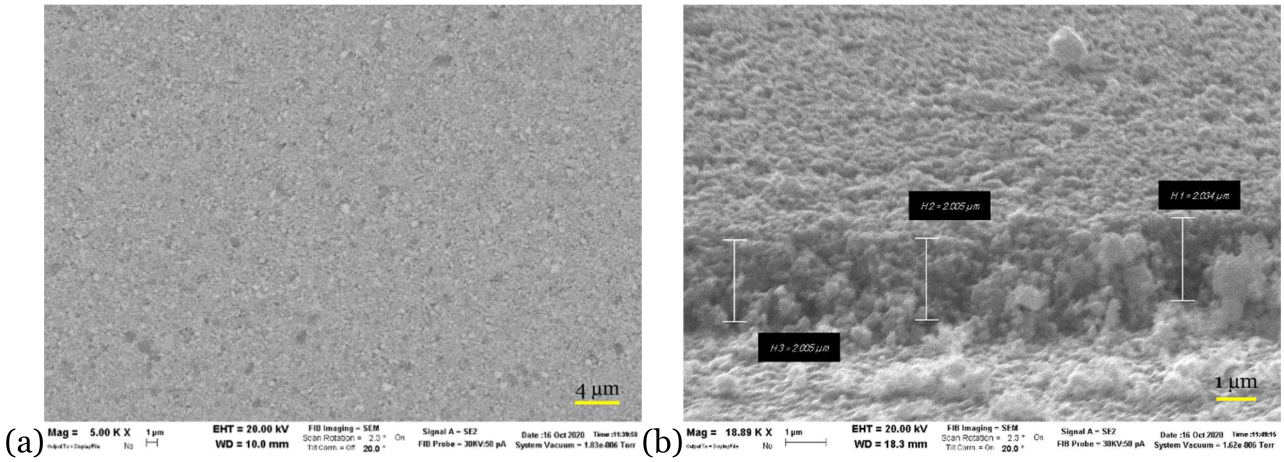

Figure 5.11: (a) 5 kX magnification on a pre-densified sample. (b) Cross-section evaluation of thickness by SEM analysis. A value of 2 µm was obtained.

<u>Step #2</u> – *Annealing.*

The second step is the annealing in ambient air of the sample, using the same instrument for hot synterization just as hotplate without applying any pressure. This step have the purpose of increasing the adhesion of thin-film to the substrate and enhance the crystallinity, improving grains dimensions. Samples were treated, as standard, for 60 minutes at the temperature of 150°C in air. Considering that CIS is a sulphide, sulphur sublimation is quite easy to be sublimated due its high vapour pressure. For this reason, long times and low temperatures were preferable. However, a mean value of 2% sulphur losses have been detected, as reported in *Table 5.4.* The solution to this issue will be discussed in chapter 6 with the introduction of dopants.

Table 5.4: EXD compositional analysis for CIS after step #2.

	Cu (%)	**In (%)**	**S (%)**
CIS as deposited	23.36	27.13	49.52
CIS after step #2	24.52	27.89	47.59

Step #3 – CBD.

The buffer layer deposition is one of the core part of our 4SP. In this case, the film homogeneity was improved by previous steps in order to guarantee the good adhesion of the thin CdS layer on CIS. Thus, the sample detachment was not expected. In addition, the nanometric CdS particles manage to percolate through the sub-micrometric CIS film grains boundaries, filling it and forming a flatter overall layer. Therefore, the deposition of about 120 nm CdS was required. The calibration line, reported in *Figure 2.13,* foresees 25 minutes of CBD exposure under standard conditions to deposit 120 nm of material. This led to the formation of large cracks on the buffer layer surface (*Figure 5.12*), detrimental to the device's performance. In addition, the prolonged deposition led to the formation of CdS grains of too large dimensions. Thus, the overall CdS layer was deposited via two identical CBD processes of 12.5 minutes each.

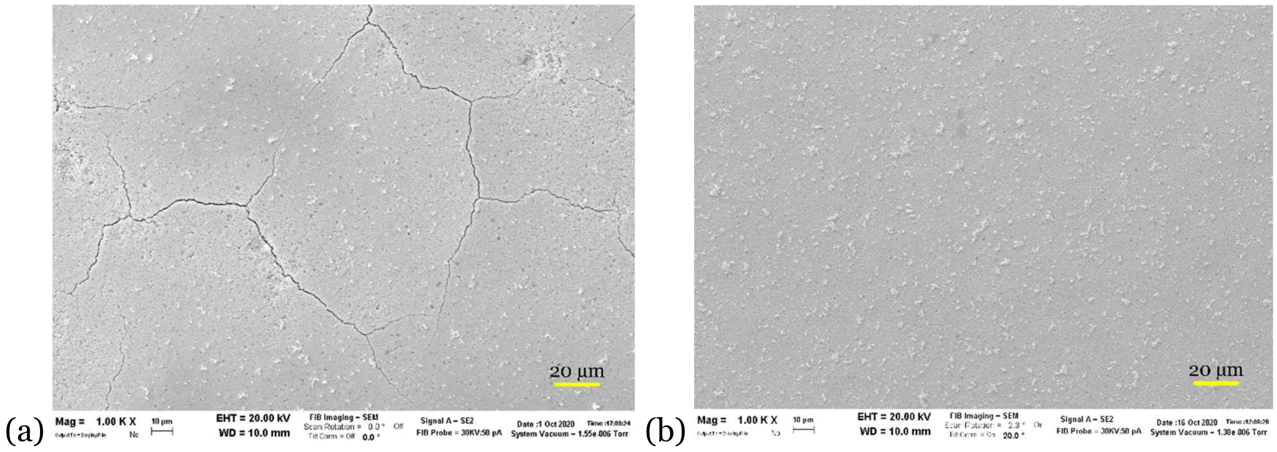

Figure 5.12: (a) Cracks formation on sample treated with a single 25-minute CBD process. (b) The introduction of two half-time depositions allows the obtainment of layers without apparent defects.

With this method, it is verified the deposition of nanometric material in both passages, and the formation of large clusters or undesired aggregates is effectively limited. The modified process consisted of simply changing the reagent solution. The sample treated for 12.5 minutes was removed from the first exhausted CBD solution and immersed in a washing solution, pre-prepared at the same temperature and pH. This was done to remove undesired superficial aggregates and spurious phases from the film without exposing the film to the critical drying procedure; this carefulness allows the operator to replace the exhausted solution with a fresh one without compromising the whole deposition. The sample was thus immersed in the new CBD solution, and the deposition could reach completion. On the other hand, the drying process was carried out through a very gentle nitrogen blow on the sample surface to prevent cracks or film delamination.

<u>Step #4</u> – *Final densification.*

The last step, in analogy with the first, consisted of a densification through the same hydraulic jack. Although the CdS deposition compacted and smoothed the surface, many clusters were deposited over it, and it was challenging to remove them, as reported in *Figure 5.13 (a)*. In this case, the pression was fundamental to densify the whole p-n junction in a single, uniform layer and completely smoothing all the remaining CdS clusters [*Figure 5.13 (b)*]. Like step #1, a top, pressing glass to cover the full extension of the sample was used. The effective pressure of 2 Kbar was again applied, this time for 20 minutes.

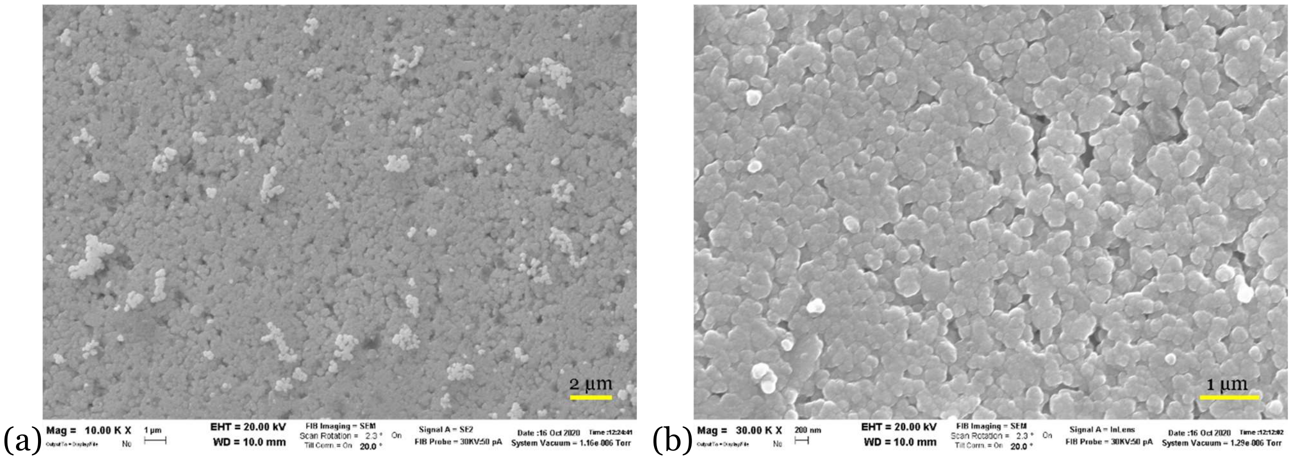

Figure 5.13: (a) 10 kX magnification of a sample treated until step #3, in which CdS aggregates and flakes are very evident. (b) 30 kX magnification of a sample treated with step #4. The final densification of the whole layer is clear, and the synterization of all CdS clusters.

In *Table 5.5* is reported a summary of the standard 4SP correlated by all technical characteristics.

Table 5.5: The standard 4SP, a summary.

Step	Instrument	Sample area (cm²)	Pressure (Kbar)	Time (min)	T (°C)	Repetitions (N)
#1	Hydraulic jack	1,56	2	15	RT	1
#2	Hot Plate	1,56	/	60	150	1
#3	CBD	1,56	/	12,5	60	2
#4	Hydraulic jack	1,56	2	20	RT	1

As reported in *Figure 5.14*, the 4SP obtained extraordinary results in thickness, homogeneity, and adhesion simply starting from suitable varnish coated Mo or FTO substrates. In addition, other substrates and materials were tested with the 4SP but not reported here (e.g., flexible polymers, ITO, or Si). See chapter 7 for details on that.

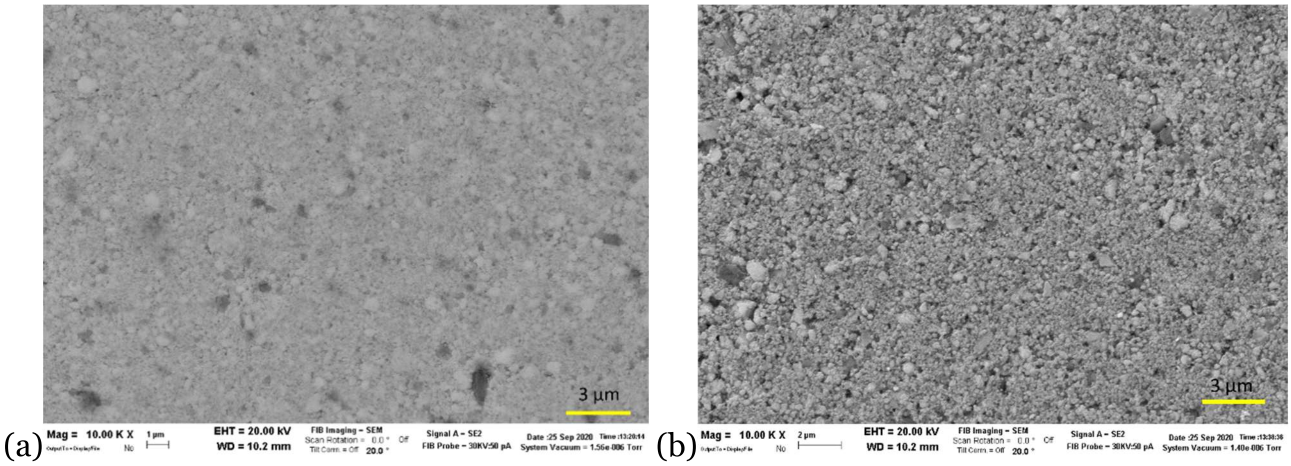

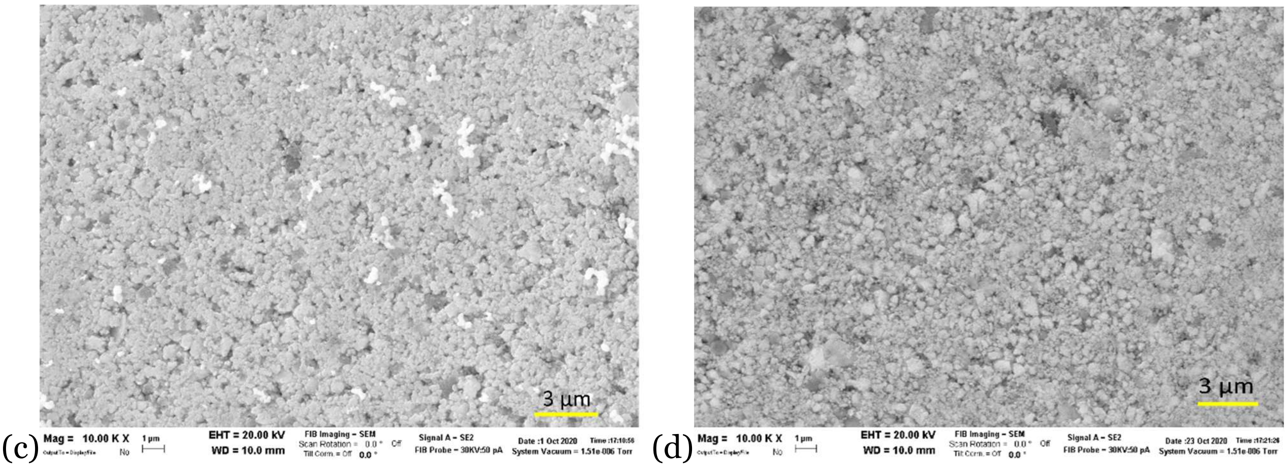

Figure 5.14: 10 kX magnification on a series of samples treated with the 4SP - (a) Step #1 pre-synterization. (b) Step #2: annealing. (c) Step #3: CBD of CdS. (d) Step #4: final densification.

5.5) PRELIMINARY P-N JUNCTION MEASUREMENTS

The results after the 4SP, as extensively reported above, allowed the preparation of whole and fully efficient p-n junctions based on liquid-phase depositions. Before completing the solar device, a careful electrical, optical, and morphological investigation was performed on the solar absorber tout-court and p-n junction.

5.5.1) MORPHOLOGICAL ANALYSIS

AFM analysis was performed on different samples to test the superficial quality and homogeneity of CIS films. The analysis had the objective to study the influence of each one of 4SP on the surface.

It was noticed, as reported in *Figure 5.15 (a)* and *(b)* a measurable reduction of roughness moving from steps #2 and #4. Starting from the as grown deposition via liquid phase, the samples treated via steps #1 and #2, the average roughness value is 37.3 nm, and the presence of several depressions and peaks were noticed. On the other hand, a sample which terminated all the 4SP; showed an average roughness around 18 nm, therefore less than half for the sample after step #2. This result confirms that 4SP effectively increase flatness of the film. It is also possible to evaluate a further characteristics of the sample through this analysis. The CBD process, as previously described, allows CdS clusters to insinuate in CIS's hollow spaces between each grains, filling them: consequently, the average smoothness of the sample was improved.

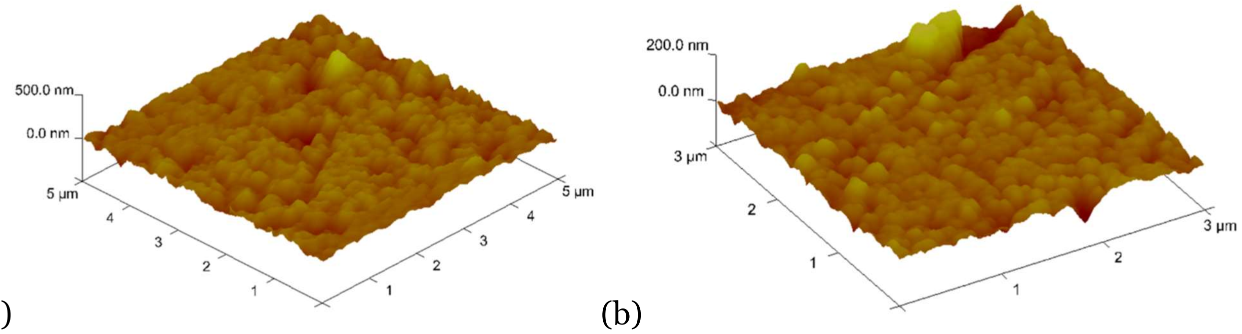

(a) (b)

Figure 5.15: AFM measurements: (a) Surface map of a sample treated until step #2. (b) Surface map of the film after step #4.

To study the heterostructure perpendicularly to the surface i.e., the direction of deposition, several samples were broken and observed in cross-section through a SEM analysis. In *Figures 5.16 (a-b)* are reported two different samples. The thicker one, *(a)*, was explicitly prepared to evaluate the quality of the stacking. It is possible to appreciate each single layer. Differently for the thinner sample, reported in *Figure 5.16 (b)*, it is the case of a standard process, then extensively applied during this work. In this case, it is almost impossible to distinguish the layer of CdS from the CIS layer, being the latter more than 18 times thinner than the CIS absorber; however, its presence can be argued by looking at the top surface where a clearly different morphology of the grains distribution is detected, indicating that a pretty uniform layer of CdS is covering CIS.

(a)

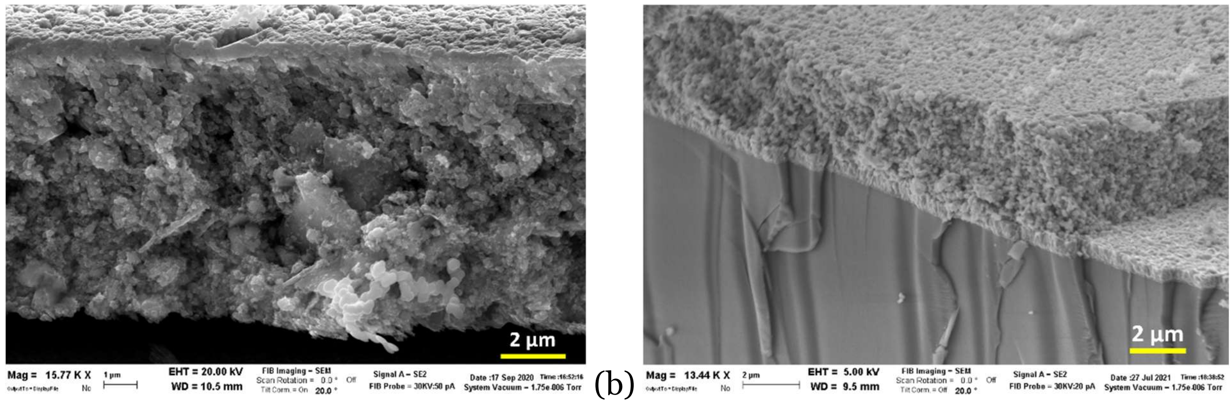

(b)

Figure 5.16: Cross-section SEM analysis on two CIS/CdS pn-junctions. (a) A thick sample: CIS on the bottom and CdS on the top, respectively (magnification of 15.77 kX). (b) A thin, standard,

sample. It is possible to observe the stacking of glass/FTO/CIS/CdS architecture (magnification of 13.44 kX).

5.5.2) OPTICAL ANALYSIS

The following measurements are intended to control and verify the optical properties of our absorber layer. Given the mean roughness of the films, prevented to test the sample in both direct reflectivity and transmission/assorbance configurations, so that diffuse reflectivity measurements collected with an integrating sphere were performed on different samples at different stages of the 4SP and different substrate. The main results are shown in *Figure 5.17*, where the case of two samples painted on Mo and FTO and treated till step #2 were compared. Despite the curves seem to converge and become comparable for wavelength below the energy gap threshold, the integrated reflectivity (characterized by both direct reflected light and scattered light) decreases with a different λ dependence as the energy of the incident light was increased (i.e. wavelength decreased). Particularly, scattered light collected from the sample deposited on Mo mainly originates from the CIS layer since the very flat and homogeneous surface does not produces significant diffusion phenomena. Contrarily for the sample on FTO, the corrugated surface of the conductive oxide increased the total scattered light determining a broader and smaller lowering of the reflectivity across the bandgap than that of CIS/Mo.

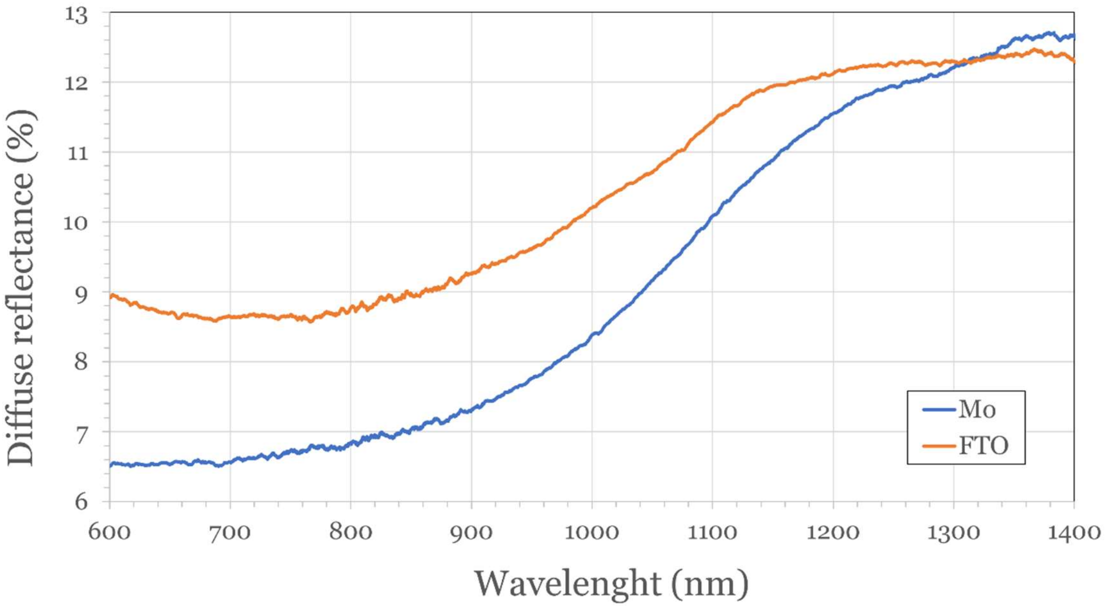

Figure 5.17: Diffuse reflectance measurements for two samples painted on Mo and FTO and treated till step #2.

5.5.3) ELECTRICAL ANALYSIS

CIS is known to be an intrinsic p-type semiconductor. For this reason, a fast evaluation of the sign of majority carriers our CIS painted films, detectable directly from the sign of the Seebeck effect, was necessary to verify that such a film deposition do not alter the intrinsic electrical properties of this semiconductor. Therefore, Seebeck coefficients have to be measured as positive (usually we qualitatively estimated them with a standard multimeter) for each films produced via varnish before undergoing to following processes and characterization. Verified that transport measurements have been carried out to study semiconductor behaviour as a function of temperature. Three samples were compared: an as deposited pristine CIS powder; a film after step #2 and a reference thin-film obtained via LT-PED by a standard target prepared via HIP. The results are reported in *Figure 5.18* showed some analogy between the curves. In any case a semiconductive like exponential trend was detected with different activation energy. The presence of extrinsic doping in painted CIS was explicit and a flatter trend with respect to the reference sample was observed. In the case of the treated painted film, the measurement was extended down to 90 K to properly evaluate the range in which the conductive band was almost empty. Nicely, an optimal resistivity of 200 Ω*cm was recorded at RT, even larger than the reference sample by LT-PED (red vs. green curves of *Figure 5.18*). From that, carriers mobility and intrinsic concentration were estimated around 10 $cm^2/(V \cdot s)$ and intrinsic carriers' 10^{15} cm^{-3}, respectively, thus indicating that it is possible to obtain comparable PV results also starting from a CIS deposited via ultra-low-cost liquid phase techniques, as our method is.

Moreover, if the treated and untreated samples are compared, it is possible to observe that the first is more resistive at low temperatures and that the respective slopes are different. This behaviour was probably ignited by step number #2 (i.e., open-air annealing). The treated sample is less doped, thus conductive, than the untreated. If necessary, conductivity and, consequently device's performances can be improved by adding an extrinsic dopant source during the cell fabrication.

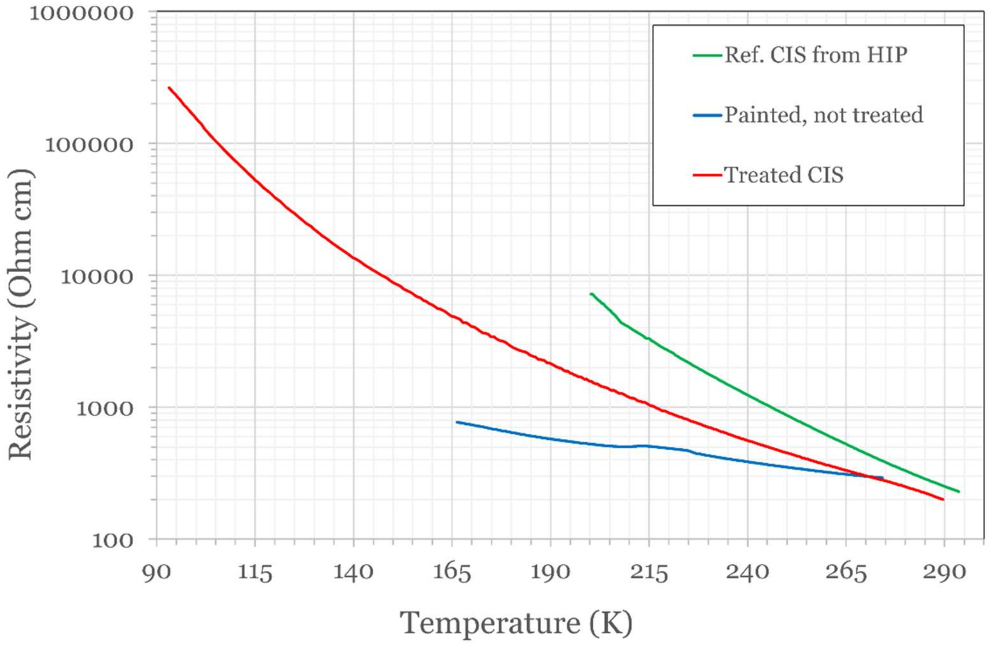

Figure 5.18: Resistivity VS temperature behaviour of painted + treated (#2) CIS, blue and red lines, respectively. The green line refers to a reference CIS based thin-film obtained via LT-PED on a commercial target.

At last, in order to demonstrate the proper working of a p-n junction it is essential to measure a potential (V_{oc}). Very preliminary measurements were carried out and the demonstration of the presence of a functioning and photoactive interface was demonstrated. In the following chapter all the procedures and studies done in order to obtain important improvements on our varnish-based PV devices will be described.

CHAPTER 6

SOLUTIONS FOR IMPROVING PV PROPERTIES TOWARDS THE FABRICATION OF A CIS VARNISH-BASED TFSC

As introduced in chapter 2, a thin-film solar cell based on chalcogenides is characterized by a stacking of different layers: namely a back contact metal or TCO, CIS layer, a CdS buffer layer and two window layers i.e., UZO and AZO which complete and extend the p-n junction of the device and act as a TCO top contact, respectively. Moreover, other processes and characterizations must be considered to improve the device's performance further.

First of all, it is known that intentional alkaline doping of the absorber is mandatory to have a good carriers extraction from the bottom electrode avoiding, at the same time, the formation of electrical barriers and maximizing carrier's mobility.

On the other hand, a fine sub-micrometric distribution of CIS grains, as the one obtained in a varnish, would obstacle the current flow, favouring electron-hole recombination processes. This usually determines an enhancement of R_S and thus a sharp drop of J_{SC}. Therefore, also definition of an effective process of recrystallisation of the absorber is, another mandatory step for improving overall PV character of the cell.

For the above reasons, two different solutions were individuated to improve the PV properties of a CIS varnish-based TFSC:

1. Alkaline doping using NaF;
2. Recrystallization of the solar absorber through annealing.

The two points were carefully and deeply investigated at the same time.

6.1) EXTRINSIC DOPANT ADDITION AND FIRST CELLS REALIZATION

Commonly, as described, principal dopants for chalcogenides are the alkaline cations (e.g., Li^+, Na^+, or K^+).[120-123] Among them, Na^+ was chosen thanks to its small cationic radius, for the great abundance and the ease of use of its main compounds. Na^+ benefits in CIGSe-based solar devices are well reported in literature.[124-125]

At first, we decided to test the Na^+ diffusion by adding a sodium ionic salt directly in the solution used for obtaining the CIS varnish stabilization via high-energy ball milling, as reported in chapter 5. The concentration of this salt should be carefully evaluated: indeed, an excessive doping can determine on one hand, a dramatic increase of the shunt processes and thus short circuiting of the junction. On the other hand, the formation of a continuum layer between the absorber and the back contact could produce a dielectric wall which prevents the current extraction while its intercalation below the buffer layer can damage the depletion layer and so the PV properties.

A very tiny amount of NaF was added in each jar during the varnish preparation. However, the presence of dopant inside the varnish resulted in an enhancement of the solvent polarity, and so in an increased propensity to re-aggregation of CIS clusters.[126] Indeed, whether the dopant is not well dispersed in excessive quantity inside the paint, the increase of the dipole-dipole induced interactions could cause a re-aggregation during the drying step of the painted layer. The effect is clear: an immediate formation of a dense cluster aggregate surrounded by the solvent was observed. During the drying process, due to the formation of random channels in which the solvent flew, the structure of the deposited bubble highlights a series of lighter percolative paths that, starting from the vertex, dispersed towards the border with a sort of dendrite symmetry. The reported behaviour was prevalent on polyimine substrates, each time the varnish was aged and aggregated.

Moreover, an extreme content of dopant could create salt aggregates during the CBD step (i.e., #3 in the 4SP), which have detrimental effects on the whole stability of the film. Namely, NaF is extremely hygroscopic; thus, it could be solubilised fast in the CBD solution, and included directly in CdS thus compromising the overall buffer layer adhesion. It is worth to stress again that we used varnishes to prepare devices following the complex process comprehensively described in chapter 5. However, this does not run out the job, indeed two more layers are needed to complete the cell, specifically two window coating of UZO and AZO, deposited through RF-MS.

The effect of extreme doping conditions in the varnish (i.e., 5% in mass) were initially tested to verify the compatibility of the doping mechanism with such a tricky vacuum technique. The film, which already displayed some adhesion issues before being processed with the RF-MS, after the treatment was totally damaged and/or exfoliated. For this reason, the amount of dopant was gradually reduced, down to 0.2% in mass. For concentrations ≤ 0.5% the process reproducibly showed no exfoliations, caused by vacuum exposition. Therefore, the first complete cells were produced respecting this condition of stability on both Mo and FTO.

6.1.1) CELLS' PV CHARACTERIZATION

The first efficiencies were measured by adding extrinsic NaF (0.2% in mass) in CIS varnishes. Sample grown respectively on Mo and FTO, were selected to be tested in terms of PV properties using the architectures reported in *Figure 6.1*. Both CIS layer were prepared via brush painting on the correspondent substrates, treated with the 4SP and completed with two window layers deposited via RF-MS. Even though different samples were tested to verify the reproducibly of the whole process, no significant variations were collected in terms of the PV properties, thus the following analysis generalized by considering two exemplifying cases, reported below in *Table 6.1 and 6.2* relatively for Mo and FTO. Measurements were performed under AM1.5 solar irradiation in order to test all parameters of the working device.

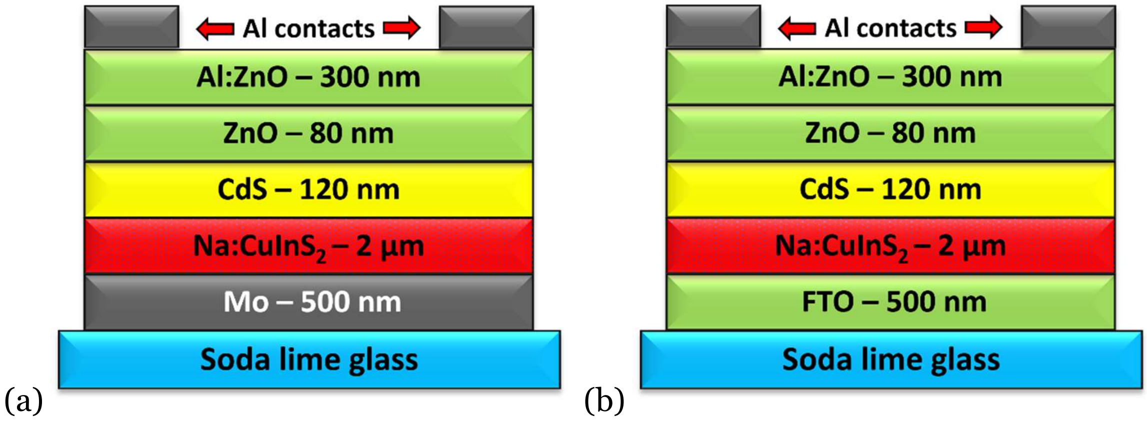

Figure 6.1: Two similar architectures for our first prototypes of solar devices based on CIS painted varnish and doped with extrinsic Na$^+$ (0.2% in mass). Devices distinguish for the back contact element: Mo and FTO for (a) and (b), respectively.

Table 6.1: Mo-based device performances under AM1.5 solar irradiation.

LIGHT MEASUREMENTS			
J_{sc} (mA/cm^2)	2.81	R_s (Ω*cm)	33.80
V_{oc} (mV)	211.68	R_{sh} (Ω*cm)	168.37
FF	0.37	PCE (%)	0.22

Table 6.2: FTO-based device performances under AM1.5 solar irradiation.

LIGHT MEASUREMENTS			
J_{sc} (mA/cm^2)	3.29	R_s (Ω*cm)	25.5
V_{oc} (mV)	319.68	R_{sh} (Ω*cm)	181.45
FF	0.34	PCE (%)	0.36

The cells performances, even quite similar, display some important differences. J_{sc}, V_{oc} and R_{sh} are higher if FTO substrate is used, on the contrary the R_s is lower.

All measurements resulted unsatisfactory if compared with other CIS-based TFSCs prepared via different methods.[127] Values over 700 mV (V_{oc}), 20 mA/cm^2 (J_{sc}) were expected, leading to higher FF and PCEs. The use of a different techniques, like varnish deposition, made the performances improvement a real challenge. V_{oc} and J_{sc} were limited by the low crystallinity of CIS and, at the same time, R_s was very high. As reported in the previous chapter, the ball milling technique forms CIS with low crystallinity. The high number of very tiny crystallites determines the presence of a very high surface vs. Volume ratio. For enhancing the performances of a PV device, R_s should be maintained as lower as possible. In this case, values were relatively high, especially for the Mo-based device. After the layer's synterization and the PV device preparation, the huge number of GBs, prevented the mobility of photogenerated carriers. The high degree of internal recombinations, mainly occurring at the GBs, return very high R_s, reducing at the same time the J_{sc} and V_{oc}, hindering the carriers separation. Moreover, Na^+ seems to have not sufficiently diffused inside the crystallites and along the boundaries, neither wondered in the whole layer. However, in some cases it acts creating some percolative channels that leads to shunt phenomena, thus lowering R_{sh} values.

Standing this, the poor performances are possibly related to the fact that the alkaline doping, introduced via solution, is not effective. Therefore, a punctual study on this aspect was done and reported in the next paragraph.

In addition, the data show other interesting interpretations such as the ohmicity of stratified layers. For the correct working of a solar device, the ohmic contact is fundamental and so the diffusion of dopant in both layers of the back contact (i.e., the substrate and the solar absorber). In this case, Mo acted like a barrier between the SLG, highly doped of Na^+, and the pn-junction. The FTO, on the other side, allowed the free diffusion of dopant from the glass during the annealing step (#2). The doping difference between the substrates and the p-n junction was significant. To avoid both this behaviour and the formation of electrical barriers, it was strictly necessary to improve the Na^+ diffusion, reducing at the same time the concentration difference between the two layers.

Furthermore, tests in dark conditions, reported in *Table 6.3*, were carried out to measure series and shunt resistances in different conditions and study the I-V curves to check if our devices properly behaves as diodes.

Table 6.3: Device performances under the dark condition to test the diode.

DARK MEASUREMENTS			
Mo			
R_s (Ω*cm)	1.62	R_{sh} (Ω*cm)	37000
FTO			
R_s (Ω*cm)	51.27	R_{sh} (Ω*cm)	3569.5

Despite the results on the FTO-based device, in which R_s and R_{sh} values were higher and lower, respectively, the Mo-based cell had the best behaviour under dark conditions. The remarkable difference between an extremely high R_{sh} and a low R_s made the study of I-V curves possible, as reported in *Figure 6.2*.

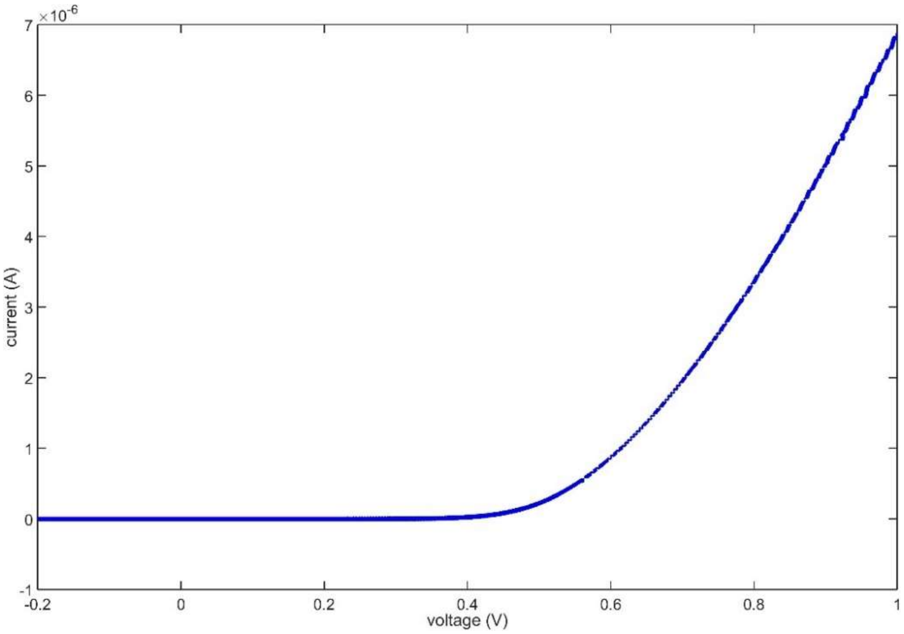

Figure 6.2: I-V curve for Mo-based device under dark conditions of measure. The behaviour is similar to an ideal diode.

6.2) DOPANT VARNISH STABILIZATION AND DEPOSITION

To solve all issues mentioned in the previous paragraph, an in-depth study on new methods and technique to introduce the dopant layers had been carried out. In particular, we studied the possibility of depositing also the dopant suspension via liquid phase, stabilizing a NaF varnish. In analogy with CIS, NaF varnish was prepared by ball milling using i-PrOH as LAG agent. In two zirconia (ZrO_2) jars were inserted in the following order 13 g of zirconia spheres (with 3 mm diameter), 100 mg of pure NaF powder (Sigma-Aldrich, 99.99% purity) and 5 mL of i-PrOH. It was not necessary to control the atmosphere in such experiment; for this reason, pulverisette 7 classic line planetary ball mill was used. The refinement process reported in *Table 6.4* allowed the preparation of a murky white varnish.

Table 6.4: Refining parameters for NaF varnish.

Mass CIS per jar (g)	0,1
Solvent	i-PrOH
Solvent volume (ml)	5
Mill duration (min)	30

Repetitions (N)	34
Total time (h)	17
Pause (min)	0
Reversal rotation?	Yes
RPM*	500
BPR**	130
Mill spheres diameter (mm)	3
Mill spheres total weight (g)	13
Material	Zirconia (ZrO_2)

* Rotation Per Minute; ** Ball to Powder Ratio

The varnish was suitable for manually hand-painted via a brush, like CIS paint. However, in the present case, it was mandatory to avoid the NaF varnish entering in contact with the liquid phase of CBD (step #3). This would cause, as already specified above, the complete detachment of all layers.

6.2.1) DOPANT DEPOSITIONS: INCAPSULATION AND DROP-CASTING

Once the varnish was obtained, a thorough study was necessary to identify how to deposit it not as a uniform and fully covering layer, but contrarily forming a distribution of separated single units of salt crystallites on the substrate over which CIS will be subsequently deposited. This would have allowed to avoid the formation of a dielectric layer at the interface but at the same time to have some "seeds" from which the alkali can diffuse both through the CIS layer and the substrate. After its preparation, it was fundamental to find the correct dilution to afford the most homogeneous distribution of NaF crystals on the substrate. For the sake of clarity, this task was very tough to be achieved since that Mo and FTO roughness were very different. Indeed, once deposited, the dopant varnish begin to dry, and nucleation of NaF occurs. Nucleation mechanisms are different also depending on the interaction with surface. The mother solution was diluted in several batches to test concentration effects on the nucleation dynamics and coverage. Low concentrated solutions (e.g., 25, 50, 75, 100 or 200 ppm) lead to the formation of few but huge crystals (according to crystal nucleation theory).[128] Viceversa, the direct deposition of highly concentrated mother solution led to an almost complete and thick coverage of a chaotic distribution of smaller crystals. Finally, the better conditions were found with a 4:1 dilution of mother solution (corresponding to a NaF concentration of about 300 ppm). In *Figure 6.3*, a sample prepared in the latter condition is compared with another prepared with a less concentrated NaF varnish.

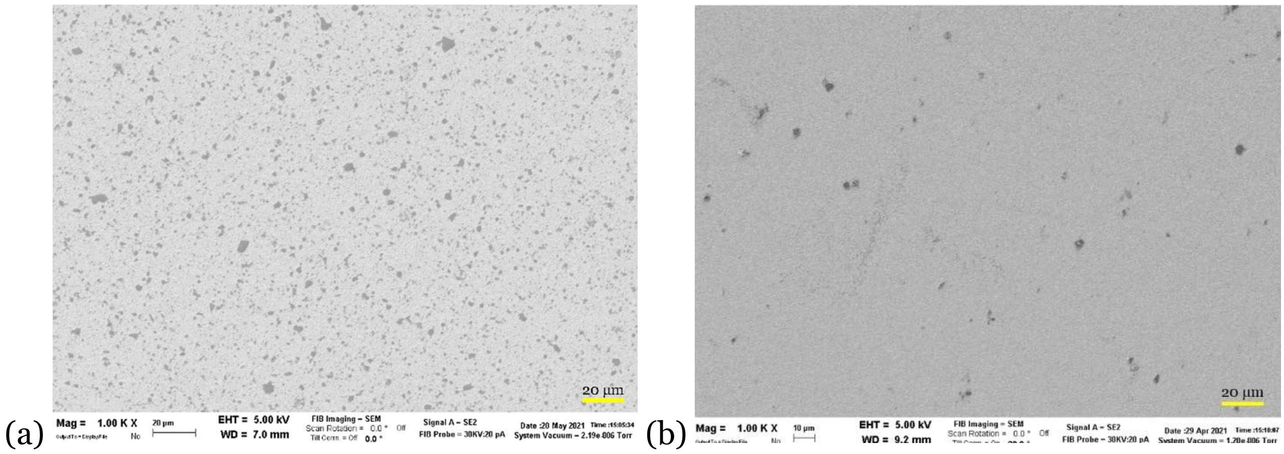

Figure 6.3: 1000x magnification of just prepared NaF cluster distributions obtained with different dilutions of the mother varnish. (a) The desired cluster's distribution with a 4:1 dilution (310 ppm) on FTO. (b) 75 ppm dilution on Mo; noteworthy, the presence of less crystals but of large average size is detected.

After the correct dilution was determined, the focus moved on testing the effect of different deposition methods on the distribution. Therefore, it is necessary to stress the point of the extreme hygroscopicity of the dopant and its effects. Once deposited, NaF must be kept away from the edge of the samples. If the CBD aqueous solution enters in contact with dopant, small crystals could be included in CdS layer during the dry process, undermining its stability in vacuum. In addition, the presence of a bigger amount of dopant between substrate and CIS layers could lead to a direct exfoliation in CBD solution due to liquid percolation.

For reasons reported above, two ways were tested:

1. Paint brushing after an encapsulation through proper mechanical support throughout the borders;
2. Standard µdrop-casting method.

<u>*Encapsulation*</u>

A squared internal area of a substrate was boarded with kapton tape to create a free surface of 1 cm^2. Subsequently, NaF varnish of selected dilution was manually deposited with a small brush. After drying process completed, the kapton framework was removed from the sample, and the distribution thus obtained was covered by a thin layer of CIS. In *Figure 6.4 (a)* and *(b)*, an encapsulated sample and the schematical architecture are reported. Although the encapsulation product seems to be at first sight of high quality, when the sample was subjected to 4SP, it did not survive to CBD of step #3. After the pre-densification step (#1), the coverage of CIS above NaF was not as uniform as for the NaF free sample, greatly enhancing the aqueous solution percolation during step #3. The dissolution of NaF layer occurred and then the physical detaching the entire film, see *Figure 6.4 (c)*. After removal from the CdS solution, the result was a layer of CIS held in tension by an underlying enclosure of liquid. After drying, everything collapsed, leading to the destruction of the sample. In addition, the presence of sharp corners allows forming air bubbles between NaF and CIS [*Figure 6.4 (d)*]. During the annealing step (#2), the latter started to expand, causing the possible microscopic rupture of the layer, favouring again the aqueous solution intrusion during the step #3 and so the destruction of the film.

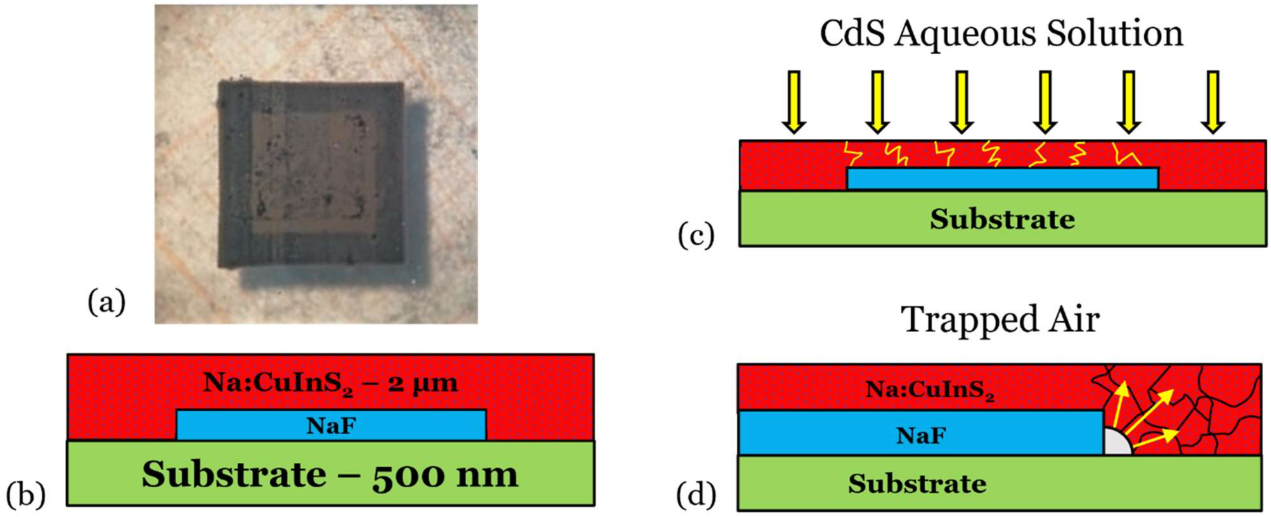

Figure 6.4: (a) The appearance of a sample with encapsulated NAF layer inside it after step #2. (b) A standard architecture for encapsulated samples. (c) Hypothetical model of the percolation mechanism of CdS aqueous solution during step #3 through fissures determined by pre-densification step (#1). (d) Magnified pictogram of possible lateral cracks affecting CIS layer due to air bubble expansion during step #2.

Drop-casting

The second tested method was, as said, the deposition via standard drop-casting through the use of a calibrated micropipette. After a vigorous mixing of the diluted solution 4:1, 70 µL were picked up, and the tiny drop obtained was gently deposited on the chosen substrate. By liquid diffusion and due to the mild capillarity of i-prOH, a roundish zone was formed. This distribution, shown in *Figure 6.5*, was treated through a process specifically designed for each type of substrate (i.e., FTO and Mo). In order to avoid issues observed for encapsulated samples, the reduction of sharp angles that caused the rupture of the previous layers was mandatory. In FTO case, an annealing step in oven (high temperatures, long times) was followed by a cold sintering (CS) in order to uniform NaF distribution and exclude the presence of sharp surfaces. Similarly, for Mo substrates, a comparable but shorter process was necessary, in order to avoid the passivation of metal's surface. Therefore, a direct HS was carried out immediately followed by a solvent trapping removal through a strong flow of pressurised air. Subsequently, the NaF distribution was covered by CIS. In paragraph 6.2.2 are reported in detail all passages, completed by the 4SP.

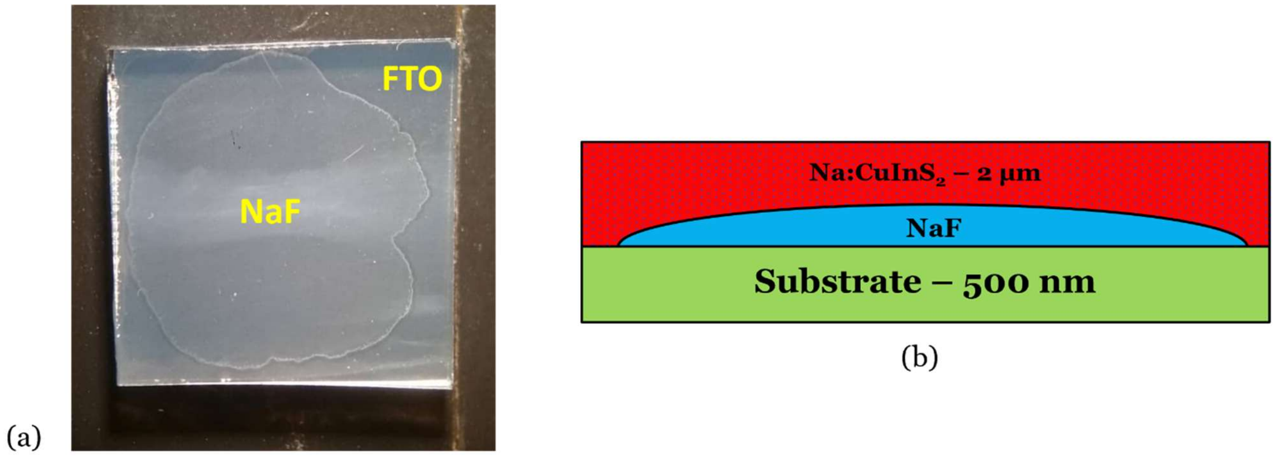

Figure 6.5: (a) NaF varnish diffusion area after drop-casting deposition on FTO. (b) The schematic architecture of drop-casting deposited NaF layer.

6.2.2) NEW DENSIFICATION PROCESSES: AN EXTENDED 4SP

The need of a specific treatment for the alkali dopant after deposition implied a completion of the aforementioned 4SP by adding some steps which are different depending on the substrate considered. Hence, to avoid confusion, the procedures have been renamed as F4SP and M4SP, respectively if a FTO substrate or Mo substrate was used.

F4SP

70 µL of NaF varnish (4:1 dilution) were deposited via drop-casting on a cleaned FTO substrate (#F1). Afterwards, the sample was placed in an oven at 380°C for 15 h to promote the diffusion of the dopant in the substrate through an annealing step (#F2). The last step was represented by CS at 2 Kbar for 15 minutes (#F3) to reduce the presence of sharp angles in NaF crystallites. Subsequently, the sample was painted with a thin layer of CIS, and then the classic 4SP could be carried out as usual: #1 pre-densification; #2 annealing; #3 CBD and #4 final densification. The whole F4SP is reported in detail below, in *Table 6.5*.

Table 6.5: The F4SPsummarised step by step.

Step	Instrument	Sample area (cm²)	Pressure (Kbar)	Time (min)	T (°C)	Repetitions (N)
#F1	Micropipette	1,56	/	/	RT	1
#F2	Oven	1,56	/	15 h	380	1
#F3	Hydraulic jack	1,56	2	15	RT	1
#1	Hydraulic jack	1,56	2	15	RT	1
#2	Hot Plate	1,56	/	60	150	1
#3	CBD	1,56	/	12,5	60	2
#4	Hydraulic jack	1,56	2	20	RT	1

The solid red line indicates CIS deposition.

M4SP

A cleaned Mo sample was immersed in hot distilled water at the temperature of 50°C to remove any molybdenum oxides from the surface (#M1). After 20 minutes, it was extracted and quickly dried through compressed air (#M2). Then, 70 µL of NaF varnish (4:1 dilution) were deposited via drop-casting on a flat support and left to dry at RT (#M3). This metal, in contact with air, tends to oxidise quickly. For this reason, it was decided to avoid the annealing process in oven, utilized in the case of F4SP, to induce dopant diffusion. Differently, it was chosen to hot-press the sample by covering the surface with a top SLG applying 3 kbar for 15 minutes at 150°C (#M4). Finally, to remove all solvent residuals, a strong flux of compressed air was used to dry the sample and to blow away the more prominent NaF clusters (#M5). After this, the CIS was deposited, and again the basic 4SP took place. In *Table 6.6* the M4SP is resumed in detail.

Table 6.6: The M4SP decomposed in all its constituting steps.

Step	**Instrument**	**Sample area (cm^2)**	**Pressure (Kbar)**	**Time (min)**	**T (°C)**	**Repetitions (N)**
#M1	Beaker	1,56	/	20	50	1
#M2	Compressed air	1,56	0.005	1	RT	/
#M3	Micropipette	1,56	/	/	RT	1
#M4	HS	1,56	3	15	150	1
#M5	Compressed air	1,56	0.005	1	RT	1
#1	Hydraulic jack	1,56	2	15	RT	1
#2	Hot Plate	1,56	/	60	150	1
#3	CBD	1,56	/	12,5	60	2
#4	Hydraulic jack	1,56	2	20	RT	1

The solid red line indicates CIS deposition.

6.3) PERFORMANCES ENHANCEMENT IN PV DEVICES

Applying the outcomes of our studies reported in the previous paragraphs, we reported the best cells both on Mo and FTO substrates obtained during my Thesis. The architectures of these two devices are reported in *Figure 6.6*, and all performances collected under AM1.5 irradiation are summarised in *Table 6.7* and *6.8*, for Mo and FTO, respectively. Moreover, these results are then compared with the former cells, produced without the interposition of NaF layer.

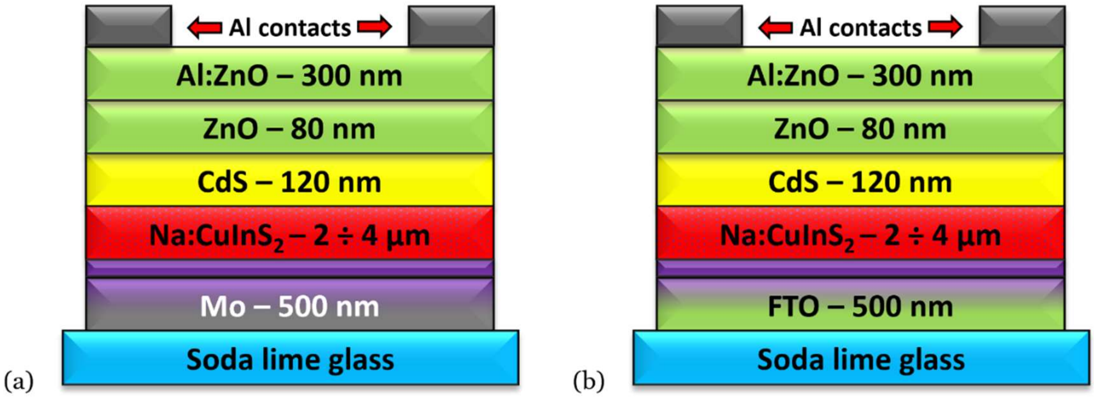

Figure 6.6: Overall architectures of varnish-based CIS solar cells with NaF interlayer by liquid phase (coloured in purple) Mo and FTO, (a) and (b), respectively.

As discussed, between substrate and p-n junction is present a small distribution of dopant, deposited via liquid phase. To favour NaF diffusion in both different layers, the dopant percentage in mass inside the CIS varnish was set to 0.2%. This allows to obtain the highest PCE% values ever on both Mo and FTO, i.e., 0.60% and 0.70%, respectively. A little but significant improvement is observed in almost all the parameters with respect to the former cells.

Table 6.7: Performances for Mo-based device with the NaF interlayer. In comparison, percentage enhancements with the device reported in Table 6.1.

J_{sc} (mA/cm²)	7.65	+ 172%	**R_s (Ω*cm)**	13.93	- 59%
V_{oc} (mV)	250.72	+ 18%	**R_{sh} (Ω*cm)**	121.97	- 28%
FF	0.32	- 14%	**PCE (%)**	0.60	+ 172%

Table 6.8: Performances for FTO-based device with the NaF interlayer. In comparison, percentage enhancements with the device reported in Table 6.2.

J_{sc} (mA/cm²)	7.00	+ 113%	**R_s (Ω*cm)**	21.23	- 16.7%
V_{oc} (mV)	268.11	- 16%	**R_{sh} (Ω*cm)**	95.23	- 48%
FF	0.36	+ 6%	**PCE (%)**	0.70	+ 95%

It is possible to notice the slight improvement of currents extracted (J_{sc}) probably thanks to a larger dopant contribution in passivating grain boundaries; thus, the higher currents are fully justified. Despite this, lowering of V_{oc} and of the R_{sh} confirm the effect of the Na^+ diffusion in limiting and worsening the static charges separation at the depletion layer of the material. Furthermore, even though not optimal, R_s decreases in both cases due to the action of dopant. Other improvements must come into, at this point.

Even if feeble signs of improvement were detected, the results are poor in terms of PV character, not yet comparable with the one obtained for similar chalcogenide-based cell made by the common vacuum techniques all over the world.[129] This tells us that some criticalities were far to be solved. First of all, the drawback of the morphology. We are dealing with an absorber layer constituted by highly defective and fine granulometry, caused by the employed growth technique. Therefore, the following reported study concerns the study of crystallinity improvement and the surface area reduction by exploiting different thermodynamics and processes.

6.4) THE CHALLENGE OF RECRYSTALLIZING THE ABSORBER LAYER

As stated in the previous paragraphs, some of the parameters of the devices with diffused NaF were not improved by dopant contribute. In particular low R_{sh}, high R_s, low V_{oc} and FF, suggested us to modify step #2 (i.e., annealing in air). The low temperatures involved (150° C), even if for long periods, did not allow the optimal diffusion of the dopant in the layers and notable re-crystallization of the film. In addition, crystals coalescence mechanisms did not involve the absorber along the whole volume, but it seems to be limited in the first few tens of nanometres below the top surface, i.e., where the pressure was applied. Indeed, CIS crystallinity was just slightly improved, as shown in *Figure 6.7*. Specifically, in *Table 6.9* shows the relative increase in intensity for the main CIS orientations; although significant, the crystallinity enhancement remained moderate limited at around 10% in the best case for the (204) reflection. As reported below, some reflections did not noticeably vary, others did, but the process which seems much affect this property is by far the CS (i.e., step #1).

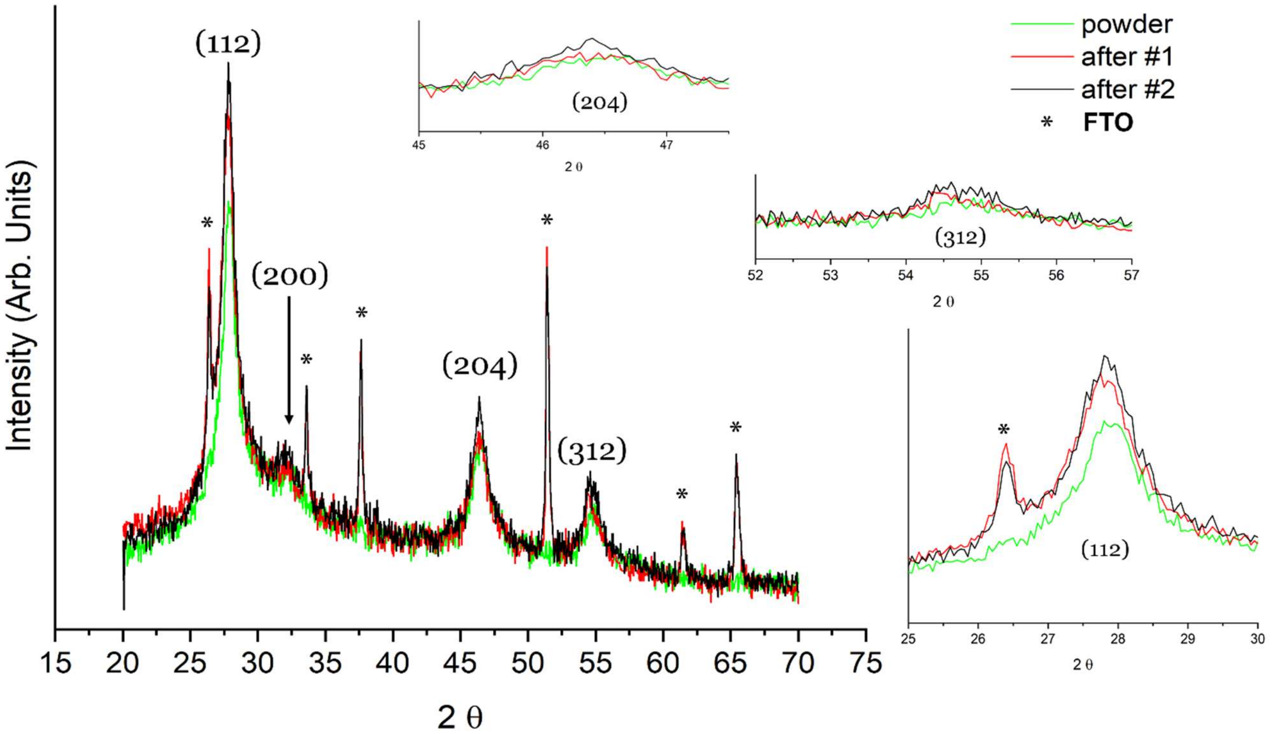

Figure 6.7: CIS deposited on FTO. PXRD patterns were collected after deposition, after step #1 and step #2 (green, red, and solid black lines, respectively). As insets, each reflection of interest magnified to highlight the modest crystallinity increment.

Table 6.9: Relative increase on two particular reflection intensities with respect to untreated CIS (powder, P). (312) reflection increment was not applicable.

(hkl)	P -> #1	#1 -> #2	P -> #2
(112)	21.9 %	6.1 %	29.8 %
(204)	4.5 %	9.6 %	14.5 %

The crystallinity had to be significantly increased to obtain films with remarkable performances. Consequently, a strong increase of temperature combined with the decrease of annealing times was the chosen recipe However, this change could not be done in ambient atmosphere, as we did until this. Indeed, CIS in these extreme condition can decompose through the loss of sulphur for sublimation. As shown in *Table 6.10*, even the mild step #2 causes an average 2% sulphur loss in each sample. In addition, the S^{2-} ions, which have left the structure, can be easily replaced by O^{2-} ions, naturally abundant in the ambient atmosphere. This is a serious issue because oxygen causes suppression of the electrical performances of the chalcogenide, killing the type-p conductivity in favour of a detrimental type-n character.

Table 6.10: CIS's compositions before and after step #2. The 2% loss of S is noticed.

STEP	Cu (%)	In (%)	S (%)
#1	22.9	26.6	50.5
#2	24.1	27.9	48.0

It was, therefore, necessary to study a new apparatus, a closed system to be set in controlled atmosphere. Accordingly, a quartz vial system, reported in *Figure 6.8*, had been designed with the proper valves and cables and thermocouples. To make inert the inner atmosphere, a line of 5N nitrogen or argon was connected as well as a rotary pump (about 10^{-2} bar of working pressure), helpful to clean and purge the system. The maximum temperature reachable by our set-up is 720°C provided by an automatic thermal power unit with an efficient water-cooling circuit for performing rapid quenching of the working temperature.

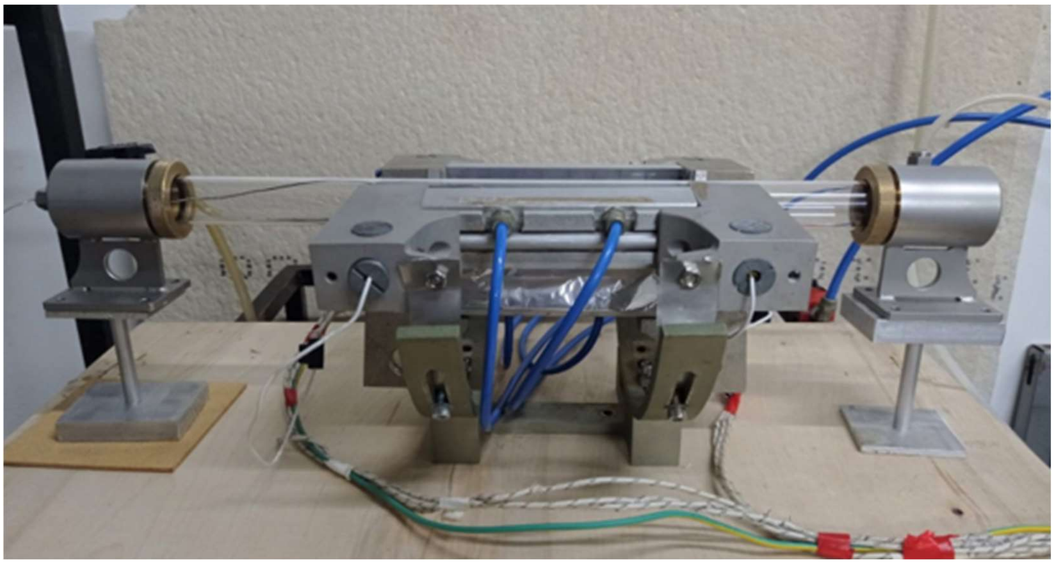

Figure 6.8. The new close system annealing apparatus.

6.4.1) THERMAL ANNEALING IN N_2 AND VACUUM ATMOSPHERES

To avoid the effects described above, the first tests were carried out under constant nitrogen flow, set at 0.2 bar/min. Even for short processes (i.e., 15 min), this led to the loss of sulphur in massive proportions, up to 50%. Thus, the application of a vacuum treatment was tested. The system had been purified with vacuum/nitrogen purges of 30 seconds each (4 cycles before each treatment). After that, the vacuum was achieved, and, thus, the system was closed. At the end of treatment, the samples were quickly quenched in vacuum to RT. The treatments performed at different temperatures and times, led to the results plotted *Figure 6.9*. PXRD patterns clearly show that the crystallinity did not vary up to 450°C, for annealing processes no longer than 15 minutes. At this temperature, CIS grains began to coalesce, and the peaks start to significantly narrow, orders better than the case of standard #2 4SP. However, if this temperature was maintained for too long, it has been recorded a sulphur loss of about 3%.

Furthermore, a sudden change of colour during the return to the atmosphere confirmed that the treatment created S^{2-} vacancies, compensated by O^{2-} during the system's opening. The formation of superficial In_2O_3 is barely perceptible in the treatment at 450°C for 3 minutes and more marked when this temperature was maintained 15 minutes. Treatment at 550°C, on the other hand, completely decomposes the bulk CIS. In_2O_3, in this case, becomes the dominant species.

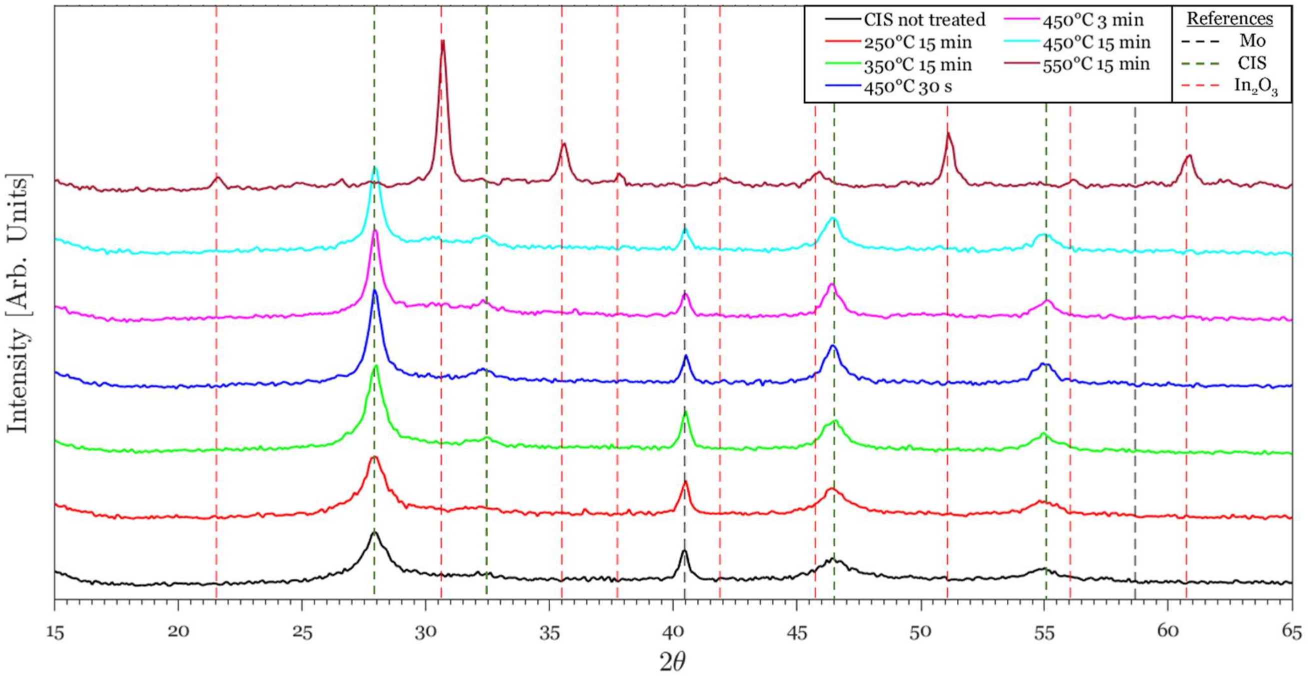

Figure 6.9: Different vacuum treatment of CIS layers deposited on Mo. Red and black dashed lines corresponding to PXRD In_2O_3 and Mo reference peak positions, respectively (J. Cards No. 00-71-2194 and 00-042-1120).

From these results, it seemed that the flash treatment (around 30 seconds) at 450° C could represent the best choice. Although, a compositional analysis, is reported in *Table 6.11*, allowed to notify that the loss of sulphur, even in this case, it is about 2%. This means that such a treatment, from a compositional point of view, showed to give the same unwanted results as the one in the air; therefore, it is far to be optimal.

Table 6.11: Compositional analysis of untreated CIS and a sample treated at 450°C for 30 s the closed vial.

	Cu (%)	**In (%)**	**S (%)**
Not treated	22.9	26.6	50.5
450°C, 30	23.3	28.2	48.5

To avoid any sulphur losses from the film at the temperatures necessary to have good recrystallization, the only possible expedient was to tune the composition of the controlled atmosphere, using the same element, sulphur in gas form to compensate the sublimation from the film.

6.4.2) THERMAL ANNEALING IN S-CONTROLLED ATMOSPHERE

To ensure that sulphur do not escape from the film, a controlled overpressure of the same element was created inside the vial during the annealing. Before each annealing process, 99.99% pure sulphur (purchased from Sigma-Aldrich) was heated on a hotplate, in a Petri capsule, at 130°C for 20 minutes. This treatment permited the degassing of any trace of humidity and/or the decomposition of water based or hydrated impurities. The treated sulphur powder was then stored in a desiccator and weighted whenever needed. After inserting the samples together with sulphur into the quartz tube, the system was purified by vacuum for 5 minutes and filled with nitrogen 5N purity for 30 seconds (flux at 0.5 bar/s). Each cycle had been repeated at least three times. During quenching passage, to prevent the sulphur sublimation from the sample, the atmosphere in the quartz tube was retained until the system was cooled down to 150°C. Subsequently, purge cycles were carried out by vacuum/nitrogen cycles (60 s/30 s) until the system reaches RT. *Figure 6.10* shows the best results for different treatments in sulphur overpressure. Finally, each sample is treated for 30 minutes at 600°C with different aliquotes of sulphur and the data are analyzed by PXRD and EDX.

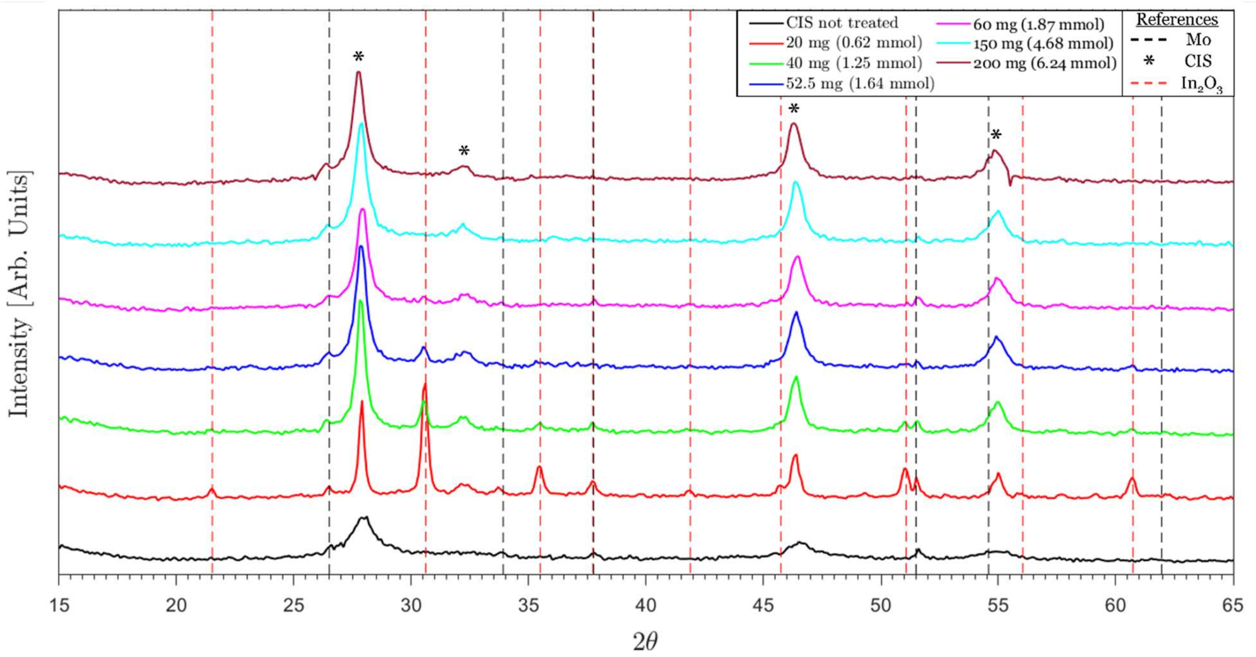

Figure 6.10: PXRD patterns of CIS samples deposited on FTO, annealed in a quartz tube at 600°C for 30 minutes. Different aliquots of treater sulphur are inserted into the system in order to create different internal overpressures. The black and red dashed lines refer to FTO and In_2O_3 PXRD peak positions.

It can be easily noticed the presence of In_2O_3 for a low overpressure (i.e., 20 mg, 40 mg, 52.5 mg and 60 mg). The principal oxide's peak at 30.6° was reduced but, on the contrary, it emergeed that the correspondant CIS's peaks were broader as the intial amount of sulphur inserted in the system increases (thus the internal overpressure). The sample treated with 150 mg of sulphur was the first free oxidation traces. Moreover, the sample treated with 200 mg does not have oxidation, too, but again the CIS's peaks were broadened, sign that the film recystallization was hindered by the overpressure. With larger amounts of sulphur, the recrystallization process was stopped, while at higher temperatures or times, the film was decomposed. Once the appropriate conditions were found, a direct comparison was made with the untreated film, shown in *Figure 6.11*. The normalization of the data allows us to excellently visualize the differences of FWHM between the two patterns. Finally, the treated film is far more crystalline and also less polydispersed.

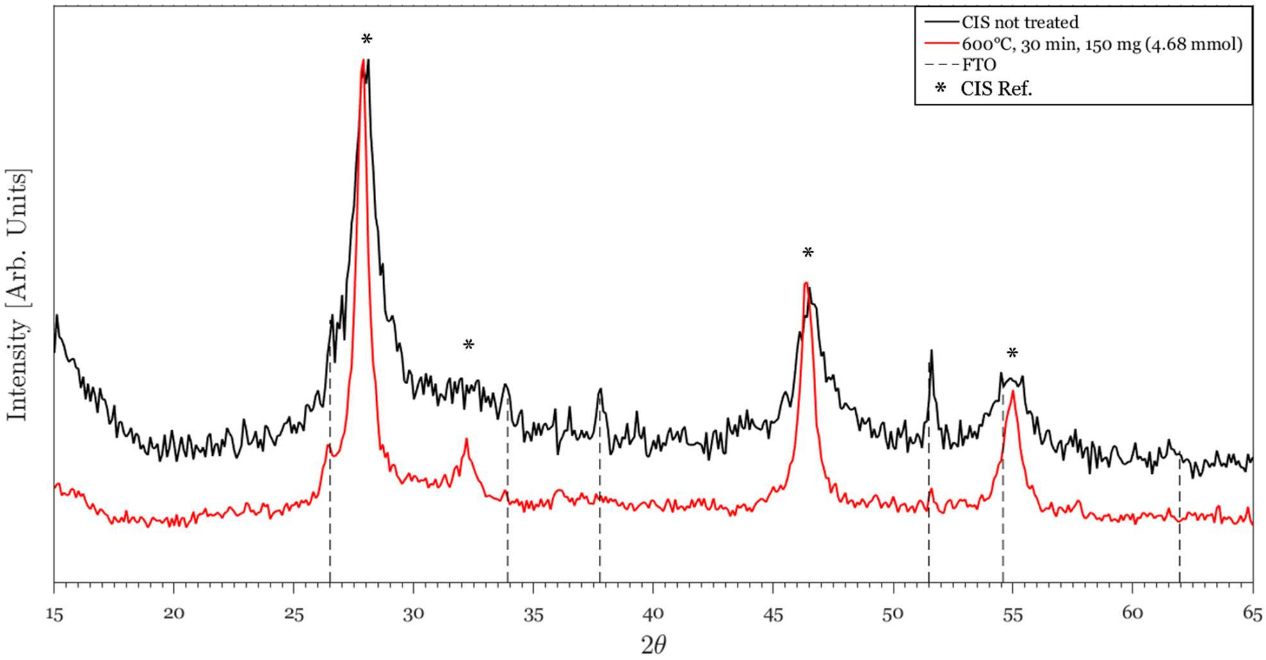

Figure 6.11: Normalized PXRD patterns of the best sample annealed in sulphur overpressure (600°C, 30 minutes, 150 mg) compared to untreated CIS. Black dashed lines refer to FTO PXRD peak positions.

To summarise, the desulphurization process is not stopped if the internal sulphur partial pressure (P_S) is too low. On the contrary, if P_S is too high, the process could cause the irreversible poisoning of film. Considering the very high T_{vap} of sulphur,[130] many attempts have been done to find the suitable P_S. Moreover, once the conditions for sulphur sublimation suppression were defined (i.e., through the use of 150 mg of sulphur), this new process could in principle allow the use of longer times and higher temperatures.

Noteworthy, In_2O_3 is invisible at the eye of a technique such as PXRD if it is located on the surface of the film and present in traces. However, this contamination, being dependent on the exposition of the film at the presence of oxygen in ambient conditions, could slowly increase in the next days and then lead to the worsening of the film quality and performances. So, we decided to comprehensively investigate the ageing of films.

6.4.2.1) AGEING TESTS

Twelve samples were painted on FTO substrates, starting from the same varnish, and stored four by four in three different environmental conditions for 33 days:

1. In a glovebox (with controlled atmosphere of N_2, 5N purity);
2. In a desiccator (< 10% of inner humidity);
3. Directly in air.

After this period, they were treated, as reported in *Table 6.12*. After over a month of ageing, no traces of oxides were detected in any case. High-resolution PXRD analyses were performed and In_2O_3, even in samples exposed to air, was not observed. In *Figure 6.13*, as the most illustrative cases, the high-resolution PXRD patterns of A9 and A12 are compared. Surprisingly, no traces of oxides were spotted. This means that, if present, these oxides are massively formed during the annealing step when the sulphur sublimation was not compensated and properly balanced. In *Figure 6.12*, the high-resolution PXRD patterns of A9 and A12 are compared.

Table 6.12: Aging treatments and storage.

Name	**#1 (pressure)**	**#2 (S overpressure)**	**Storage**
A1	/	/	Glovebox (N_2)
A2	1.22 Kbar, 20 min	/	Glovebox (N_2)
A3	/	600°C, 30 min, 150 mg S	Glovebox (N_2)
A4	1.22 Kbar, 20 min	600°C, 30 min, 150 mg S	Glovebox (N_2)
A5	/	/	Desiccator
A6	1.22 Kbar, 20 min	/	Desiccator
A7	/	600°C, 30 min, 150 mg S	Desiccator
A8	1.22 Kbar, 20 min	600°C, 30 min, 150 mg S	Desiccator
A9	/	/	Air
A10	1.22 Kbar, 20 min	/	Air
A11	/	600°C, 30 min, 150 mg S	Air
A12	1.22 Kbar, 20 min	600°C, 30 min, 150 mg S	Air

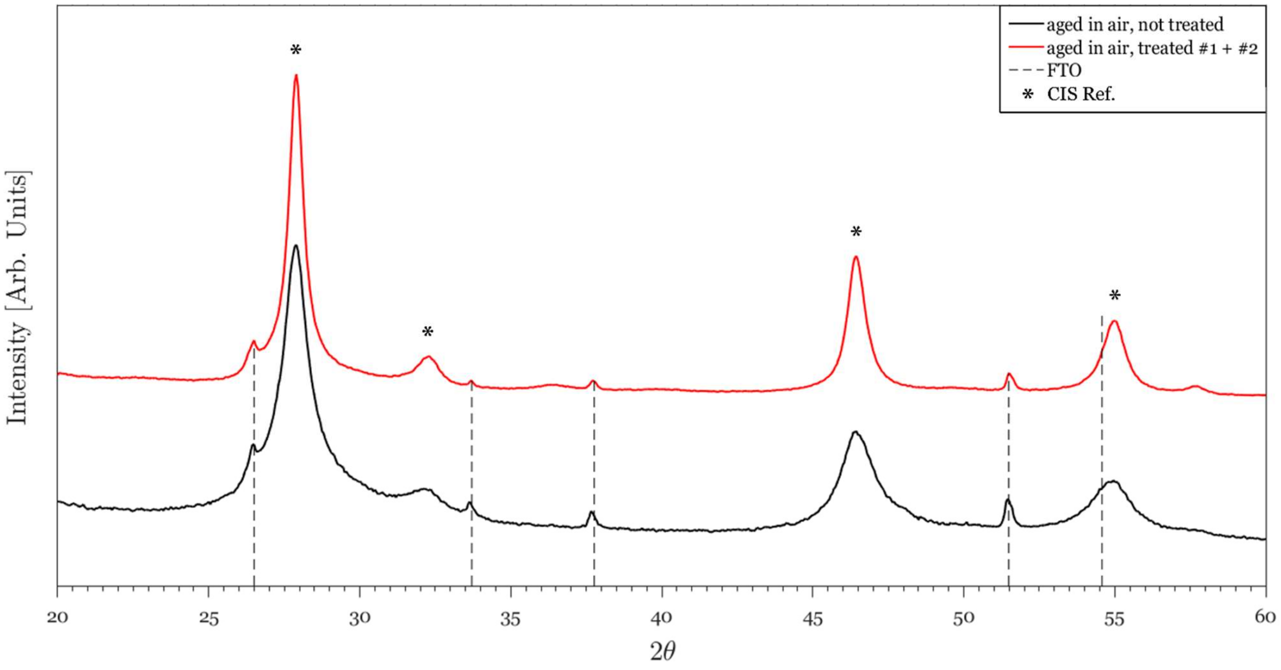

Figure 6.12: High-resolution PXRD pattern of two CIS samples aged in the air: A9 and A12, black and red solid lines, respectively. Both did not report any trace of In_2O_3. Black dashed lines refer to FTO's PXRD peak positions.

6.4.3) ELECTRICAL MEASUREMENTS ON RECRYSTALLIZED SAMPLES UNER CONTROLLED ATMOSPHERE

Despite the very good results obtained in the recrystallization processes, the here reported electrical analyses has underscored some dramatic and not negligible issues. For what concerns the PV properties, although R_{sh} resulted to be relatively improved, it was not possible to measure the open circuit voltage of the p-n junction, and a R_s average value in the order of 1 MΩ*cm was recorded. The complete suppression of the V_{oc} and thus of the whole PV performance was confirmed for all the tested samples.

Such a total compensation of the semiconductive properties of the whole system seems to arise from some chemical/physical effects induced by the annealing process, despite the absence of any oxide spurious phase, and the lack of sulphur residual both with macroscopic and microscopic level on the samples' surfaces, are confirmed almost in all the studied cases. Moreover, several tests were carried out to measure the CIS's resistivity after the annealing treatment in sulphur overpressure. As a comparison, in *Figure 5.18*, it is reported the same measurements after the low-temperature annealing in the air (150°C, 60 minutes). From that an average value of 200 Ω*cm is recorded at RT in our samples.

In the current case, as plotted in *Figure 6.13*, the minimum resistance recorded is close to 80 kΩ*cm, while in worst cases values greater than 1MΩ*cm. It is worth to note that such transport measurements vs. T cannot be extended below 200 K, because measured resistance overcame the instrument sensitivity scale.

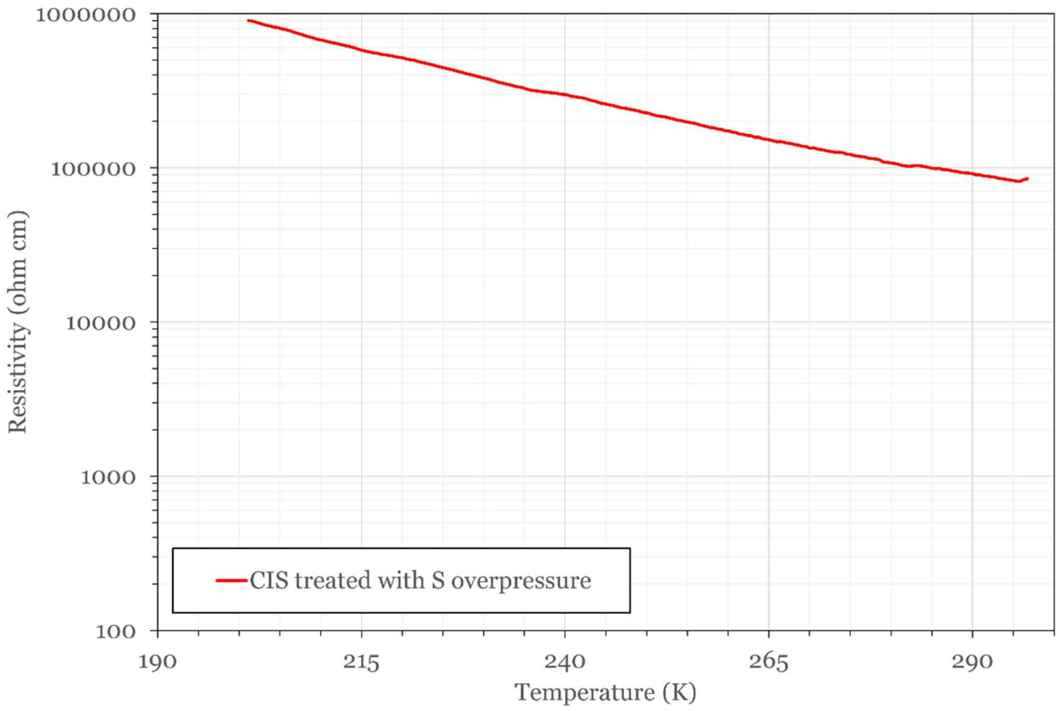

Figure 6.13: Resistivity VS logarithmic temperature measure of a painted CIS sample pre-densified and annealed for 30 minutes at 600°C in S overpressure (150 mg).

A paper published in 2015 gave us some insights to try to understand and address this strange behaviour.[131] Solar materials (e.g., CISe or CGSe) obtained through non-vacuum techniques, especially far from the thermodynamic equilibrium can show the presence of different undesired pollutants. Specifically, if solvents used to prepare these compounds are organics, some molecules may remain trapped in chalcogenide material also after the deposition. This presence of organic molecules, mainly carbon, in the p-n junction could cause severe drawbacks. At first, C pollution could suppress PV performances by significantly increasing the series resistances. Secondly, it may limit the crystalline growth or coalescence of the grains during thermal treatments of annealing. This could happen quickly if the molecules decomposed during thermic treatments. Strong annealing conditions, for instance, are very close to thermodynamic threshold of decomposition of many of the possible trapped organic molecules. In our process, at the energies involved during the liquid assisted ball milling (i.e., the refinement process), organic solvent can possibly partially/locally decompose. However, and more realistically, if the solvent remained trapped in the layer after the brush deposition, it cannot decompose during annealing at low temperatures (150°C), as for the original 4SP; on the contrary, at higher temperatures, like one of the processes in overpressure of sulphur (600°C), this decomposition could become favoured.

6.5) ONGOING STRATEGIES: A NEW BALANCED PROCESS

Summarising the big amount of data and studies presented in this chapter, it is clear that a solar devices based on CIS and prepared by liquid phase deposition have encountered some strong limitations. In particular two main issues were arising i.e., Na^+ diffusion and carbon poisoning. To face them new investigations are currently in progress to solve these critical points, and everything related to them.

For instance, the new idea is focused on a variation the solvent used for stabilizing the varnish, trying to avoid the use of organic liquids. Our starting candidate is water. Thanks to the NaF high solubility in water, varnishes would have a much higher degree of dispersion than for i-PrOH, preventing the formation of aggregates. The problem of the gradient could be easily overcome through the preparation and deposition of several thin layers having different NaF concentrations. Of course, in this case, the high-temperature thermal treatments in sulphur overpressure could be conducted without the risk of creating carbonic clusters in the absorber layer.

Preliminary tests are carried out modifying the refinement step of CIS. Several processes are under investigation, here it is reported the one that at this stage seems more promising. After CIS's mechano-reaction, whose parameters are not modified as compared to those reported in chapter 5, water is inserted in jars with agate spheres. By now, no dopants salts are added inside this new varnish because the initial goal is to verify the feasibility of this experimental solution. After the system's sealing, the refinement began with the two processes reported in *Table 6.13*.

Table 6.13: Refining parameters for the realization of a CIS aqueous varnish.

	Process 1	**Process 2**
Mass CIS per jar (g)	0.5	0.5
Solvent	Milli Q water	Milli Q water
Solvent volume (ml)	10	5
Mill duration (min)	15	15
Repetitions (N)	75	70
Total time (h)	18,75	17,5
Pause (min)	0	0
Reversal rotation?	yes	no
RPM*	300	300
BPR**	4.5	5.6
Mill spheres diameter (mm)	5	5
Mill N spheres	12	15
Material	Agate (SiO_2)	Agate (SiO_2)

* Rotation Per Minute; ** Ball to Powder Ratio

Particularly the second process produced a more stable and homogeneous varnish. If PXRD patterns of two dried aqueous-varnishes are compared with i-PrOH based ones, one can immediately see, that the mean crystallinity of the product (fixed the MC conditions) is lower for the varnish in water than alcohol. As reported in *Figure 6.14*, the use of less solvent with higher BPR and no reversal rotation (i.e., Process 2) produces an excellent varnish in which the crystallinity is very low. This point is essential because mainly the deposition on flat substrates such as Mo will result easier. Furthermore, the aqueous paints are more stable than those obtained with i-PrOH. This is possible thanks to water's properties: shallow vapour pressure, high ionicity and significant surface tension. These characteristics allow CIS's clusters not to reaggregate and remain suspended. It is observed that varnish obtained with 5 ml of water could remain stable for over 6 days; thus, much better than the best i-PrOH varnish.

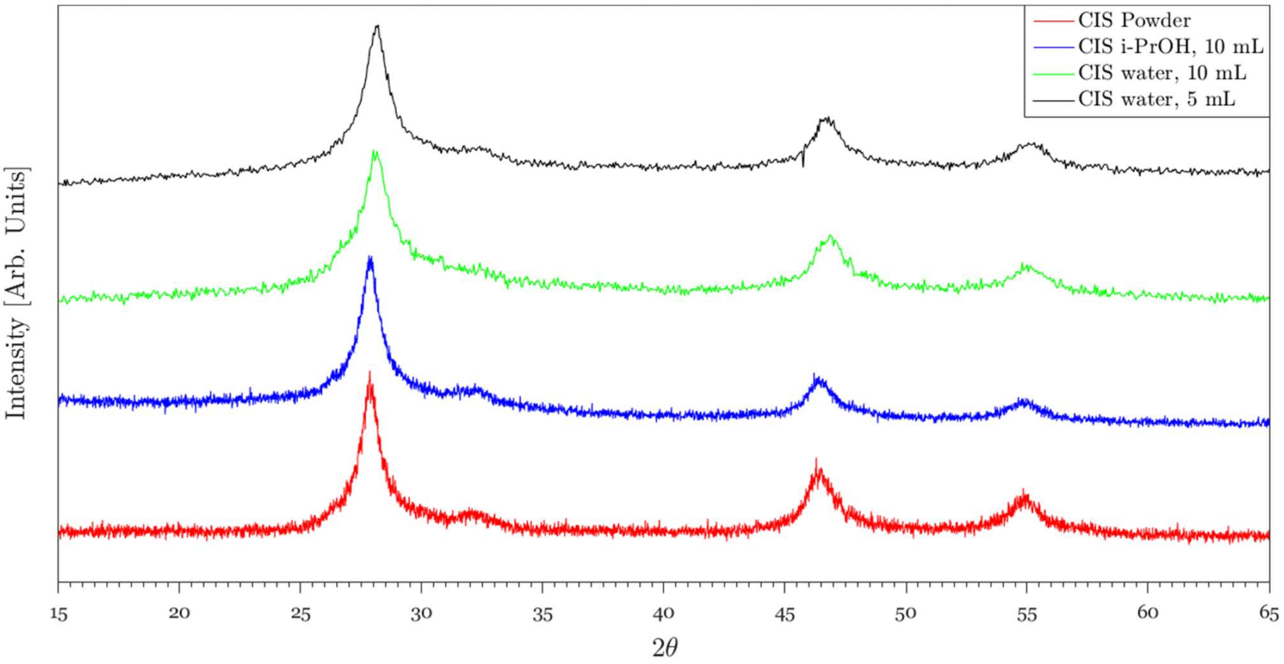

Figure 6.14: PXRD pattern comparison between CIS after mechano-reaction (red line), dried CIS varnish obtained with 10 ml of i-PrOH (blue line) and dried aqueous-based CIS varnishes. Green and black lines correspond to 10 ml and 5 ml refinements, respectively.

Concerning the deposition, due to water's physicochemical properties, the manual painting with the brush is ineffective and inapplicable. Techniques such as drop-casting or spin coating should be used to achieve results similar to those presented in this work. Moreover, the low tension of vapour and the extraordinary surface energy of water make evaporation and coverage very complex processes. At first, samples are deposited via the drop-casting method on a hotplate. A clean substrate is positioned on a 50°C pre-heated hotplate. Immediately, during substrate's heating, CIS aqueous varnish is deposited. After this passage, the temperature is raised up to 80°C to accelerate the varnish distribution and the solvent evaporation. *Figure 6.15* reports all steps of deposition and drying of new water-based paints.

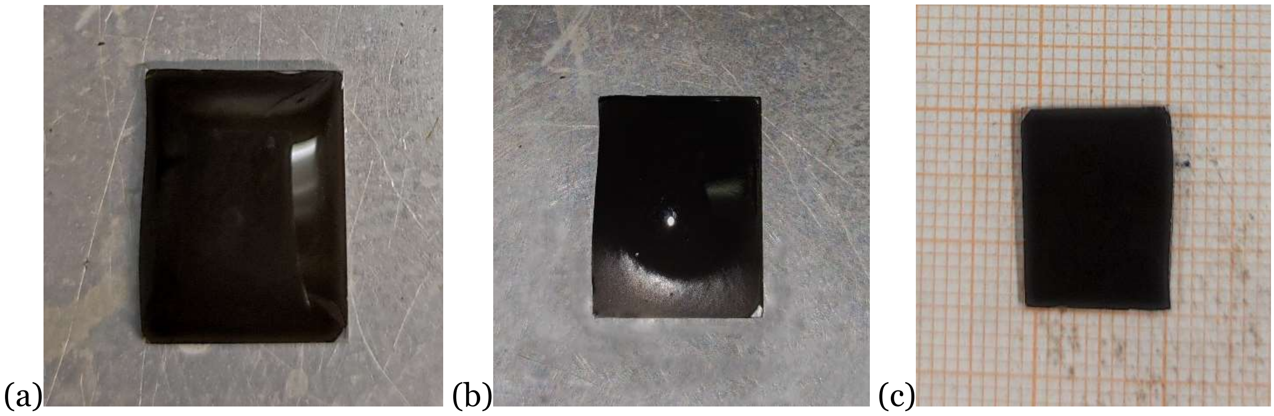

Figure 6.15: Drying process of novel water-based CIS varnishes deposited on bare SLG. (a) Paint pool after drop-casting deposition on a 50°C hotplate. (b) Pool reduction during the dry process at 80°C. (c) Sample obtained after complete solvent removal.

These results, however excellent and promising in every respect, were obtained just before the submission of this work. Due to the lack of time, the process of water-based varnishes will be strongly studied and developed within the project described in chapter 7.

CHAPTER 7

AEROSOL-PRINTING OUR CIS: A PARALLEL STUDY ON POSSIBLE SCALE UP OF THE TECHNOLOGY

7.1) THE INDUSTRIAL PARTNER

The entire work illustrated throughout chapters 5 and chapter 6 represents only a part of the daily efforts spent during my PhD. CIS's paints have also been used as inks through a complementary approach. Thanks to the consolidation of a partnership with Camlin Italy SRL jointly promoted to target EU projects on the field of PV, CIS was alternatively deposited through an aerosol 3D jet printer. All the studies presented in the previous chapters were in parallel developed also in this framework. Private agreements still cover all the stage results and details of this work. In parallel to studies on rigid substrates (i.e., Mo and FTO) done with varnishes, printed samples in collaboration with Camlin Italy were also prepared, to study the property of such printed inks also on different substrates, as polymers, Si, or ITO and dimensions, towards large area. This vast amount of data was fundamental for some ad hoc studies and explicitly devoted for the industrial scale-up.

Furthermore, thanks to the studies on painted samples reported in this work, an important project, with acronym FOURIER, was won in the framework of this collaboration and it is going to in the early 2022. The project's specific objective concerns the print process of CIS and CIGS-based photovoltaic inks to develop an ultra-low cost and green method for preparing efficient solar devices applications in BIPV or tandem systems on commercial silicon cells.

7.2) FLEXIBLE DEVICES

This study had, as aim, the development of stand-alone CIS-based PV devices from a liquid phase process. First attempts were made on rigid substrates (i.e., Mo and FTO) for simplicity, but the focus was to produce flexible polymeric based solar cells. The compatibility test on such intriguing materials is conditioned by severe difficulties due to their physical properties involving samples preparation and processing. The steps involving CS, for example, needed more intense processes. In addition, CBD was difficult because plastics tended to float or sway rather than remain stationary in the chemical bath.

As a consequence, at this stage CIS layers deposited were not very homogeneous. In addition, adhesion, still scarce, is going to be improved by deeply changing the methodology applied until now. Moreover, flexible substrates are related to the sample torsion and flexion. If thicknesses of CIS layers would have been too high, the sample detachment easily occurred. Despite this, with thicknesses less than 2 microns, CIS layers demonstrated to be well adhered and to resist to raw handling as reported in *Figure 7.1*.

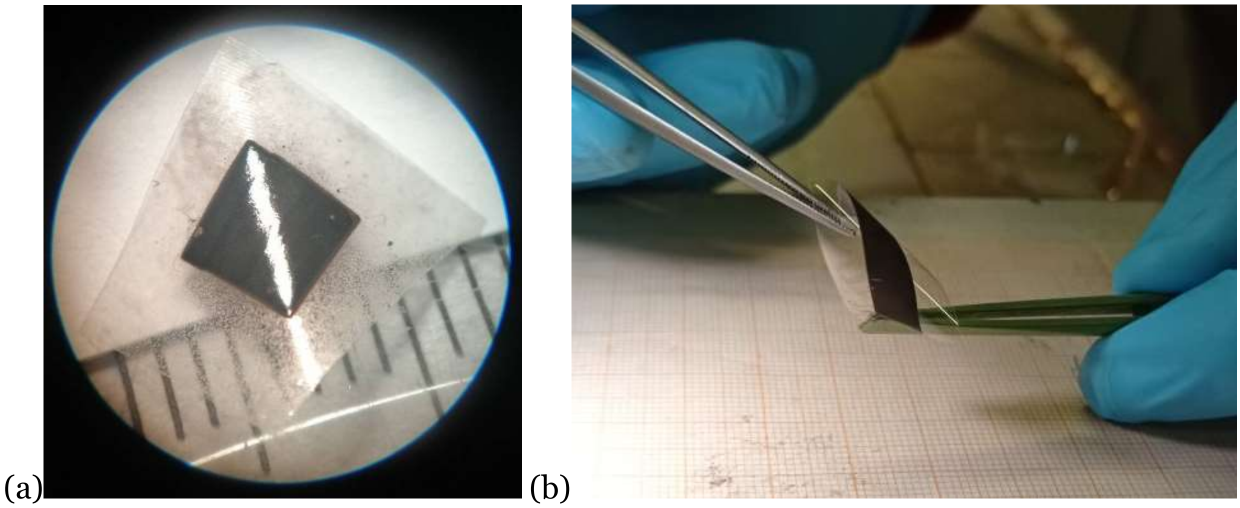
(a) (b)

Figure 7.1: Two examples of CIS samples on parylene after CS and annealing. (a) The smoothness of the surface is evident from the light reflection over the film. (b) A CIS rectangular stripe is manually rotated and tilted to highlight the flexibility and mechanical resistance of our CIS.

For what pointed out above, the study on flexible materials (e.g., parylene, polyimine, PET) is taking an independent route with respect to previous mentioned rigid substrates.

7.3) LARGE AREA INDUSTRIAL SCALE-UP

As mentioned one of the other main objectives of the collaboration with the partner company is to produce commercial modules. The actual area of commercial modules is approximately 256 cm^2, a surface over 150 times larger than those studied up to now (around 1.56 cm^2). PV cells of the increased size of 4 cm^2 are currently printed and sintered via aerosol 3D printing. In *Figures 7.2* and *7.3* are reported examples of 4 cm^2 CIS devices printed both on Mo and FTO. The sample printed on Mo was not treated. It is, therefore, possible to appreciate the homogeneity of raw CIS distribution obtained via aerosol printing

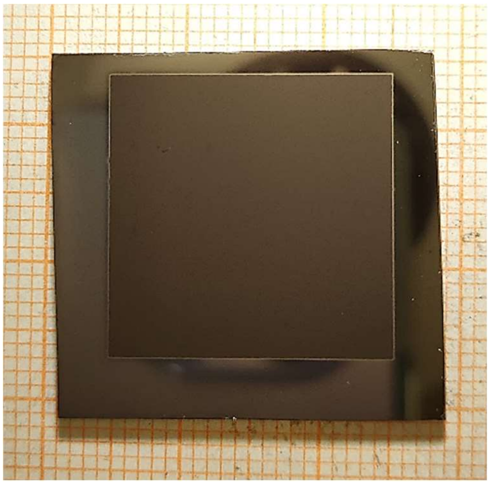

Figure 7.2: 4 cm² printed sample on Mo, not treated.

Instead, the sample printed on FTO was treated until step #2. As a result, it is possible to notice a comparable homogeneity; however some tiny dots and stripings, direct consequence of the printer's needle movements are visible indicateing a still non-ideal deposition process thoroughout such a large area. Moreover, the macroscopical reflectivity under direct light was tested with a simple torch pointed at the sample surface, as shown in *Figure 7.3 (b).*

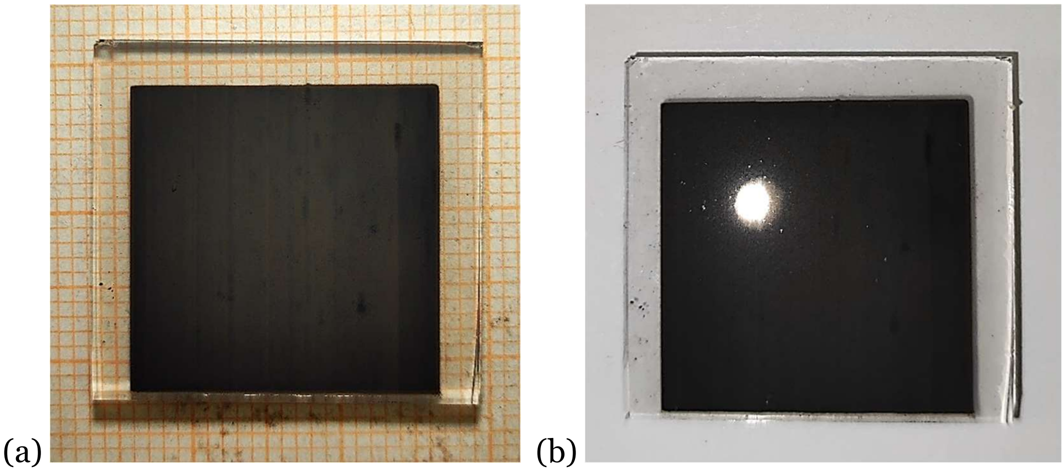

Figure 7.3: 4 cm² printed sample on FTO and standardly treated up to step #2. (a) The image was taken in diffuse light. (b) The picture was taken under direct light, so that the reflectivity of the material can be appreciated.

CHAPTER 8

CONCLUSIONS

This thesis concerned the study of Thin-Film Solar Cell devices (TFSC) with particular attention on innovative layers. Bifacial or flexible thin-film layers based on complex chalcogenides were investigated by physical vacuum and liquid phase depositions. The second-generation photovoltaics is a very wide field: we focused our efforts on finding different layers to improve TFSC performances. An innovative back contact for bifacial solar cell (BFSC) was developed and preliminary studies on an intriguing and promising non-toxic solar absorber were conducted. In addition, a full and comprehensive research was carried out to develop solar cells based on chalcogenides deposited via liquid-phase.

BFSC are in principle capable to collect more light than a standard TFSC, thanks to the use of transparent conductive oxide as back contact. Despite this, the sheet resistivity ($\rho_{\square}$) of such materials is significantly larger than common metals, so performances could be worsened, and bifacial system could be less performing than a standard second generation TFSC. Particularly, for standard Glass/F:SnO_2/$CuIn_{0.5}Ga_{0.5}Se_2$/CdS/ZnO/Al:ZnO cell, for example, it was observed a low shunt resistance (i.e., < 1 kΩ*cm) on a 0.1 cm^2 active area.[103] To improve properties and increase the active areas of bifacial devices, a new mixed Mo:TCO (i.e., transparent conductive oxide) engineered back contact was developed. Theoretically, the presence of TCO can provide more light collection from the rear of the cell, while the use of Mo may consent to have an optimal photocurrent extraction from the absorber. In this case of study, fluorine-doped tin oxide (FTO) and indium tin oxide (ITO) were chosen as TCOs candidates. A photolithographic process, followed by a selective chemical etching and RF-sputtering deposition of the opposite material was standardised to prepare new Mo:FTO and Mo:ITO mixed layers. Mo:FTO back contact achieved up-to-5 times improvement of both active areas and shunt resistances (i.e., 0.48 cm^2 and >5 kΩ*cm). Despite this, due to some critical points related to chemical etching and scarce repeatability, Mo:ITO was chosen as preferential back contact. The new layer achieved promising results: one for all, it behaves like a quasi-ideal diode with shunt resistance up to 0.27 MΩ*cm on 2 cm^2 of active area. The utility of such approach is thus demonstrated, and more studies are ongoing to further maximise the performances of such embedded grids BFSCs.

In the last years, the scientific research on TFSC is focusing on the discovery of new, non-toxic materials exploitable as main components of a solar device, substituting rare and expensive elements with others more abundant and easily available in nature. Namely, it is the case of ASe, a new and competing chalcogenide material suitable as solar absorber. ASe is characterized by a covalent ribbon-like quasi-1D structure, induced by its strong anisotropy. Thanks to this, the photo-generated carriers can flow easily along the ribbons, while, in the perpendicular directions, the transport is limited due to a thermally activated hopping mechanism. To obtain maximum current extraction, a specific process has to be identified in order to correctly orient these ribbons. Specifically, if (hk0) reflections are maximised, ribbons lie parallel to the substrate and the total extracted current is minimum. On the contrary, if (hk1) or, in the best case (00l), reflections are selected, the conduction is improved due to the presence of slanted or normal ribbons, respectively. Thanks to Inorganic Crystal Structure Database and VESTA software simulations, all lattice parameters were investigated both for ASe and a wide selection of material commonly used as substrates for TFSC. Using epitaxial mismatches, an a-priori test was developed to evaluate the best substrate for ASe orientation. It was found that ZnO, FTO and all metals maximise (hk0) reflection group, thus preventing the ribbons' normalization. At the same time, ITO seems to determine random growths. Further studies on ASe deposited via RF-sputtering and subsequently annealed, suggested the use of boron-doped ZnO or ASe itself as a seed layer.[116] An important re-organisation of the structure was noticed during long physical vapour depositions in vacuum, with a remarkable improvement in both (hk1) and (00l) reflection groups. Studies are ongoing to investigate such behaviour and to study new engineered substrates based on undoped zinc oxide nanowires, grown normal to the substrate. Such strongly oriented interlayers could in principle force ASe ribbons to grow parallel to nanowires and so perpendicularly to the substrate.

During my Ph.D thesis, it was also developed a comprehensive investigation on designing and fabricating new-concept TFSC constituted by a $CuInS_2$ (CIS) absorber layer deposited via an ultra-low-cost and green liquid phase techniques. CIS pure and sub-micrometric powders were prepared through a mechano-chemical reaction carried out in a high-energy planetary ball milling machine, then a liquid phase varnish was stabilised with a liquid assisted refinement conducted in 10 ml of 2-propanol (i-PrOH). Subsequently, a brush or drop-casting deposition on a pre-cleaned 1.5 cm^2 substrate (e.g., Mo, FTO, plastics, etc.) was standardized to obtain a uniform and thin distribution of the CIS powder. The thin-film was then obtained through a complex 4 step process (4SP), in which the layer was: (1) pre-densified at 2 Kbar for 15 minutes, (2) annealed at 150°C for 60 minutes in an open-air system, (3) covered with two identical 60 nm thick layers of CdS through chemical bath deposition, (4) re-densified at 2 Kbar for 20 minutes (step #4). The film after 4SP, presents good adhesion, superficial uniformity and flatness. This was checked through both Atomic Force Microscopy (AFM) and Scanning Electron Microscopy (SEM) measurements. In parallel, Energy Dispersive X-ray analyses pointed out an average 2% sulphur loss during step #2. Electrical analysis on varnish-based CIS films underscores comparable values as for CIS deposited via LT-PED. A $\rho_{\square}$ of 200 Ω*cm^2 at room temperature, mobility of 10 $cm^2/(V\cdot s)$ and an intrinsic carriers' concentration of 10^{15} cm^{-3} were achieved.

In order to passivate grain boundaries and improve short-circuit currents, a tiny amount of NaF as alkaline dopant was added (0.2% in mass) directly in the CIS varnishes and the first devices were completed through the deposition of two windows layers of undoped ZnO and Al:ZnO with a RF-MS facility. The first photovoltaic device presented low performances due to the scarce dopant diffusion and CIS low crystallinity: thus, high surface vs. volume ratio and the presence of non-passivated grain boundaries determine a high series resistance (R_s), low V_{oc} and bad currents J_{sc}. For instance, a record 0.22 % Power Conversion Efficiency (PCE) was obtained on Mo. To further improve the device's characteristics, two different studies were independently carried out: (i) a dopant varnish diffusion study and (ii) the definition of a proper recrystallization process for the CIS absorber.

(i) A NaF varnish was stabilised in 5 mL of i-PrOH, diluted and deposited with µdrop-casting on a chosen substrate to create a finely controlled distribution of dopant crystallites. Two different processes were established, for FTO or Mo respectively. In the case of FTO substrates, a 15 h thermal annealing at 380°C, followed by cold sintering at 2 Kbar (for 15 minutes) was necessary; in the case of Mo a unique hot sintering step (3 Kbar, 150°C, 15 minutes) was needed to avoid the formation of oxides on metal surface. Afterwards, CIS varnish was deposited and the aforementioned 4SP was performed. The obtained best devices showed improved PV properties. In particular, PCEs of 0.60% and 0.70% were obtained for Mo and FTO, respectively, and a little increase of J_{sc} and R_s, probably ascribable to a partial yet satisfactory GBs passivation is detected. Despite this, CIS grains ultrafine morphology, which was intentionally sought for granting the varnish stabilization, still represents the main drawback in getting notable photovoltaic performances: so, annealing treatments were strictly required to both enhance CIS crystallinity and induce a more effective dopant diffusion.

(ii) The new annealing apparatus constituted by a closed vial system was specifically designed for permitting the pressure and composition control of the inner atmosphere. After a deep study, in which several parameters were investigated, it was found that the best recrystallization mechanism occurred with an annealing at 600°C for 30 minutes with 150 mg of S inserted in the system in powdered form. Notwithstanding the films obtained through this process are less polydisperse and far more crystalline than the pristine samples, electrical measurements underscore a detrimental $\rho_{\square}$ (over 80 $K\Omega*cm^2$ at room temperature) and a full compensation of the semiconductor. We hypothesized that this behaviour was caused by organic molecules (constituting the varnish solvent) trapping inside the CIS layer. During the annealing process they decomposed, inducing a C poisoning of the film. To avoid both the limited NaF diffusion and C poisoning, a new water-based CIS varnish is currently under investigation. Thanks to the properties of water (such as high polarizability and vapour tension) varnishes' characteristics are improved. The stability is doubled (>6 days) and the deposited layers seems to be as good as for the alcohol-based varnish if a longer and hotter drying process is applied.

In parallel, a study on CIS-ink printability is in progress with Camlin Italy SRL as industrial partner. In the framework of this collaboration, an incoming large project was granted by MISE and, starting from the early 2022, the scalability and industrialization of our technology will be investigated focusing on the production of aerosol 3D-printed CIS solar cells on flexible substrates or in tandem configuration with silicon commercial modules for applications in the rising field of Building Integrated Photovoltaic (BIPV) or Product Integrated Photovoltaic (PIPV).

LIST OF PUBLICATIONS AND SCIENTIFIC CONFERENCES

Scientific publications

- F. Pattini, *et al.*, *Sol. Energ. Mat. Sol. C.*, 2020, **218**, 110724.
- B. Sibanda, T. S. Mahule, D. Delmonte, A. Sala, E. Gilioli and V. V. Srinivasu, *Mater. Res. Express*, 2021, **8**, 066101.
- G. Spaggiari *et al.*, *J. Phys. D: Appl. Phys.*, 2021, **54**, 385502.
- A. Sala, Z. Hoossen, A. Bacchi and M. R. Caira, *Molecules*, 2021, **26**, 4427.
- K. Abouabassi, *et al.*, *Coatings*, 2022, **12**, 75.

Scientific conferences

- A. Sala, F. Pattini, S. Rampino, A. Bosio, M. Sidoli, M. Mazzer and E. Gilioli, "New architectures for CIGS bifacial solar cells based on metal grids embedded in transparent back contacts", poster session presented at MASTEC - Materials for Today's Energy Challenge in Università di Padova, 3-4 June 2019.
- A. Sala, "The importance of crystallographic orientations in thin-films photovoltaic devices", online poster session presented at GCI@home – September 2020.
- A. Sala, D. Delmonte, E. Gilioli, "Photovoltaic varnishes: chalcogenide based thin-film solar cells by ultra-low-cost ball milling", oral session presented at the XLIX Meeting of the Italian Association of Crystallography (AIC), 6-9 September 2021.

REFERENCES

[1] X. Zeng. Highlights of GML’s contributions to the 2020 BAMS State of the Climate Report, 2021. https://gml.noaa.gov/news/state_of_climate.html (accessed October 2021).

[2] Lindsey R., Climate Change: Atmospheric Carbon Dioxide, https://www.climate.gov/news-features/understanding-climate/climate-change-atmospheric-carbon-dioxide, (accessed March 2021).

[3] Allen, M.R. *et al.*, *2018: Framing and Context.* In: Global Warming of 1.5°C. An IPCC Special Report on the impacts of global warming of 1.5°C above pre-industrial levels and related global greenhouse gas emission pathways, in the context of strengthening the global response to the threat of climate change, sustainable development, and efforts to eradicate poverty [Masson-Delmotte, V., P. Zhai, H.-O. Pörtner, D. Roberts, J. Skea, P.R. Shukla, A. Pirani, W. Moufouma-Okia, C. Péan, R. Pidcock, S. Connors, J.B.R. Matthews, Y. Chen, X. Zhou, M.I. Gomis, E. Lonnoy, T. Maycock, M. Tignor, and T. Waterfield (eds.)]. In Press.

[4] The Paris Agreement, https://ec.europa.eu/clima/policies/international/negotiations/paris_en (accessed march 2021).

[5] H. Ritchie and M. Roser (2020) - "*Renewable Energy*". Published online at OurWorldInData.org. Retrieved from: 'https://ourworldindata.org/renewable-energy' [Online Resource].

[6] IEA (2020), Key World Energy Statistics 2020, IEA, Paris https://www.iea.org/reports/key-world-energy-statistics-2020.

[7] Global Solar Atlas. https://globalsolaratlas.info/global-pv-potential-study (access March 2021).

[8] K. Ponomarjova. Disenchantment: The Culture of Narcissism and Mainstream Economics, pp. 24. Research report, University of Strasbourg, Strasbourg, FR, 2015.

[9] C. Meehan. NREL Developing Improved Tech to Lower Costs for Multi-Junction Solar Cells, 2018. https://www.solarreviews.com/blog/nrel-developing-tech-lower-cost-multi-junction-solar-cells#:~:text=To%20give%20a%20cost%20comparison,a%20watt%20at%20this%20point (accessed March 2022).

[10] E. Becquerel, *Comptes rendus des séances de l'Académie des sciences*, 1839, **9**, 561-567.

[11] D. M. Chapin, C. S. Fuller and G. L. Pearson, *J. Appl. Phys.*, 1954, **25**, 676–677.

[12] S. Rühle, *Sol. Energy*, 2016, **130**, 139–147.

[13] Best Research-Cell Efficiency Chart. https://www.nrel.gov/pv/cell-efficiency.html (access March 2021).

[14] Price quotes updated weekly – PV Spot Prices". PV EnergyTrend. Retrieved 13 July 2020.

[15] J. F. Geisz, R. M. France, K. L. Schulte *et al.*, *Nat Energy*, 2020, **5**, 326–335.

[16] G. Yu, J. Gao, J. C. Hummelen, F. Wudl, and A. J. Heeger, *Science*, 1995, **270**, 1789.

[17] R. H. Friend *et al.*, *Nature*, 1995, **376**, 498.

[18] L. Meng *et al.*, *Science*, 2018, **361**, 1094-1098.

[19] J. Jiang *et al.*, *Appl. Phys. Lett.*, 2020, **117**, 203901.

[20] M. Pagliaro, R. Ciriminna, and G. Palmisano, *ChemSusChem*, 2008, **1**, 880-891.

[21] Q. Tai and F. Yan, *Adv. Mater.*, 2017, **29**, 1700192.

[22] R. Guerrero-Lemus, R. Vega, T. Kim, A Kimm, and L. E. Shephard, *Renew. Sust. Energ. Rev.*, 2016, **60**, 1533-1549.

[23] M. Yamaguchi *et al.*, *J. Phys. D: Appl. Phys.*, 2018, **51**, 133002.

[24] M. R. Cibi and S. Manikandan, *IOP Conf. Ser.: Mater. Sci. Eng.*, 2021, **1130**, 012033.

[25] R. Scheer and H.-W. Schock, 2011. Chalcogenide Photovoltaics: Physics, Technologies, and thin-film Devices. WILEY-VCH, Chapter 3.

[26] A. B. Phillips, K. K. Subedi, G. K. Liyanage, F. K. Alfadhili, R. J. Ellingson, and M. J. Heben, *ACS Appl. Energy Mater.*, 2020, **3**, 6072−6078.

[27] M. Mazzer *et al.*, *Sol. Energ. Mat. Sol. C.*, 2017, **166**, 247–253.

[28] M. B. Johnston and L. M. Herz, *Acc. Chem. Res.*, 2016, **49**, 146−154.

[29] Z. Li *et al.*, *Nat. Commun.*, 2019, **10**, 125.

[30] J. P. Sawant, S. F. Shaikh, R. B. Kale, and H. M. Pathan, *Engineered Science*, 2020, **12**, 1-12.

[31] D. Delmonte *et al.*, *Semicond. Sci. Technol.*, 2020, **35**, 045026.

[32] F. Pattini, M. Bronzoni, F. Mezzadri, F. Bissoli, E. Gilioli, and S. Rampino, *J. Phys. D: Appl. Phys.*, 2013, **46**, 245101.

[33] M. Nistor, N. B. Mandache, and J. Perriere, *J. Phys. D: Appl. Phys.*, 2008, **41**, 165205.

[34] A. Liguori, C. Gualandi, M. L. Focarete, F. Biscarini, and M. Bianchi, *Coatings*, 2020, **10**, 16.

[35] R. J. Choudhary *et al.*, *Appl. Phys. Lett.*, 2004, **84**, 1483.

[36] T. Ono, T. Kenmotsu, and T. Muramoto. *Simulation of the Sputtering Process*. In Reactive Sputter Deposition., D. Depla, S. Mahieu (eds), Springer Series in Materials Science, 109; Springer, Berlin, Heidelberg, 2008.

[37] I. Safi, *Surf. Coat. Tech., 2000*, **127**, 203-219.

[38] J.T. Gudmundsson *et al.*, *J. Vac. Sci. Technol. A*, 2012, **30**, 030801.

[39] M. Samuelsson, D. Lundin, J. Jensen, M. A. Raadu, J. T. Gudmundsson, and U. Helmersson, *Surf. Coat. Tech.*, 2010, **205**, 591–596.

[40] A. Anders, *J. Appl. Phys.*, 2017, **121**, 171101.

[41] G. Regmi, A. Ashok, and S. Velumani. *In Large Area (10 x10 cm^2) Production of CdS Buffer Layer for Solar Cells by Chemical Bath Method*. Proceedings of the 17th International Conference on Electrical Engineering, Computing Science and Automatic Control (CCE), Mexico City, Mexico, November 11-13, 2020; IEEE 2020.

[42] M. R. De Guire, L. P. Bauermann, H. Parikh, and J. Bill. *Chemical Bath Deposition*. In Chemical Solution Deposition of Functional Oxide thin-films, T. Schneller, R. Waser (eds); Springer, Vienna, 2013; Ch. 14, pp 319-339.

[43] S.M. Pawar, B.S. Pawar, J.H. Kim, Oh-Shim Joo, and C.D. Lokhande, *Curr. Appl. Phys.*, 2011, **11**, 117-161, Fig. 2.

[44] V. Murza, O. Friedman, L. Vradman, and Y. Golan, *Cryst. Eng. Comm.*, 2018, **20**, 3765.

[45] A. J. Lynch and C. A. Rowland; *The History of Grinding*; SME, 2005.

[46] P. A. Thiessen, *Z. Chem.*, 1965, **5**, 162.

[47] I. Tole, K. Habermehl-Cwirzen, and A. Cwirzen, *Miner. Petrol.*, 2019, **113**, 449–462.

[48] B. Wu and A. Kumar, *Appl. Phys. Rev.*, 2014, **1**, 011104.

[49] Y. Chen, *Microelectron. Eng.*, 2015, **135**, 57-72.

[50] R. Garcia, A. Knoll, and E. Riedo, *Nat. Nanotechnol.*, 2014, **9**, 577–587.

[51] MATCH! Phase Analysis using Powder Diffraction. https://www.crystalimpact.com/match/ (accessed Dec. 22, 2021).

[52] U. Holzwarth and N. Gibson, *Nat. Nanotechnol.*, 2011, **6**, 534.

[53] PVEducation. https://www.pveducation.org/ (accessed June 18, 2021).

[54] Z. Li *et al.*, *Nat. Commun.*, 2019, **10**, 125.

[55] A. Mavlonov *et al.*, *Sol. Energy*, 2020, **201**, 227-246.

[56] J. Black, E. M. Conwell, L. Seigle, and C. W. Spencer, *J. Phys. Chem. Solid*, 1957, **2**, 240–251.

[57] X. Liu *et al.*, *Prog. Photovoltaics Res. Appl.*, 2017, **25**, 861-870.

[58] F. Pattini, *et al.*, *Sol. Energ. Mat. Sol. C.*, 2020, **218**, 110724.

[59] X. Hu *et al.*, *Appl. Mater. Today*, 2019, **16**, 367–374.

[60] G. Spaggiari *et al.*, *J. Phys. D: Appl. Phys.*, 2021, **54**, 385502.

[61] J. P. Sawant, S. F. Shaikh, R. B. Kale, and H. M. Pathan, *Eng. Sci.*, 2020, **12**, 1–12.

[62] W. C. Huang *et al.*, *Langmuir*, 2012, **28**, 8496−8501.

[63] M. I. Schimmel, N. R. de Tacconi, and K. J. Rajeshwar, *J. Electroanal. Chem.*, 1998, **453**, 187−195.

[64] Y. Tani *et al.*, *Res. Chem. Intermed.*, 2021, **47**, 169–182.

[65] D. Delmonte *et al.*, *Inorg. Chem.*, 2020, **59** (16), 11670-11675.

[66] D. Delmonte *et al.*, *Semicond. Sci. Technol*, 2020, **35**, 045026.

[67] B. J. Stanbery, *Crit. Rev. Solid State Mater. Sci.*, 2002, **27**, 73−117.

[68] S. R. Kodigala. *Cu(In,Ga)Se_2 Based thin-film Solar Cells*; Academic, Burlington (MA), 2010.

[69] M. J. Shin *et al.*, *Sol. Energy*, 2019, **181**, 276–284.

[70] M. Ganchev *et al.*, *Thin Solid Films*, 2006, **325**, 511–512.

[71] I. Bouchama *et al.*, *J. Mol. Struct.*, 2020, **1217**, 128457.

[72] S. Rampino *et al.*, *Appl. Phys. Lett.*, 2012, **101**, 132107.

[73] F. Pattini *et al.*, *J. Phys. D: Appl. Phys.*, 2013, **46**, 245101.

[74] S. Rampino *et al.*, *Sol. Energ. Mat. Sol. C.*, 2015, **133**, 82–86.

[75] D. Colombara *et al.*, *Nat. Commun.*, 2018, **9**, 826.

[76] D. Colombara *et al.*, *J. Mater. Chem. A*, 2020, **8** (14), 6471-6479.

[77] A. Chirila *et al.*, *Nat. Mater.*, 2013, **12**, 1107-1111.

[78] S. T. Kim, H. J. Jeong, Y. C. Kim, V. Bhatt, M. Kumar, J. H. Yun, and J. H. Jang, *Energy Reports*, 2021, **7**, 2255–2261.

[79] V. D. Moreno-Regino *et al.*, *Results Phys.*, 2019, **13**, 102238.

[80] P. K. Weimer, *Proceedings of the IRE*, 1962, **50** (6), 1462-1469.

[81] R. W. Smith, *Phys. Rev.*, 1957, **105** (3), 900.

[82] Yu A Akimov *et al.*, *Sov. J. Quant. Electr.*, 1972, **2** (3), 284.

[83] M. Ouafia, B. Jaberb, and L. Laânaba, *Superlattices and Microst.*, 2019, **129**, 212–219.

[84] Kim Hyon Chol *et al.*, *Opt. Mater.*, 2021, **112**, 110790.

[85] Hiroshi Mori. *Radiation energy transducing device*. US 3278811, October 3, 1961.

[86] N. M. Bordina, T. M. Golovner, V. V. Zadde, K. N. Zaitseva, A. P. Landsman, and V. I. Streltsova, *Applied Solar Energy*, 1975, **11** (5–6), 81–86.

[87] A.Cuevas, A.Luque, J.Eguren, and J.del Alamo, *Sol. Energy*, 1982, **29** (5), 419-420.

[88] H. Ohtsuka, M. Sakamoto, K. Tsutsui, and Y. Yazawa, *Prog. Photovolt.: Res. Appl.*, 2000, **8**, 385-390.

[89] N. Lusson. *Bifacial modules: The challenges and advantages*. https://www.pv-magazine.com/2020/08/19/bifacial-modules-the-challenges-and-advantages/#:~:text=Results%20and%20studies%20have%20shown,high%20as%2030%2D40%25 (accessed October 19, 2021).

[90] J. Page. *The Role of Solar Radiation Climatology in the Design of Photovoltaic Systems*. In Practical Handbook of Photovoltaics: Fundamentals and Applications, T. Markvart and L. CastaŁżer; Elsevier, 2003; pp. 60-61.

[91] J. Benemann, O. Chehab, and E. Schaar-Gabriel, *Sol. Energ. Mat. Sol. C.*, 2001, **67**, 345-354.

[92] T. S. Liang *et al.*, *Energy Environ. Sci.*, 2019, **12**, 116.

[93] F. Fu *et al.*, *Nat. Commun.*, 2015, **6**, 8932.

[94] M. Espindola-Rodriguez *et al. Efficient bifacial* $Cu_2ZnSnSe_4$ *solar cells*. In: Proceedings of IEEE, 2015, pp. 1–3.

[95] J. Wu *et al.*, *Sci. Rep.*, 2014, **4**, 4028.

[96] R. Guerrero-Lemus, R. Vega, T. Kim, A. Kimm, and L.E.Shephard, *Renew. Sust. Energ. Rev.*, 2016, **60**, 1533–1549.

[97] W. Gu, T. Ma, S. Ahmed, Y. Zhang, and J. Peng, *Energ. Convers. Manage.*, 2020, **223**, 113283.

[98] A. Hübner, A.G. Aberle, and R. Hezel, *Appl. Phys. Lett.*, 1997, **70**, 1008-1010.

[99] L. Kreinin, N. Bordin, A. Karsenty, A. Drori, and N. Eisenberg. *Experimental analysis of the increases in energy generation of bifacial over mono-facial PV modules*. In: Proceedings of the 26th European photovoltaic solar energy conference, Hamburg, Germany; 2011, 3140–3.

[100] A. Edler, M. Schlemmer, J. Ranzmeyer, and R. Harney. *Flasher setup for bifacial measurements*. In: bifiPV Workshop, Konstanz; 2012.

[101] J.P. Singh, T.M. Walsh, and A.G. Aberle, *Prog. Photovoltaics Res. Appl.*, 2014, **22**, 903-909.

[102] T. Nakada, *Thin Solid Films*, 2005, **480–481**, 419–425.

[103] N. Cavallari *et al.*, *Appl. Surf. Sci.*, 2017, **412,** 52–57.

[104] M. Mazzer *et al.*, *Sol. Energ. Mat. Sol. C.*, 2017, **166**, 247–253.

[105] T. W. Harris; Chemical Milling: the Technology of Cutting Materials by Etching; 1st Ed., Clarendon Press, 1976.

[106] S. L. Triana *et al.*, *J. Phys.: Conf. Ser.*, 2016, **776**, 012005.

[107] L. Guo *et al.*, *Sol. RRL*, 2018, **2**, 1800128.

[108] Z. Li *et al.*, *Adv. Mater.*, 2019, **31**, 1903914.

[109] F. A. El-Salam and E. A. El-Wahabb, *Vacuum*, 1992, **43**, 849-853.

[110] Y.H. Kwon *et al.*, *Sol. Energ. Mat. Sol. C.*, 2017, **172**, 11–17.

[111] Y. Zhou, L. Wang, S. Chen *et al.*, *Nat. Photonics*, 2015, **9**, 409–415.

[112] R. Tang, X. Chen, G. Liang, Z. Su, J. Luo, and P. Fan, *Surf. Coat. Tech.*, 2019, **360**, 68-72.

[113] K. J. Tiwari *et al.*, *Solar Energ. Mat. Sol. C.*, 2020, **215**, 110603.

[114] Y. Zhou *et al.*, *Nat. Commun.*, 2019, **10**, 125.

[115] J. Zhou *et al.*, *J. Alloy Compd.*, 2021, **862**, 158703.

[116] J. Mendes and J. Embden. *Vapour transport deposition of highly [002] oriented Sb_2Se_3 thin-films on nanostructured substrate for solar cells, Symposium L: Nanomaterials for Energy Applications*. In: International Conference on Nanostructured Materials (NANO 2020). Melbourne: Engineers Australia, 2020, 262.

[117] D. Delmonte *et al.*, *Semicond. Sci. Technol.*, 2020, **35**, 045026.

[118] W. Lua, Y. Fub, and B. Tseng, *J. Phys. Chem. Solids*, 2008, **69**, 637–640.

[119] W. Wang, Z. Fu, and H. Wang, R. Yuan, *J. Am. Ceram. Soc.*,2002, **22**, 1045–1049.

[120] C. Jiang, R. Tang, X. Wang, H. Ju, G. Chen, and T. Chen, *Sol. RRL*, 2019, **3**, 1800272.

[121] D. Shin *et al.*, *Sol. Energ. Mat. Sol. C.*, 2016, **157**, 695-702.

[122] G. Altamura, M. Wang, and K. L. Choy, *Sci. Rep.*, 2016, **6**, 22109.

[123] D. Fraga, T. Stoyanova Lyubenova, R. Martí, I. Calvet, E. Barrachina, and J. B. Carda, *Sol. Energy*, 2017, **147**, 1-7.

[124] D. Colombara, *Phys. Rev. Materials*, 2019, **3**, 054602.

[125] D. Colombara, K. Conley, M. Malitckaya, H.-P. Komsa, and M. J. Puska, *J. Mater. Chem. A*, 2020, **8**, 6471-6479.

[126] R. French, A. Jacobson, B. Kim, S. Isley, R. Leepenn, and P. Baveye, *Environ. Sci. Technol.*, 2009, **43**, 1354–1359.

[127] P. M. P. Saloméa, H. Rodriguez-Alvareza, and S. Sadewassera, *Sol. Energ. Mat. Sol. C.*, 2015, **143**, 9-20.

[128] V. I. Kalikmanov; Classical Nucleation Theory. In: *Nucleation Theory. Lecture Notes in Physics*, Vol: 860; Springer, Dordrecht, 2013.

[129] K. Siemer, J. Klaer, I. Luck, J. Bruns, R. Klenk, and D. Braunig, *Sol. Energ. Mat. Sol. C.*, 2001, **67**, 159-166.

[130] H. Rau, T. R. N. Kutty, and J. R. F. Guedes De Carvalho, *J. Chem. Thermodyn.*, 1973, **5**, 833-844.

[131] J. Bekaert, R. Saniz, B. Partoens, and D. Lamoen, *J. Appl. Phys.*, 2015, **117**, 015104.

AKNOWLEDGEMENTS

At this point I think it is possible to stop using English and write a bit in Italian.

Siamo finalmente arrivati in fondo a questo lungo percorso, bello e travagliato allo stesso tempo. Vorrei ringraziare tutte le persone che hanno contribuito a questo lavoro, sia direttamente che indirettamente, ma, per evitare di scrivere una nuova tesi, dovrò limitarmi alle più importanti!

Vorrei pertanto ringraziare:

Davide Delmonte per avermi fatto appassionare al mio lavoro, per avermi fatto credere in me stesso, oltre che guidato, supportato… e *sopportato*. Credo fermamente che persone così belle, altruiste, curiose, energiche e preparate allo stesso tempo siano cosa rarissima da trovare. Io ho avuto la fortuna di imparare da una di queste, un vero mentore. Grazie per aver reso indimenticabile ogni momento passato insieme, in laboratorio o altrove, per avermi insegnato cosa significa fare ricerca e per essere il capetto che sei. Davvero, ***grazie***!

Edi Gilioli per la sua guida e per la sua profonda esperienza nel campo della ricerca.

Elena e Chiara. Grazie a voi il gruppo si ravvivato ed è diventato più unito che mai. Ogni momento passato assieme è stato bellissimo: le risate, i caffè, i petteguless ma anche le nottate al lavoro e l’aiuto reciproco per soddisfare gli altissimi standard del capetto. Avete saputo rendere indimenticabile anche un viaggio difficile come quello in Sudafrica. Anche se il nostro carattere ci ha fatti scontrare a volte, una buona partita a Tokyo, una tazza di roiboos e il bobootie ci hanno sempre riavvicinati. Princess Elena, un giorno prenderai la scantarina e mi dirai che odore ha l’azoto; Chiaretta fai vedere a chi fa cose per pochi come si lavora in officina! In voi ho trovato delle buonissime amiche e delle valide alleate nel lavoro e nella vita, grazie ragazze!

Il gruppo di Camlin Italy. Kostantin Koshmak, Davide Vurro, Pasquale D’Angelo, Giuseppe Tarabella e Luca Ascari, grazie per l’ottimo lavoro svolto assieme, per le idee e gli sforzi per portare le nostre ricerche a livelli competitivi.

Marco Villani e Silvia Zanettini. Grazie Villo per il mutuo soccorso nelle carenze del laboratorio, per il reciproco supporto per la realizzazione di tutti gli esperimenti e per i bei momenti passati in pausa caffè. Grazie Silvia per l'ottima intesa e il tuo sempre presente aiuto nelle attività di litografia.

Tutti i ricercatori e i collaboratori IMEM. Grazie infinite Francesco Mezzadri per le misure XRD ad alta risoluzione e per il tuo supporto quando le mie conoscenze di cristallografia venivano a mancare. Giovanna Trevisi, ti ringrazio per le misure SEM-EDX e per il lavoro svolto insieme, anche in orari o giorni impossibili. Patrizia Ferro, grazie per le misure PXRD, per la tua pazienza e per avermi permesso di imparare ad utilizzare il tuo diffrattometro. Marco Pola, grazie per l'instancabile lavoro in Istituto e per le belle chiacchierate a fine giornata. Enos Gombia, ti ringrazio moltissimo per aver condiviso un poco della tua profonda conoscenza sui semiconduttori, sulla fotolitografia e sull'evaporazione dei metalli. In più un ringraziamento sentito anche a Massimo Mazzer, Francesco Bissoli, Mara Carra, Giovanni Maione, Andrea Zappettini, Antonella Secondulfo, Antonio De Sanctis, Matteo Bosi, Giovanni Attolini, César De Julian Fernandez e Roberto Mosca.

Alessia Bacchi. Grazie per essermi stata accanto dal punto di vista personale e scientifico durante questi anni, per avermi sempre coinvolto in progetti di divulgazione e per avermi dato preziosissimi consigli e aiuti per sviluppare la mia vita professionale.

Tutti i miei compagni di (dis)avventure in IMEM. Ale, Rick, Edo, Manu, Nico, Vitti, Filo, Gabri e Vale. Ricordare tutto quello che ho passato insieme a voi non starebbe in un libro! Pranzi e pause del genere, con o senza cronometro, non si dimenticano facilmente… Grazie per il supporto e per bellissimo tempo speso assieme, speriamo di rivederci prima che Edo finisca di mangiare la sua pizza!

Bronz, Enzo e tutto il gruppo dell'Aperitivo Scientifico. Prima come interni IMEM, poi come amici al di fuori siete riusciti a supportarmi e a consigliarmi al meglio per non cedere alla follia e per riuscire a concludere ottimamente questo percorso. Spero che Malik ci accompagni ancora nelle nostre serate in trasferta e che si possa prenotare dell'ottimo cavallo pesto come quello del Navetta.

A tutti i miei amici per i momenti di svago e felicità passati assieme. Davide, Francesco, Nima, Giulia e Carlotta che, nonostante la distanza o i problemi lavorativi siete stati sempre presenti durante questi anni, soprattutto nei momenti di più grande difficoltà con i vostri incoraggiamenti. Grazie a Cristina che, nella mia stessa situazione, ha saputo supportarmi veramente al meglio. Grazie anche a Valentina, Francesca, Giovanni, Federico, Giulio, Alice e Luca!

Matteo, i miei genitori, Roberta e Carlo, i miei nonni, Anna e Dino. Ultimi ma non meno importanti, hanno rappresentato sostegno più grande, un vero e proprio pilastro. Sono veramente grato per la loro capacità di farmi vedere le cose da un'altra prospettiva, per tutti gli incoraggiamenti, l'enorme supporto e una dose *titanica* di pazienza ogni volta che è stato necessario per tutti gli aspetti di questo lungo e articolato percorso.